Dipl.-Ing. Patrick Posch, BSc

Ion Dynamics in Oxide-Type Solid Electrolytes and Electrode Materials

DISSERTATION

zur Erlangung des akademischen Grades

Doctor Technicae

eingereicht an der

Technischen Universität Graz

Betreuer

Univ.-Prof. Dr. rer. nat. Martin Wilkening

Institut für Chemische Technologie von Materialien

Graz, Juli 2019

Eidesstattliche Erklärung

Ich erkläre an Eides statt, dass ich die vorliegende Arbeit selbstständig verfasst, andere als die angegebenen Quellen/Hilfsmittel nicht benutzt, und die den benutzten Quellen wörtlich und inhaltlich entnommenen Stellen als solche kenntlich gemacht habe. Das in TUGRAZonline hochgeladene Textdokument ist mit der vorliegenden Dissertation identisch.

Datum

Unterschrift

Danksagung

Ich möchte mich vielmals bei allen Personen bedanken, die maßgeblich zur Entstehung dieser Arbeit beigetragen haben. Aus diesem Grund werde ich die mannigfaltigen Arten der Beiträge in den folgenden Absätzen etwas genauer erläutern.

An erster Stelle sollte hier Prof. Martin Wilkening genannt werden, der mich in seine Arbeitsgruppe aufgenommen und damit den Grundstein für dieses Werk gelegt hat. Darüber hinaus habe ich von ihm gelernt, wie wichtig es ist, bei solch einem schwierigen Unterfangen das Ziel nicht aus den Augen zu verlieren. Seine Intuition zur richtigen Zeit die richtigen Akzente zu setzen, und damit eine eingängige, praktisch orientierte Wissensvermittlung zu schaffen, habe ich stets sehr geschätzt. Selbst in noch so hektischen und stressigen Zeiten kümmerte er sich mit stoischer Ruhe um die Anliegen seiner Mitarbeiter und stand einem stets mit Rat und Tat zur Seite.

Ein weiterer großer Dank gilt auch den Post-docs der Arbeitsgruppe, Dr. Ilie Hanzu und Dr. Daniel Rettenwander, die sich stets Zeit genommen haben

um anfallende Probleme zu diskutieren. Auch mit Fragen zu Proben oder deren Charakterisierung konnte man sie zu jeder nur erdenklichen Zeit aufsuchen; dafür bin ich sehr dankbar.

Einen besonderen Dank möchte ich auch meinen Bürokollegen, Sarah Lunghammer und Martin Philipp, aussprechen. Ihr habt über die ganze Zeit hinweg für ein angenehmes Arbeitsklima gesorgt und triste Momente mit viel Witz und Ironie erhellt. Ich danke euch für die vielen schönen Erlebnisse innerhalb und außerhalb der Arbeitszeit.

Christina Albering gebührt nicht nur Dank für das Auftreiben von Chemikalien und Gerätschaften aller Art, sondern auch für den freundschaftlichen Umgang den wir stets pflegten. Ihre Hilfsbereitschaft und ihre selbstlose Art haben mich immer wieder überrascht und begeistert.

Angela Hampl, Margareta Maierhofer und Rosina Kerschbaumer will ich für das stets einladende und ordentliche Arbeitsumfeld sowie die gelegentlichen, sehr willkommenen, Gespräche fernab der Wissenschaft danken.

Allen ehemaligen und aktuellen Mitgliedern der Arbeitsgruppe danke ich für die Zusammenarbeit.

Unendlich großer Dank gebührt meiner meiner Familie, Sarahs Familie und meinen Freunden. Ihr alle wart in schwierigen Zeiten mein Fels in der

Brandung. Ihr hattet stets ein offenes Ohr für meine Probleme und hattet jederzeit gute Ratschläge parat. Dafür danke ich euch von ganzem Herzen!

Mit großer Freude nenne ich die wichtigste Person zum Schluss. Liebe Sarah, ich danke dir für die unendlich vielen schönen Momente die ich in den letzten Jahren mit dir verbringen durfte. Du hast mich jederzeit in meinem Handeln unterstützt und mich mit keinem Problem je alleine gelassen. Ich könnte mir keine bessere Begleiterin vorstellen.

KURZFASSUNG

Auf der ganzen Welt spielen wiederaufladbare Li-Ionenbatterien seit den frühen 90er-Jahren eine wichtige Rolle in unserem täglichen Leben. Unabhängig von Alter, sozialer Stellung, Einkommen oder Wohnort kommen Menschen mit elektronisch betriebenen Geräten, Autos oder gar Flugzeugen in Kontakt. Betrachtet man die Sicherheit solcher Batteriesysteme, dann stellen thermische Belastungen für die derzeit verfügbaren Produkte ein großes Problem dar und arten in Bränden oder gar Explosionen aus. Ursache für diese Zwischenfälle sind die standardmäßig verwendeten organischen Flüssigelektrolyte. Die in den letzten Jahrzehnten vorgestellten Festelektrolyte, bestehend aus Keramiken oder Polymeren, stellen eine adequate Lösung dieser Probleme dar. Auf der Suche nach Zelltypen mit hoher Energiedichte und gleichermaßen hoher thermischen Belastbarkeit, wurde die Wissenschaft immer häufiger auf potenzielle Festelektrolyte aufmerksam. Um auf Zellebene hohe Energiedichten zu erreichen, bedarf es ähnlich schneller Ionendynamik in festen Elektrolytmaterialien wie sie derzeit in flüssigen Medien vorzufinden sind.

Die zweite wichtige Anforderung, nämlich thermische Belastbarkeit, hängt jedoch weitgehend von den chemischen Ursprüngen der Materialien ab.

Oftmals wird die hohe ionische Leitfähigkeit der Elektrolyte als Hauptanforderung zur Realisierung von Festelektrolytbatterien genannt. Ebendiese Leitfähigkeit wird von einer Vielzahl von Eigenschaften wie Defekten, Kristallinität und Kristallstruktur oder der chemischen Zusammensetzung beeinflusst. Um diese Eigenschaften leichter beeinflussen zu können stehen adaptierbare Syntheserouten hoch im Kurs. Allerdings bedarf es zur Verbesserung derzeitig bekannter Materialien einer aufwendigen Untersuchung der Ionendynamik samt zugrunde liegender Diffusionspfaden.

Zeitgleich arbeitet die Wissenschaft mit Hochdruck an der Verbesserung von Batterien auf Zellebene. Da das Zellpotential, welches die Anwendungsbereiche der Batterie maßgeblich beinflusst, hauptsächlich von den verwendeten Elektrodenmaterialien abhängt, ist genaues Verständis des Interkalationsprozesses bei neuen Materialien von enormer Bedeutung.

Diese Arbeit beschäfigt sich hauptsächlich mit Ionendynamik in oxidischen Festelektrolyten und Elektrodenmaterialien. Hierbei wurde, vom Festelektrolyten im inneren der Zelle ausgehend, jeder Bestandteil einer Zelle, bis hin zu den Stromableitern, analysiert. Zuerst wurde mit einer Kombination aus

Impedanzspektroskopie und Kernspinresonanz (NMR) die Ionendynamik von $Li_7La_3Zr_2O_{12}$ (LLZO) Festelektrolyten, im makroskopischen wie mikroskopischen Maßstab, aufgeklärt. Hierbei wurden erstmalig Al- und Ga-substituierte LLZO Einkristalle auf ihre Ionendynamik hin untersucht. Diese Einkristalle eignen sich durch ihre chemische Homogenität und das völlige Fehlen von Korngrenzen besonders gut zur Analyse von elementaren Sprungprozessen. In beiden Fällen konnte eine weitaus bessere Auflösung der Sprungprozesse erreicht werden als in polykristallinen Proben Proben mit ähnlicher Zusammensetzung.

Weiters wurde eine umfangreiche NMR-Studie zur Phasenbildung in chemisch sodiiertem $Li_4Ti_5O_{12}$ (LTO) durchgeführt. Im Gegensatz zur Interkalation von Li, findet sich in der Literatur zur Interkalation von Na in LTO ein weitaus komplexerer Phasenbildungsprozess wieder. Ergebnisse zeigen die Bildung einer *solid solution*, welche beide Ladungsträger beherbergt und einen Übergang zwischen lithiumreichen und natriumreichen Regionen des Materials bildet. Die Dynamik des jeweiligen Ladungsträgers hängt hierbei stark von der Quantität des eingebrachten Natriums ab. Diese Abhängigkeit wurde anhand von mehreren Proben mit unterschiedlichen Sodiierungsgraden mittels ^{7}Li und ^{23}Na NMR Messungen ermittelt.

In einer weiteren Studie wurden die Aluminium Stromableiter in Na-Ionenbatterien auf etwaige Schäden durch Reaktionen mit anderen Zellkomponenten untersucht. Hierbei wurde der Einfluss auf die Leistung der Systeme mittels elektrochemischer Analysemethoden und der Zustand der verwendeten Elektroden mittels Rasterelektronenmikroskopie festgestellt.

Nach einer kurzen Einführung in die Grundlagen zu Batterien und Festkörperdiffusion werden die Ergebnisse kumulativ in Form von Publikationen in Fachzeitschriften und Manuskripten vorgestellt.

Abstract

Since the early 1990s, rechargeable Li-ion batteries play an essential role in the everyday life of people all around the globe. Regardless of age, social position, income or place of residence, people come in contact with portable electronic devices, electric vehicles or even electric aircrafts on a daily basis. In terms of safety, however, commercial products pose a high risk of thermal runaway that results in catching fire or even explosions. To overcome those issues, mainly related to the organic liquid electrolyte, alternatives like polymer or solid electrolytes were introduced during the last decades. In search for high energy densities at similarly high thermal stability, various solid electrolytes materials entered the spotlight of research throughout the years. To achieve the former, fast ion dynamics close to those of liquid-based systems are needed, whereas the latter feature largely depends on the chemical origins of the solid electrolyte.

High ionic conductivity in solid electrolytes is often regarded as the key feature to realize all-solid-state batteries. The overall conductivity, however,

is heavily influenced by properties like defects, crystallinity, crystal structure, and chemical composition. Therefore, versatile synthesis routes to yield tailor-made products are highly sought after. Optimization of available materials requires sophisticated ion dynamics studies to accurately determine the underlying diffusion pathways.

Simultaneously, research brings to light new electrode materials to enhance battery performance on a cell level. The interaction between the two electrode materials determines the operating potential of a battery and has, therefore, a significant impact on application of a particular cell type. To make the most of newly developed electrode materials, it is essential to fully elucidate their storage processes.

This thesis is devoted to ion dynamics in oxide solid electrolyte materials and electrode materials. Here, battery cell components are regarded one step at a time, starting from a solid electrolyte through to the current collector materials. At first, impedance spectroscopy and ^{7}Li nuclear magnetic resonance (NMR) were employed to provide an in-depth look into ion dynamics of the garnet-type $Li_7La_3Zr_2O_{12}$ (LLZO) solid electrolyte. In this process, a combination of both analysis methods is a prerequisite to fully disclose ionic motion on a macroscopic level and, in addition, provide information on microscopic

hopping processes. Here, ion dynamics in novel single crystalline Al-stabilized and Ga-stabilized cubic LLZO garnets were probed for the first time. Due to their high homogeneity and absence of grain boundary contributions to the overall diffusion, these single crystalline samples are considered perfect model systems to probe elementary jump processes. Compared to polycrystalline analogs, both single crystals provided much better resolution of the fundamental hopping processes in LLZO-type garnets and, therefore, enable deeper understanding of the fast ionic motions in such systems.

Furthermore, a comprehensive NMR study sheds light on the phase formation processes in $Li_4Ti_5O_{12}$ (LTO) upon chemical sodiation. In stark contrast to lithiation of LTO, a more complex phase formation process is initiated by incorporation of Na-ions. Results suggest the formation of a solid solution that contains both charge carriers and acts as a connection between Li-rich and Na-rich regions. ^{7}Li and ^{23}Na NMR relaxation measurements performed on several samples with differing sodiation ratios revealed that the Li mobility, however, largely depends on the sodium content.

Moreover, the impact of Na-ion cell components on the surface of aluminum current collectors was studied. Here, special attention was directed to the influence on cell performance and *post-mortem* analysis of the electrodes.

Information on the former was gathered by electrochemical analysis methods, whereas the effects on current collector and electrode material were thoroughly studied by scanning electron microscopy.

In this thesis, a brief introduction to historical and theoretical background is followed by the obtained results, which are presented in a cumulative approach including published articles in peer-reviewed journals and manuscripts.

TABLE OF CONTENTS

1 Introduction **1**

2 Historical Evolution and State of the Art Systems **5**

2.1 Electrolytes 14

2.2 Solid Electrolytes 23

3 Fundamentals of Diffusion **40**

3.1 Diffusion in Solids 40

3.2 Diffusion at the Atomic Scale – Random Walk Theory 45

3.3 Diffusion Mechanisms 53

3.4 Origins of defects 56

3.5 Experimental Probes for Ion Dynamics 59

4 Results **80**

4.1 Ion Dynamics in Aliovalently Substituted Garnet-Type $Li_7La_3Zr_2O_{12}$ Single Crystals 80

4.2 Phase Formation in Chemically Sodiated Spinel-Type $Li_4Ti_5O_{12}$ 111

4.3 Is Aluminum a Proper Anode Current Collector in Na-ion Batteries? 124

5 Conclusions and Outlook **136**

Bibliography **141**

Appendix **163**

5.1 Supporting Information Single Crystalline Al-stabilized LLZO . 166

CHAPTER 1

INTRODUCTION

The worldwide energy demand is steadily increasing and, even though the generation of electricity from fossil fuels stagnates and the share generated from renewable sources grows continuously, serious questions arise that need to be answered in the near future [1]. Generation of electricity from renewable resources, *i.e.*, wind, solar, water and tidal energy, relies on the energy input from the environment and is, therefore, highly time dependent. Energy storage systems satisfy the need to separate the moment of energy generation from the moment of energy consumption. Among these storage systems, rechargeable electrochemical energy storage devices achieve high energy densities and, therefore, drastically reduce the required space to store large amounts of energy.

Even though this group of devices comprises a large variety of battery systems, the most promising candidates to fulfill the aforementioned task are batteries based on Li-ions or Na-ions. Today, sodium-ion batteries are highly regarded as stationary grid storage systems that can accumulate high amounts of energy, whereas the Li-ion technology is mainly used to power portable electronic devices or electric vehicles. Such batteries rely on shuttling of Li ions from cathode to anode and *vice versa*. External charge balance enables charging and discharging of the cell, even though performance of such Li-ion batteries depends largely on the individual cell components. Here, research focusses mainly on electrode materials and electrolyte materials and compositions, respectively. While a couple of electrode materials are well established and commercially available, liquid electrolyte systems caused some serious issues in the recent past. Commercially available cells make use of liquid electrolytes that are based on organic solvents to enhance ionic transport, although they pose a serious threat in terms of flammability.

Novel systems that are under development for a few years solely consist of solid materials and, therefore, significantly reduce the risk of thermal runaway. Solid-state electrolytes consist of materials that can either be assigned to the class of polymers, ceramics or glasses. Requirements for solid materials match

those for liquid systems, namely, high ionic conductivity, stable interfaces with electrode materials, temperature resistant, high chemical stability and high electrochemical stability window. In the class of oxidic ceramic solid-electrolytes, that are considered inherently stable and temperature resistant, ionic conductivities determine the suitability as electrolyte material. In such ceramic electrolytes, ionic conductivities are governed by many properties like defects, chemical composition, crystal structure and crystallinity.

This thesis is subdivided into an introductory part and an experimental part. The former consists of a historical recapitulation and provides basic knowledge of diffusion and the utilized analysis methods. The experimental part aims at introducing several diffusion phenomena to the overall ion dynamics in electrolyte materials, accurate determination of the phase formation processes in electrode materials and reactivity of cell components with current collector materials.

To resolve ion hopping mechanisms in the fast ion conductors Al-substituted and Ga-substituted $Li_7La_3Zr_2O_{12}$ (LLZO), impedance spectroscopy and NMR were employed. The combination of these two methods enables analysis of both macroscopic and microscopic ion dynamics. Comparison of empirical data with results from simulations leads to suggestion of possible diffusion

pathways of the lithium ions through the LLZO lattice. NMR was employed to elucidate the phase formation mechanism in chemically sodiated $Li_4Ti_5O_{12}$. In the end, an electrochemical study revealed the impact of aluminum anode current collectors on the overall performance of sodium-ion batteries.

CHAPTER 2

HISTORICAL EVOLUTION AND STATE OF THE ART SYSTEMS

The first heartbeat of a commercial primary lithium battery took place in US-laboratories of Wilson Greatbatch Ltd in 1972. Researchers aimed at an increase in volumetric capacity to achieve a severe reduction in size compared to its predecessor, the Zn–HgO battery. After extensive research, the so-called Model 702E found its way into the bodies of clients all over the world [2]. Regarding its advantage in size, weight and extended lifetime of up to 7 years, this system superseded previous technologies. This type of Li-iodine battery, consisting of a metallic lithium metal anode and an iodine cathode embedded

in a poly-2-vinylpyridine matrix, still powers many pacemakers all over the world [3]. Meanwhile, Japanese researchers at Matsushita Electric Inc. found a combination of Li metal, carbon fluoride and organic electrolyte that is operable as primary battery [4]. This company, which was renamed to Panasonic later on, produced such batteries in coin-type housings to power watches, calculators and wall-mounted clocks.

Suddenly, the strive to implement the latest technologies in military equipment promoted exploration of more advanced battery systems. At this point, research focused mainly on high energy and high power energy storage devices for military applications. Between 1972 and 1990, 44 patents comprising lithium storage devices were filed by research departments associated to the US armed forces. Most patent specifications focus on cell components, in particular electrolyte mixtures [5] and electrode engineering [6], while others approach cell design and connections between cells using modules [7]. Niche sulfur-based liquid electrodes like $SOCl_2$ or SO_2Cl_2 were thoroughly investigated during this time period.

In 1978, extensive research yielded a new class of electrode materials, viz., intercalation compounds [8]. These materials are able to temporarily incorporate foreign atoms into their crystal structure and release them at a sub-

sequent moment. In order to operate these cells efficiently, such intercalation compounds need to maintain high reversibility. Additionally, good electronic conducting properties are requested to ensure electronic balance. The most prominent examples for this class of compounds are TiS_2, V_2O_{10}, $LiCoO_2$ and LiC_6. Intercalation properties of titanium disulfide were thoroughly investigated by Whittingham and his coworkers at Exxon in 1978. First attempts included chemical insertion of Li into the TiS_2 host using *n*-butyl lithium. In good agreement with Bichon *et al.*, intercalation of Li with contents ranging between $0 \leq x \leq 1$ was found for Li_xTiS_2 in absence of any phase transformations [9]. To avoid energy loss during cell reactions, the absence of phase transformation processes was considered beneficial. Extensive testing revealed the formation of dendrites on metallic lithium anodes. These dendrites are able to pierce through separator materials and short circuit the cell. Depending on cell housing, short circuits lead to either ignition or explosion of the cell. Since both events cause severe damage to the cell and its environment, alterations to the metallic anode were necessary. *In situ* formation of an alloy, consisting of aluminum and lithium, during cell assembly finally resulted in commercialization of $LiAl \left| LiClO_4 \text{ (THF:DME)} \right| TiS_2$ coin cells [10]. Even though this setup accomplished shuttling of Li ions in absence of pure lithium metal, the

initial 10 cycles of its battery life were accompanied by severe capacity loss. This effect is caused by excessive volume expansion of almost 200 % during formation of the Al-Li alloy. As a result, the active alloy layer develops cracks and, therefore, loses its contact with the current collector. To improve reliability of secondary lithium based batteries, research was in need of novel Li bearing anodes that exhibit high reversibility. LiC_6 was explored and the strive for new stable anode materials found a sudden end [11]. Graphite-based anodes exhibit a structure of stacked planes and are able to incorporate Li ions between them. Various preparation methods are carried out at room temperature and benefit from low-cost natural carbon resources. The invention of a rechargeable battery cell containing the lithiated carbon compound, *i.e.*, Graphite $\left|\right.LiPF_6$ (org. solvent) $\left|\right.LiCoO_2$, was patented by Sony Corp. in 1991 and thereafter successfully brought to market [12]. Figure 2.1 sketches a cell, similar to the one patented by Sony, that comprises two intercalation electrodes. In a first attempt, the anodes were usually temperature treated soft carbon derivatives obtained from coke that, in combination with propylene carbonate (PC) based electrolytes, were prone to capacity fading when charged above 4.1 V. Close investigation of the storage process revealed expansion of the interplanar spacing from 335 pm to 372 pm during lithium insertion. Researchers focused

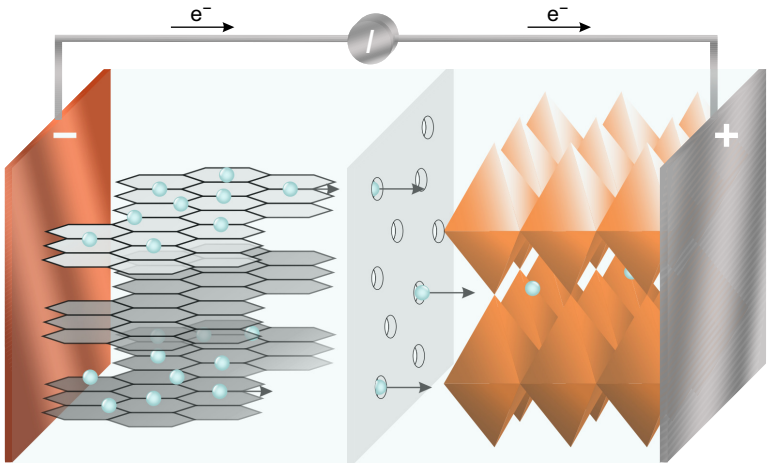

Figure 2.1: Schematic of a Li-ion cell that comprises 2 intercalation-type electrodes that are ionically connected to each other by an organic liquid electrolyte. Mobile Li ions are depicted as aqua colored marbles that move from one electrode to the other.

on other types of carbon, viz., hard carbon, to overcome this issue. Soft carbon is considered graphitizable and exhibits similar interplanar spacing as graphite, whereas the hard carbon counterpart is considered non-graphitizable and reveals plane gaps larger than 372 pm. Hence, synthesis of hard carbon was refined with much effort to yield a novel anode material for the second generation of Sony's Li-ion battery. Regarding energy density, an increase of almost 50 % was achieved by switching anode materials. Additionally, an increase in charging voltage to 4.2 V was achieved, and is nowadays considered a standard charging voltage for Li-ion batteries. Compared to discharge capacities of first generation cells hard carbon anodes can only compete when opting for low cutoff potentials around 2.5 V. Since electric devices, like cellular phones, often

require cutoff voltages higher than 3 V, further optimization of carbonaceous anodes was necessary. A combination of novel graphite preparation and completely redesigned ethylene carbonate (EC) based electrolyte finally met the desired requirements [13]. Carbon-based anodes, however, suffer from low gravimetric energy density, *i.e.*, 350 mA h g^{-1}, compared to metal alloy anodes or even pure lithium metal (3800 mA h g^{-1}).

In order to find suitable alternatives, alloys consisting of Al, Sn or Si were thoroughly investigated. Elements like tin and silicon enable reversible reactions with 4 or more Li ions. In the recent past, Si attracted loads of attention due to its high specific capacity of almost 3600 mA h g^{-1}. An attempt to compensate its volume expansion of 320 % during lithiation, which is considered the bottleneck for application of this material, was made by nanostructuring of the electrode [14]. Developing a nano-sized structure comprises formation of particles, rods, tubes or hollow spheres and an interconnection thereof. Recent publications report on SiOC electrodes, composed of silicon oxycarbide glass particles embedded in a carbon matrix, which maintain a capacity of 588 mA h g^{-1} throughout 1000 cycles [15]. Hence, the main challenge to establish alloy anodes is to overcome issues connected to massive volume expansion. Similar approaches were first realized by Sony Corp., viz., encapsulation of Sn-

Co nanoparticles in carbon matrix [16]. Due to its nanostructured texture, this system inhibits contact loss between electrode material and current collector by buffering volume changes. Furthermore, said material combination also maintains the capability of the carbon matrix to form a stable Solid Electrolyte Interphase (SEI) with Li and electrolyte components. Formation of a thin SEI film, on the one hand, protects the anode surface from unwanted reactions with the electrolyte and dendrite formation and, on the other hand, promotes Li diffusion towards the electrode [17]. Figure 2.2 illustrates the structure of an SEI layer. Compared to LiC_6, the SEI on alloy anodes is exposed to strain during cell operation. Mechanical load on the SEI can lead to cracks and, therefore, loss of its protective properties. As a result, SEI formation on such materials consumes up to 50 % of the initial capacity during the first cycles [18]. To optimize stability and performance of available Li-ion systems, research focused on new intercalation cathode compounds. First alternatives, viz., $LiFePO_4$ and $LiMn_2O_4$, entered the spotlight in 1996 [19, 20]. The former comprises an olivine 2-dimensional structure that accommodates Li ions in a channel-like structure. Iron phosphate is considered inherently stable and batteries consisting of said cathodes and graphite anodes are often used to replace environmentally hazardous lead acid systems. Spinel-structured

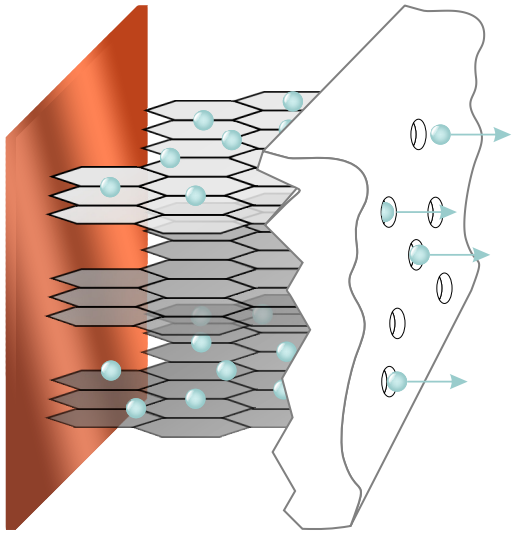

Figure 2.2: Illustration of an SEI layer close to the electrode surface. Aqua colored marbles represent Li ions that are able to trespass the SEI in both directions.

$LiMn_2O_4$ systems exhibit much smaller capacities, about two thirds compared to $LiCoO_2$, but offer enhanced safety and thermal stability. Its structure enables 3-dimensional ion transport through the crystal lattice. Modern approaches, *i.e.*, blends of multiple transition metals like $Li[Ni_xMn_yCo_z]O_2$ (NMC), favor tailor-made cathode compositions to meet specific requirements. Such NMC electrodes, usually described by the three letters x, y and z that indicate ratios between Ni, Mn, and Co, can serve as electrodes in power cells and energy cells, respectively. Even though the initial composition was set to NMC111, the increase in cobalt demand encouraged manufacturers to find Co-poor compositions that still offered high capacities in battery cells. Cost-efficient

tuning of electrochemical properties and its high versatility assured successful commercialization of this material class. Enhanced discharge capacities, an essential feature for high energy systems, are mainly achieved by increasing Ni contents and result in high demand for NMC811 that exhibits capacities up to 200 mA h g^{-1}. Nowadays, NMC is one of the most popular cathode materials in Li-based battery systems [21]. Alterations to this system comprise the exchange of Mn with Al. The obtained $Li[Ni_xCo_yAl_z]O_2$ (NCA) electrodes exhibit high discharge capacities, good reversibility and long storage calendar life. Their drawbacks are limited to rapid capacity loss at elevated temperatures [22]. In contrast to NMC, alterations to this material class only result in slight performance increases, whereas temperature dependent disadvantages can only be compensated on a cell level. Nonetheless, since electric vehicle manufacturer Tesla Inc. currently uses 18650 cells equipped with NCA cathodes and carbon anodes, this cathode material found its success in the market.

The latest change in commercially available electrode materials occurred in 2008, when the anode material $Li_4Ti_5O_{12}$ (LTO) surfaced. Known since the late 1980s, LTO exhibits outstanding cycle life and excellent low-temperature characteristics [23]. In stark contrast to other intercalation materials, its spinel-type structure enables reversible insertion of lithium ions at negligible volume

expansion [24–26]. All of the above mentioned benefits result in excellent withstanding of rapid charging rates, a feature that renders LTO a highly potent anode material for electric mobility. As a result of its low nominal cell potential of 2.4 V, when paired with NMC cathodes, this cell type is a very expensive option for large scale application [27].

2.1 Electrolytes

The electrolyte is considered a crucial, not yet discussed, component of the Li-ion battery. The absence of active hydrogen atoms is obligatory for its operation in lithium batteries. Decomposition of aqueous electrolytes would lead to failure of the cell, regarding operation voltages of the anode, $0 - 1.5$ V, and the cathode, $3 - 4.5$ V, and takes place in a potential range of 2 V to 4 V. Hence, different compositions of non-aqueous electrolyte systems were used throughout Li-ion battery history. Such electrolyte systems consist of a conducting lithium salt that is dissolved in a solvent or solvent-mixture. Therefore, the spectrum is limited to aprotic substances that contain polar groups, such as nitrile, carbonyl, sulfonyl and ether-links, to ensure dissolution of sufficient amounts of lithium salt. Furthermore, these solvents should

- exhibit low viscosity (η),
- be considered chemically inert to other cell components,
- cover a wide temperature range in liquid state,
- operate safely (high flash point T_f) and environmentally friendly.

Thorough investigations of a wide spectrum of non-aqueous polar solvents revealed two classes, *i.e.*, organic esters and ethers, of potential electrolytes for battery application. Polarity, usually quantified by the dielectric constant ϵ, and viscosity range in the same order of magnitude for all applicable ethers. Regarding esters, these two parameters largely depend on the structure. Cyclic esters facilitate solubility of lithium salts, whereas linear analogs exhibit low viscosity and, therefore, promote ion transport [28, 29]. This drastic difference is attributed to intramolecular strain of cyclic esters [30]. Directly after the first successful lithium electrodeposition experiments from dissolved $LiClO_4$ in PC in 1958, propylene carbonate soon became a state of the art electrolyte solvent for lithium batteries [31]. PC combines a high dielectric constant with a low melting point and a high boiling point. Even though static stability with lithium anodes is obtained by formation of a protective layer, PC suffers from severe capacity fade during cycling [32, 33]. This effect is attributed to non-uniform

deposition and dissolution of Li on the metal anode surface leading to contact loss of lithium particles. To overcome this issue, cyclic ethers were employed as solvents and provided much better cycling efficiencies [34]. As reported by Koch and his co-workers, such systems sufficiently suppress the formation of dendritic lithium until charging rates exceed 10 C cm^{-2} [35]. Compared to PC, which is stable up to 5 V vs. Li, the most promising ether candidate, tetrahydrofurane (THF), already exhibits oxidation at 4 V vs. Li [36]. High voltage cathode application, and catalytic surface properties of the same, severely affect the oxidation of this electrolyte and render it unusable for advanced cell compositions [37]. The strive to find electrolyte solvents that unite all requirements set research and manufacturers back to ester based systems. Even though the first report on EC dates back to 1964 [38], its application remained unconsidered until Pistoia *et al.* first described its electrolyte properties at room temperature [39]. To prepare the reported electrolyte, almost 27 wt% $LiClO_4$ were dissolved in EC at 40 °C and resulted in a molal lowering of the freezing point to an average of 5.5 °C. Due to the simplicity of the system, Blagden's law (1.1) can be applied to describe the freezing point depression that is related to the introduction of the conducting salt.

$$\Delta T_F = K_F b i \tag{1.1}$$

Here, K_F denotes the cryoscopic constant, b indicates the molality of conductive salt dissolved per kg of solvent and i is defined as the van 't Hoff factor. According to experimental determination, K_F equals 5.55 K kg mol^{-1} and i, in case of $LiClO_4$, is assumed to be 2 [40]. Calculation, within the boundaries set by Bonner *et al.*, yields a freezing point of 6.7 °C. Further suppression of the freezing point was achieved by addition of co-solvents to EC electrolyte mixtures, or in reverse, using EC as co-solvent to enhance existing electrolytes. Sony largely benefitted from adding EC to the existing PC electrolyte during commercialization of the first generation Li-ion battery. In 1990, formation of the SEI at the interface of graphitic anodes was attributed to the EC content of the electrolyte [41]. To improve the state of the art PC:EC mixture, several co-solvents, including THF derivatives, diethoxyethane and dimethoxyethane, were investigated [42–44]. None of the alterations to the existing formula proved to be a suitable replacement. PC mixtures exhibited severe irreversible capacities during the first cycles, whereas ether mixtures suffered from oxidation reaction at the cathode surface [45]. Tarascon and Guyomard successfully mixed EC with its linear relative dimethyl carbonate (DMC), added various conducting lithium salts to the resulting solution and finally analyzed the properties of these mixtures [46, 47]. Published in 1994, this comprehensive

study established 1 M $LiPF_6$ in EC:DMC (1:1) electrolyte as state of the art in Li-ion cells. It features a voltage breakdown of more than 5.1 V against Li at RT, ionic conductivity of 11 mS cm^{-1} and a freezing point equal to −20 °C. Changes in ratio between the 2 solvent components leads to different conductivities and also affects the boiling point of the mixture. Except some variations to the component ratio, also considering 3 component mixtures, this electrolyte composition is still used in many commercial cells today as it was introduced to the 3rd generation of Sony's Li-ion battery in 1994. $LiPF_6$ is a commercially unchallenged electrolyte solute, it combines stability against high voltage cathodes with the ability to successfully passivate aluminum current collectors [48, 49]. Its major drawbacks are described as thermal instability and high sensitivity towards moisture. Operation at temperatures exceeding 50 °C leads to severe decrease in conductivity, which is a result of electrolyte decomposition and formation of fluorinated derivatives [50, 51]. Several alternatives surfaced throughout the years, but none of them covers the wide range of distinct requirements as successfully as $LiPF_6$.

2.1.1 Lithium Borate Salts

In parallel to the investigation of $LiPF_6$, other lithium conducting solutes were explored. After commercialization of the first Li-ion cell, $LiBF_4$ was studied in more detail to expand the thermal operation window of Li-ion systems [47, 52]. This solute ensures operation at a maximum temperature of 60 °C, which is a slight increase compared to ⩽ 50 °C for $LiPF_6$. Additionally, lower capacity fade was observed at moderate temperatures from 20 to 25 °C [53]. At low temperatures, however, suppression of the freezing point is not sufficient to enable cell operation at −20 °C without severe capacity fade. An effect that can easily be ascribed to lower charge-transfer resistance resulting from presence of $LiBF_4$ in the electrolyte mixture [54]. Furthermore, electrochemical stability exceeding 3.5 V vs. Li is not granted and, as a consequence, renders this solute incompatible with high voltage cathode materials [55].

To boost stability at high potentials, the more complex lithium *bis*(oxalate)-borate (LiBOB) was introduced [56]. Unexpectedly, LiBOB forms a highly potent electrolyte with PC that is able to generate an SEI on graphite to prevent exfoliation. Due to the absence of fluorine-ions, corrosion of the aluminum current collector is successfully reduced and a passivating layer is formed during cycling [57]. In combination with a $LiFePO_4$ cathode and EC as solvent,

LiBOB enables stable cycling at temperatures as high as 100 °C [58]. Regarding electrochemical stability of resulting electrolytes, application of potentials up to 5 V vs. Li does not entail electrolyte decomposition [59]. As reported by Cui *et al.*, a 1 M LiBOB γ-butyrolactone / sulfolane / DMC (1:1:1) electrolyte mixture performed 100 cycles retaining 85.9 % of the initial discharge capacity in a $LiNi_{0.5}Mn_{1.5}O_4$/Li half-cell arrangement [60]. Its major disadvantages comprise extensive SEI formation, which leads to increasing resistance at the anode surface, and low solubility compared to $LiPF_6$ [61, 62]. Alongside these adverse effects, which limit LiBOB to certain operation conditions, the enhancement of temperature stability in $LiPF_6$ containing electrolytes renders this material an excellent electrolyte additive [63].

Advanced understanding of decomposition processes in lithium borate electrolytes concluded in creation of $LiBF_2C_2O_4$ (LiODFB). Figure 2.3 provides the structure formula of both LiBOB and LiODFB. The latter carries a mixture of both oxalate and fluorine terminations at the boron based anion. This feature empowers LiODFB to merge the advantages of $LiBF_4$ and LiBOB. Hence, LiODFB extends thermal stability (> 60 °C and < −10 °C), efficiently passivates the Al current collector up to potentials of 6 V, reduces irreversible capacities during formation of a temperature stable SEI and enhances performance in

PC containing solvent mixtures [64–67]. Considering the requirements for battery application, this material exceeds the performance of the commonly used $LiPF_6$-based electrolytes. However, presence of moisture and oxalate impurities in the electrolyte mixture, originating either from synthesis of the material or electrolyte solvents, adversely affect cell performance [65].

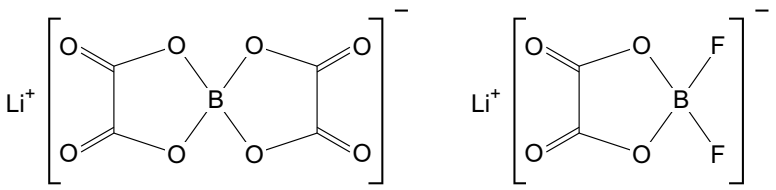

Figure 2.3: Structural formula of LiBOB and LiODFB

2.1.2 Lithium Imide Salts

Lithium imides, and their most prominent representatives $LiN(SO_2CF_3)_2$ (LiTFSI) and $LiN(SO_2F)_2$ (LiFSI), exhibit enhanced low and high temperature stability and form durable SEI layers. Futhermore, this class of solutes is considered highly stable against hydrolysis at standard operating conditions [68, 69]. Incorporated heteroatoms, in the structures of LiTFSI and LiFSI, respectively, grant high conductivity and serve as charge centers. In addition, $-CF_3$ groups draw electrons to increase solubility in carbonate solvents. Regarding DMC-based solutions, LiFSI solute concentrations of up to 5 M can be accomplished [70].

As reported by Krause *et al.*, electrolytes containing lithium imides are prone to corrode aluminum current collectors at potentials between 3.6 V and 4.5 V [71]. On one hand, this aspect renders LiTFSI and LiFSI unusable in combination with high voltage cathodes, on the other hand, systems equipped with $LiFePO_4$ cathodes largely benefit from the enhanced temperature stability and outstanding conductivity of those solutes [70].

The most suitable $LiPF_6$ replacement among lithium imide representatives is $LiN(SO_2C_2F_5)$, often referred to in its abbreviated form LiBETI, which combines all previously mentioned advantages and enhanced corrosion stability towards Al current collectors [72]. Figure 2.4 highlights the differences between the exact structures of the aforementioned lithium imide salts. Compared to its previously discussed relatives, corrosive properties of LiBETI are shifted towards much higher potentials, viz., from 3.55 V (LiTFSI) to 4.5 V [71]. Corrosion stability towards Al is granted by formation of a passivating layer with a thickness ranging between 500 nm and 1 µm [72]. These features facilitate its utilization as electrolyte salt in state of the art cells equipped with cathode materials like $LiCoO_2$.

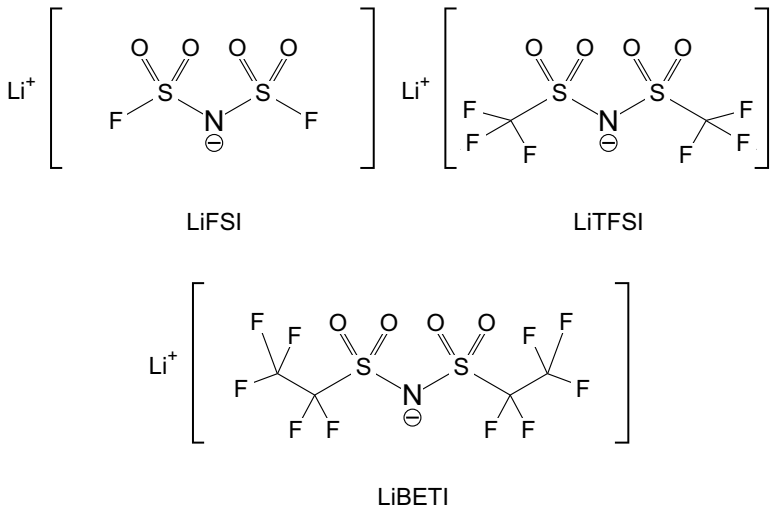

Figure 2.4: Structural formula of LiFSI, LiTFSI and LiBETI

2.2 Solid Electrolytes

First records of ionic conduction in solids date back to the early 19th century when Michael Faraday reported on conduction in heated Ag_2S and PbF_2 [73]. The foundation for solid-state electrolytes and their application in battery systems was lain in 1943, when Kato and Yamaguchi first synthesized $Na-\beta-Al_2O_3$ ($Na_2O \cdot 11Al_2O_3$) [74]. J.T. Kummer and his team recognized the potential of this 2D sodium-ion conductor and developed the first Na–S solid-state battery. In 1966, a patent comprising the construction of an all-solid-state battery (ASSB), which uses molten Na metal as anode and a molten sulfide-based cathode material, was filed by the Ford Motor Company [75]. To achieve sufficient ionic conductivity and surface wetting of the $Na-\beta-Al_2O_3$ electrolyte, operation

temperatures of these cells were kept steady at 300 °C. First steps to improve this system included application of $FeCl_2$ or $NiCl_2$ embedded in an iron matrix that is surrounded by $NaAlCl_4$ electrolyte. This cathode material enables lowering of the operating temperature to 250 °C [76, 77]. Molten sodium batteries comprising these metal chloride cathodes were given the name ZEBRA, an abbreviation for Zero Emission Battery Research Activity, the name of its founding research facility. Protection of intellectual property and, therefore, the interest in commercialization of this technology was already evinced in 1974 by ESB Inc. [78]. Advantages in safety such all solid state systems aroused growing interest in room temperature application of solid-state electrolytes (SSE). In general, suitable electrolyte materials are divided into organic and inorganic SSEs.

2.2.1 Polymer-Based Solid Electrolytes

In the 80s first attempts pursued the application of organic, viz., polymer, electrolytes by investigating various compositions based on poly(ethylene oxide), furthermore abbreviated as PEO [79]. Polymer electrolytes are classified in three systems, viz., dry polymer, gel polymer and composite polymer. Since dry polymer electrolytes, *i.e.*, a mixture of PEO and a conducting salt, suffer from

conductivity depression below the melting point of PEO, multi-component mixtures entered the focus of research [80]. Adding another component yields gel polymer electrolytes that usually consist of a polymer matrix (PEO), a conducting salt ($LiClO_4$ or $LiCF_3SO_3$) and a plasticizer (EC, PC, Polyethylene glycol (PEG) or derivatives thereof) [81]. Even though these improvements lead to an increase in conductivity, PEO based polymer electrolytes cannot exceed a limit of $10^{-3}\,S\,cm^{-1}$. To further enhance the conductivity of polymer electrolytes, numerous reports suggested alternatives to the PEO polymer matrix, such as, polyacrylonitrile (PAN) [82], poly(methyl methacrylate) (PMMA) [83], poly(vinyl sulfone) (PVS) or poly(vinylidene fluoride) (PVdF) [84, 85]. Replacement of the aforementioned plasticizers and conducting salts by classic liquid electrolyte mixtures was considered a beneficial change in composition of gel polymer electrolytes. A combination of several optimization steps granted conductivities up to $10^{-2}\,S\,cm^{-1}$ [84]. A contrary approach, viz., incorporation of ceramic fillers in the polymeric host material, yielded the class of composite polymer electrolytes. Here, a differentiation between active and passive filler materials must be drawn. Active fillers affect the conduction mechanism, whereas their passive analogs only affect the glass transition temperature of the polymer matrix [86]. In combination with a conducting salt ($LiCF_3SO_3$),

the most prominent example of the former, viz., $\gamma-LiAlO_2$, achieved reasonable cycling efficiency [87]. Inert fillers, such as TiO_2, Al_2O_3, SiO_2 or $BaTiO_3$, enhance the electrolyte properties by decreasing the interfacial resistance between electrode and electrolyte. In further consequence, this reduction in resistance leads to improved cycling performance [88, 89]. Composite polymer electrolytes, regardless of the filler activity, are often dosed with Li conducting salts to enhance ionic conductivity of the overall mixture. To further increase the performance, ceramic-in-polymer electrolyte compositions were created by incorportation of ceramic electrolyte particles, viz., those exhibiting high ionic conductivity, into polymer matrices. Figure 2.5 sketches a ceramic-in-polymer electrolyte and compares it to its close relative polymer-in-ceramics, which will be discussed later on. Extensively investigated polymers like PEO and PAN were used as matrices for nanostructured oxide electrolyte ceramics, such as, $Li_{0.33}La_{0.56}TiO_3$ or $Li_{6.4}La_3Zr_{1.4}Ta_{0.6}O_{12}$, and yielded conductivities

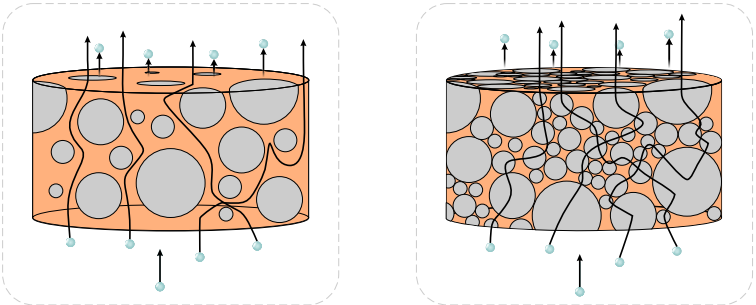

Figure 2.5: Comparison between polymer-in-ceramics and ceramics-in-polymer systems.

in the mS cm^{-1} range [55, 90]. Besides high conductvities, reports show that dendrite growth is suppressed when omitting Li conducting salts in PEO-based ceramic-in-polymer electrolytes [90]. Three dimensional structuring of the used ceramics can lead to enhanced stability of the electrolyte mixture and plating and stripping of Li can be ensured for at least 1000 cycles [91]. Latest progressions head towards polymer loaded ceramic electrolytes, viz., polymer-in-ceramic, that make use of polymers to enhance connection between ceramic particles to overcome low grain boundary conductivities [92]. Additionally, these mixtures enable facile and scalable preparation of thin flexible films by simple processing methods like spray painting [93].

2.2.2 Thin Films

In parallel to its organic relatives, advanced processing techniques for inorganic solid-electrolytes, in particular lithium phosphorous oxynitride (LiPON), caught attention in this field of research [94]. Bates *et al.* introduced radio-frequency sputtering as suitable method to prepare thin film battery systems based on LiPON electrolyte [95]. This method enables direct application of thin layered amorphous LiPON on a broad variety of electrode materials and, therefore, facilitates implementation of such batteries in micro-devices [96,

97]. To optimize the performance of such thin film batteries, alternatives like lithium borophosphate were investigated to replace the state of the art glassy LiPON electrolytes [98, 99]. Its main advantages over LiPON constitute of a less sophisticated sputtering process, resulting in better reproducibility, and enhanced ionic conductivity [100]. Further proceedings substituted the radio-frequency sputtering process by atomic layer deposition and accomplished an optimization of the deposited layers [101]. This method made a large variety of materials, *i.e.*, $(Li, La)_xTi_yO_z$ [102], $Li_xAl_2O_3$ [103], Li_3PO_4 [104], LiPON [105], and $Li_xAl_ySi_zO$ [106], accessible for electrode application in thin layer batteries. Among this variety, LiPON is the most successful commercially available thin film electrolyte that provides high cycling, electrochemical and chemical stability. Cells containing $LiNi_{0.5}Mn_{1.5}O_4$ cathodes and Li anodes were tested for 10,000 cycles at high charging rates (5 C) and achieved excellent capacity retention [107]. Ceramic electrolytes First compounds considered for application as solid electrolytes, as already mentioned, were different compositions of $Na-\beta-$alumina and already known in the 1940s. Its first class of competitors, viz., $NaM_2(PO_4)_3$ with M = Ge, Ti or Zr, entered the spotlight in the late 60s [108]. Clearfield *et al.* assigned the ability of ions to diffuse through its lattice to zeolite-like cavities that provide enough room to accommodate ions [109].

At temperatures exceeding 850 °C, XRD proved an irreversible crystallographic change of $KTi_2(PO_4)_3$ from its cubic polymorph to a rhombohedral phase that is also accompanied by a change in color from blue to white [110]. In 1976, J.B. Goodenough *et al.* reported on high ionic conductivity of rhombohedral $Na_{1+x}Zr_2P_{3-x}Si_xO_{12}$ in which Na^+ ions could easily be exchanged with Li^+, Ag^+ or K^+ ions. These findings laid the foundation for the class of NASICON materials, an abbreviation for Na super ionic conductors, with a general formula of $A_xMM'(XO_4)_3$. A sites can be occupied by the previously mentioned cations, M and M′ transition metals like Fe, V, Ti, Zr, Sc, Mn, Nb or In occupy the centers of $M(')O_6$ octahedra, and X denotes S, P, Si or As cations residing on center sites of XO_4 tetrahedra [111]. Large freedom to tailor the properties of this material class led to growing research interest and spawned a large variety of compounds crystallizing in NASICON structure.

At first, several research groups focused on synthesis of new electrode materials by incorporation of Fe or V on the M(′) lattice site and P, S, Mo or W in the tetrahedral centers [112–115]. Operation of Li based systems is granted at stable conditions with a mixture of PO_4 and SO_4 ($LiFe_2(SO_4)_2(PO_4)$ [116]. Electrodes equipped with MoO_4 or WO_4 are able to intercalate Na^+ or Li^+ and perform a two-electron transfer that yields a storage capacity of roughly

120 mA h g^{-1} [117–119]. Replacement of Fe with Vanadium results in a cathode material commonly known as LVP, an abbreviation for $Li_3V_2(PO_4)_3$, which exhibits high cyclability at equally high operation potentials [120]. However, LVP suffers from low electric conductivity that is usually overcome by carbon coating to establish good electric contact [121, 122]. After this optimization process, the material is operated at potentials as high as 4.8 V and yields reversible capacities of 197 mA h g^{-1}, although the cycle life is not very long due to electrolyte instability [123].

A small change in composition, viz., exchange of V by Ti, yields $LiTi_2(PO_4)_3$, one of the most successful NASICON electrolytes [124–126]. However, in direct contact with metallic lithium this electrolyte material is prone to reduction of the Ti^{4+} centers to Ti^{3+}, whcih results in electronic conduction [127]. This detrimental factor was suppressed by partial substitution of Ti^{4+} for Al^{3+} and, therefore, yielding $Li_{1+x}Al_xTi_{2-x}(PO_4)_3$ [128]. Optimization of the preparation method, as well as the composition, yielded an enormous increase in long range ion mobility that results in bulk contributions up to 3.4×10^{-3} S cm^{-1} and grain boundary contributions up to 8.9×10^{-6} S cm^{-1} at room temperature [129–131]. Latest reports pursue the back to the roots approach and focus on compositions like $Na_3Zr_2(SiO_4)_2(PO_4)$ [132]. Substitution of Zr, which resides

on octahedral lattice sites, with small quantities of Sc results in enhanced room-temperature ionic conductivities up to $4 \times 10^{-3}\,\mathrm{S\,cm^{-1}}$ [133, 134]. Its high thermal and chemical stability as well as its fast ion dynamics render this material a highly potent candidate for ASSB application.

2.2.3 Perovskite Systems

Similar adverse effects are observed for the perovskite class of solid electrolytes. In the early 90s $Li_{3x}La_{2/3-x}TiO_3$, a well known representative of the perovskite class that was first reported in 1953 [135], caught up with NASICON materials in terms of room temperature bulk conductivity [136]. As a consequence of high grain boundary resistances, the total conductivities of these compounds settle around $10^{-5}\,\mathrm{S\,cm^{-1}}$ [137]. Additionally, the aforementioned reduction of Ti^{4+} in direct contact with Li metal renders this class of materials unusable for battery application. Electrochemical characterization performed by Bohnke *et al.* determined short circuit conditions at cathodic potentials above 2.8 V. Furthermore, application as electrode material is limited by its ability to intercalate only small amounts of Li [138]. The success of early approaches to implement perovskites in fuel cells pushed further research activities into other directions [139–142]. Latest developments in ASSB and beyond Li-ion research

show recurring interest in perovskite and antiperovskite electrolytes [143–147].

2.2.4 Garnet-Type Solid Electrolytes

Garnet-type materials refer to the general garnet formula $A_3B_2Si_3O_{12}$, in which A exhibits eightfold coordination and B is sixfold coordinated. Known as gemstone for thousands of years, the lithium diffusivity of a close relative, viz., $Li_5La_3M_2O_{12}$ (M = Nb or Ta), was first reported by Thangadurai *et al.* in 2003 [148]. This garnet electrolyte featured total conductivities up to $10^{-6}\,S\,cm^{-1}$ at RT and was, therefore, highly competitive to other solid electrolytes. In order to optimize the ionic conductivity, connections to the origin of the ion diffusivity had to be drawn. A Li_3-phase, viz., $Li_3Ln_3Te_2O_{12}$ (Ln = Y, Pr, Nd, Sm-Lu), published in 2006 exhibited much lower conductivity [149]. Further experiments revealed low mobility of tetrahedrally coordinated Li as opposed to its analog residing on octahedral sites. The introduction of lithium to unoccupied octahedral sites, achieved by addition of lithium and partial substitution of Te with Sb, leads to an increase in conductivity by 2 orders of magnitude [150]. Hence, research focused on optimization of the Li_5-phase reported in 2003. Structural elucidation identified the cubic space group of the garnet $Ia\bar{3}d$ and located Li ions on $24d$ and $96h/48g$ lattice sites [151]. Figure 2.6 represents the

crystal structure in its cubic phase and highlights the most important features.

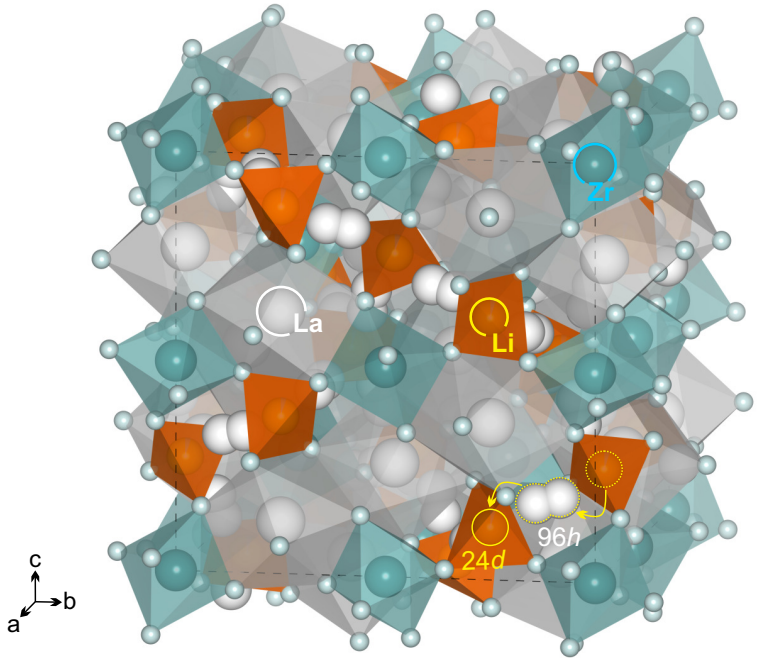

Figure 2.6: Crystal structure of cubic garnet-type LLZO. Lithium ions and dopants are indicated by color and labels.

Partial or full substitution of Nb/Ta in $Li_5La_3M_2O_{12}$ yields an increase in lattice parameters, but does not beneficially affect conductivity [152, 153]. The Li_6-phase is introduced by substitution of La^{3+} with divalent cations like Ca^{2+} or Ba^{2+}. This operation does not only increase the lattice parameter, it also affects the occupation shares of lattice sites. In Li_5-phases the charge carriers reside, to an extent of about 80 %, on tetrahedral 24*d* lattice sites and smaller amounts, viz., 14 %, can be located at the 48*g* octahedral sites. When higher

amounts of Li^+ and alkaline earth metals are introduced to the structure, *i.e.*, $Li_{5+x}Ba_xLa_{3-x}Ta_2O_{12}$ with x = 1.6, the occupation of 24d sites decreases to 14 % and 48g lattice sites are predominantly filled to an extent of 57 % [154]. This effect is a result of changes in lattice parameters and affects ion mobility. Further, increasing lattice parameters and the negative impact on ionic conductivity are closely connected to increasing sintering temperatures [155]. Assuming that introduction of more Li^+ into the garnet structure will lead to enhanced ionic conductivity, the first Li_7 garnet phase, viz., $Li_7La_3Zr_2O_{12}$ (LLZO) entered the spotlight in 2007 [156]. Samples annealed at 1230 °C exhibit total conductivities between 2.44 × 10^{-4} S cm^{-1} and 7.74 × 10^{-4} S cm^{-1}. As reported by Awaka *et al.*, minor changes in the synthesis route, such as, annealing samples at 980 °C, leads to formation of the tetragonal polymorph in the space group $I4_1/acd$. Tetragonal garnets exhibit much lower bulk conductivities of ≈ 10^{-6} S cm^{-1} at 300 K, a fact that is evidentially attributed to site occupancy of Li atoms [157]. Whereas the Li – vacancy disordering between tetrahedral and octahedral lattice sites enables fast ionic motion in the cubic polymorph, the completely ordered Li – vacancy site occupancy and lack of equivalent Li positions entail much slower ion dynamics in the tetragonal structure [157, 158]. These differences were also backed by *ab-initio* molecular

dynamics simulations, which differentiate between synchronous collective mechanism and asynchronous mechanism of single-ion jumps, as reported by Meier *et al.* [159]. Striving for higher conductivities, heterovalent doping was reported as suitable method to stabilize the preferred cubic polymorph at much lower annealing temperatures, *i.e.*, between 900 °C and 1100 °C [160, 161]. Introduction of Al^{3+}, which supposedly resides on Li^{+} lattice sites, to the LLZO structure results in creation of 2 Li^{+} vacancies and, therefore, enhances conductivity [160]. To reveal the location of Al ions in the LLZO lattice, ^{27}Al magic angle spinning (MAS) nuclear magnetic resonance (NMR) was employed. Alongside other experimental techniques and calculations, the residence of Al ions was located at 24*d* lattice sites, and to a smaller extent also 96*h* sites, and entails beneficial effects on ionic conductivity [162–164]. Furthermore, partial substitution of Li^{+} with Ga^{3+} or Zr^{4+} with Ta^{5+} stabilizes the cubic LLZO polymorph and leads to increased conductivities of 3.5×10^{-4} S cm^{-1} and 8.7×10^{-4} S cm^{-1}, respectively [165, 166]. On one hand, within certain boundaries increasing dopant concentrations were proven to beneficially affect ionic conductivity and phase stabilization [162, 167]. On the other hand, simultaneous co-doping at Li and Zr sites results in lower ionic conductivities, suggesting that the Li pathway is adversely affected by aliovalent dopants at 24*d* lattice

sites [166]. Bottke *et al.* employed NMR spectroscopy on Mo-doped LLZO to resolve the $96h - 24d - 96h'$ Li conduction path in the cubic polymorph [168]. These findings overlapped with results from an investigation of single crystalline Ta substituted LLZO that exhibited correlated Li ion motion along the same path [169]. Wachter-Welzl *et al.* reported on the highest effective conductivity, viz., 5.7×10^{-4} S cm^{-1} at 25 °C, by substituting 0.25 Li per formula unit (pfu) with Al [170, 171]. Moreover, they demonstrate that inhomogeneous substituent distribution in Al-stabilized polycrystalline materials results in conductivity variations of more than one order of magnitude. This theory is in good agreement with recent simulations that reveal blocking of Li ion motion in close proximity to Al ions [172]. Substitution by Ga, however, enables limited Li diffusion in its close surrounding and, therefore, exhibits higher ionic conductivities [172–174]. A variety of techniques, including single crystalline XRD, powder XRD, SEM, NPD and ^{7}Li NMR, was used to closely investigate structural properties of Ga-stabilized LLZO and revealed its acentric cubic $I-43d$ (no.220) structure [175]. Outstanding chemical and thermal stability, as well as high ionic conductivity render Al, Ga or Ta stabilized cubic LLZO ceramics highly potent candidates for ASSB application. Interfacial issues related to fabrication of Li-metal ASSB, especially concerning poor wettabil-

ity of garnet electrolyte surfaces, posed a problem during the past few years [176–178]. Suggested solutions to this problem are application of an interlayer [179, 180] and surface treatment, *i.e.*, polishing [181]. Recent publications also address dendrite growth through dense LLZO ceramics [182] and even single crystals [183] and suggest application of an interlayer to prevent such events [184].

2.2.5 Sulfide-Based Systems

Sulfide based solid electrolytes entered the research spotlight in 1986, when Kennedy *et al.* performed first conductivity measurements on SiS_2 – Li_2S glasses [185]. Before the last heating and quenching step, Li-salts like LiCl, LiBr or LiI were added to the ground glass to enhance its ionic conductivity. Such glassy solid electrolytes bearing LiI contents of 30 molar %, exhibit ionic conductivities of $8.2 \times 10^{-4}\,\mathrm{S\,cm^{-1}}$ at 25 °C [186]. In 2000, Kanno *et al.* introduced a new class of fast Li-ion conducting electrolytes called thio-LISICON, an abbreviation for Li superionic conductor, based on the composition Li_2S-GeS_2. Materials that belong to this class crystallize in an orthorhombic system closely related to $\gamma-Li_3PO_4$. As demonstrated in the case of Li_4GeS_4, these ceramic systems are capable to reach ionic conductivities as high as $2 \times 10^{-7}\,\mathrm{S\,cm^{-1}}$ at

25 °C [187]. Further refinement of the system, *i.e.*, substitution of Ge^{4+} + Li^{+} with P^{5+}, resulted in formation of Li_2S-GeS_2-P_2S_5 that is accompanied by an enormous boost in conductivity. The general formula for the thio-LISICON family was determined to be $Li_{4-x}M_{1-x}M'_xS_4$ with Si or Ge residing on M sites and P, Al, Zn or Ga located at M' sites. The structure offers a 3-dimensional framework for Li diffusion that is composed of MS_4 and M' S_4 tetrahedra. Substitution with x = 0.75 P (M′) in a Ge-based system leads to conductivities as high as 2.2×10^{-3} S cm^{-1} at 25 °C. Additionally, this composition exhibits high thermal, viz., up to 200 °C, and electrochemical stability from −0.5 V up to 5 V vs. Li [188]. Aiming for faster ion dynamics, a glass ceramic electrolyte based on the system Li_2S-P_2S_5, usually described by mol% of the 2 components, exhibited an increase in Li diffusivity. Changes in the preparation procedure of $70Li_2S{\cdot}30P_2S_5$, in particular the change from mechanical milling to melt quenching, resulted in increase of the ionic conductivity from 3.2×10^{-3} S cm^{-1} to 4.1×10^{-3} S cm^{-1} at 25 °C [189, 190]. In 2013 Liu *et al.* reported on a highly conductive nanocrystalline phase of Li_3PS_4 that is considered the most stable compound emerging from the Li_2S-P_2S_5 system [191]. Alongside a reasonable RT conductivity of 1.6×10^{-4} S cm^{-1}, β−Li_3PS_4 exhibits negligible interfacial resistance and outstanding cycling behavior in Li plating and strip-

ping experiments at elevated temperatures. Mixtures of said phase with cubic LLZO, in a molar ratio of 7 : 3, facilitate the mechanochemical manufacturing process, improve mechanical stability and result in an increase in diffusivity [192]. Introducing lithium halides, in particular LiI, to the $\beta-Li_3PS_4$ structure, yields a $Li_7P_2S_8I$ phase that withstands reactions with Li up to a potential of 10 V and triples the initial conductivity [193]. Nowadays, thio-LISICON and $\beta-Li_3PS_4$ systems are still in the spotlight of research. Introduced in 2011, $Li_{10}GeP_2S_{12}$ reaches conductivities as high as commercial organic electrolytes [194]. Nonetheless, major drawbacks of sulfide-based solid electrolytes consist of sensitivity towards moisture as well as the tendency to form decomposition layers at the electrodes to maintain electrochemical stability [195, 196].

CHAPTER 3

FUNDAMENTALS OF DIFFUSION

3.1 Diffusion in Solids

Solid electrolytes rely on the hopping of a mobile species along the sites of their crystal lattice. High performance is granted by open lattice, channel or layered structures that enable free motion of small cations. Similar to gases, glassy solids, polycrystalline materials without texture and most liquids, diffusion in cubic solid electrolyte materials is of isotropic nature and regarded as a scalar quantity. Hence, one can make use of Fick's laws to describe ionic motion in these materials. According to Fick's first law, the diffusion flux (J_x) in one

dimension (x) is connected to the ion concentration (C).

$$J_x = -D\frac{\partial C}{\partial x} \tag{1.1}$$

Diffusion is considered a process to equalize concentrations and, therefore, the negative sign next to the species dependent diffusion coefficient (D), viz., the right-hand side term, indicates changes in concentration opposite to that of the diffusive flux. A closer look at the units for C ($\mathrm{mol\,m^{-3}}$), x (m) and D ($\mathrm{m^2\,s^{-1}}$) reveals the unit of the diffusive flux ($\mathrm{mol\,m^2\,s^{-1}}$). A three dimensional approach utilizes vector notation to apply Fick's first law.

$$\boldsymbol{J} = -D\nabla C \tag{1.2}$$

Here, the vector of the diffusion flux $\boldsymbol{J}$ is in antiparallel orientation to the concentration-gradient vector ∇C. This vector is expressed by an interaction of the *nabla* operator ∇ with the scalar concentration field $C(x, y, z, t)$. Thus, the magnitude of ∇C equals the maximum rate of increase in concentration at the point where the concentration field undergoes the fastest increase. Diffusion processes in an ideal system conserve the amount of diffusion particles, whereas the continuity equation is applied for species that obey a conservation law. This equation links the accumulation rate, *i.e.*, the material balance between inflow and outflow, to the partial time derivative of the concentra-

tion. The specification of an infinitesimal sized test volume introduces the divergence $\nabla\cdot$ that expresses the vector of the diffusion flux.

$$-\nabla\cdot\boldsymbol{J}=\frac{\partial C}{\partial t} \tag{1.3}$$

Fick's second law, often referred to as the "diffusion equation", combines (1.2) with (1.3) and is, therefore, a partial differential equation of second-order. Hence, linearity of the equation solely depends on the diffusion coefficient. In case of diffusion governed by a chemical composition gradient, D is labeled interdiffusion coefficient and the resulting equation is considered non-linear.

$$\frac{\partial C}{\partial t}=\nabla\cdot(D\nabla C) \tag{1.4}$$

In ideal solutions or chemically homogeneous systems, diffusivity is independent of ion concentration and denoted as D^{tr}. These boundaries simplify Fick's second law to a linear second-order partial differential equation in which the Laplace operator Δ acts on the concentration field $C(x, y, z, t)$.

$$\frac{\partial C}{\partial t}=D^{\mathrm{tr}}\Delta C \tag{1.5}$$

In anisotropic materials diffusion properties are heavily influenced by diffusion direction. Anisotropy in non-cubic single crystals, composite materials, textured polycrystals and decagonal quasicrystals manifests in interactions

between the concentration gradient and the diffusion flux. More precisely, the direction of the diffusion flux is not square to the surface of constant concentration. Fick's first law for anisotropic materials drastically differs in boundary conditions from that for isotropic media, as seen in (1.2).

$$\boldsymbol{J} = -\boldsymbol{D}\nabla\boldsymbol{C} \tag{1.6}$$

Here, $\boldsymbol{D}$ is a symmetric second-rank diffusivity tensor [199]that can be transformed to its three orthogonal principal axes

$$\begin{pmatrix} D_1 & 0 & 0 \\ 0 & D_2 & 0 \\ 0 & 0 & D_3 \end{pmatrix}, \tag{1.7}$$

in which D_1, D_2 and D_3 denote principal diffusion coefficients. Additional independent parameters p, *i.e.*, related to symmetry of the crystal structure and present in variable quantities $p \leqslant 6$, affect diffusion by defining $p-3$ orientations of the principal axes in anisotropic media. Integer values for p ascend from 1 to 6 according to the structure and the progression

$$\text{cubic} < \begin{matrix} \text{hexagonal} \\ \text{tetragonal} \\ \text{rhombohedral} \end{matrix} < \text{orthorhombic} < \text{monoclinic} < \text{triclinic}$$

Assuming the case that diffusion flux $\boldsymbol{J}$ and the concentration gradient $\nabla \boldsymbol{C}$ point towards different directions, relevant components of $\boldsymbol{J}$ and principal diffusion axes (x_1, x_2, x_3) yield the relations

$$\begin{aligned} J_1 &= -D_1 \frac{\partial C}{\partial x_1}, \\ J_2 &= -D_2 \frac{\partial C}{\partial x_2}, \\ J_3 &= -D_3 \frac{\partial C}{\partial x_3}. \end{aligned} \tag{1.8}$$

For defined directions of the principal diffusion axes, obtained diffusion coefficients completely describe anisotropic diffusion. Starting from direction angles $\Theta_1, \Theta_2, \Theta_3$

$$\alpha_1 \equiv \cos\Theta_1,\ \alpha_2 \equiv \cos\Theta_2,\ \alpha_3 \equiv \cos\Theta_3 \tag{1.9}$$

the diffusion coefficient for the defined direction can be described by

$$D(\alpha_1, \alpha_2, \alpha_3) = \alpha_1^2 D_1 + \alpha_2^2 D_2 + \alpha_3^2 D_3. \tag{1.10}$$

Crystals that defined by $p \geqslant 3$ exhibit 3 different principal diffusivities. Even though principal axes of diffusion coincide with the axes of crystallographic symmetry in orthorhombic structured materials, the previously mentioned relation, viz., (1.11), applies.

$$D_1 \neq D_2 \neq D_3 \tag{1.11}$$

The relation between diffusion coefficients in uniaxial materials, which are characterized by $p = 2$ and exhibit a unique axis that is arranged in parallel to the x_3–axis, is described by

$$D_1 = D_2 \neq D_3. \tag{1.12}$$

Due to existence of only one angle Θ between diffusion flux and crystal axis, (1.10) simplifies to

$$D(\Theta) = D_1 \sin^2\Theta + D_3 \cos^2\Theta. \tag{1.13}$$

In isotropic systems the diffusivity tensor reduces to a scalar quantity and boundaries of isotropic diffusion apply. For these systems the relation holds.

$$D_1 = D_2 = D_3 \equiv D \tag{1.14}$$

3.2 Diffusion at the Atomic Scale – Random Walk Theory

Regarding unforced uniaxial diffusion of an atom to one of its 6 nearest interstitial sites displays, in a simple but effective way, that the diffusion coefficient is a product of jump rate and the square of the jump distance. Considering an

atomic flux J between two lattice planes at a certain jump rate Γ

$$J = \Gamma n_1 - \Gamma n_2, \tag{2.1}$$

and taking into account that the quantitites n of the interstitials can also be expressed as concentrations C per jump length λ

$$C_\mathrm{i} = \frac{n_\mathrm{i}}{\lambda}, \tag{2.2}$$

in combination with a Taylor expanded concentration-distance function

$$C_1 - C_2 = -\lambda \frac{\partial C}{\partial x}, \tag{2.3}$$

a diffusion equation similar to that of Fick's first law can be composed.

$$J = -\lambda^2 \Gamma \frac{\partial C}{\partial x} \tag{2.4}$$

Compared to (1.2), the diffusion coefficient can be denoted as

$$D = \Gamma \lambda^2, \tag{2.5}$$

and considering a simple cubic lattice as diffusion medium, in which the total jump rate can be regarded as $\Gamma_\mathrm{tot} = 6\Gamma$, a diffusion coefficient

$$D = \frac{1}{6} \Gamma_\mathrm{tot} \lambda^2 \tag{2.6}$$

is obtained.

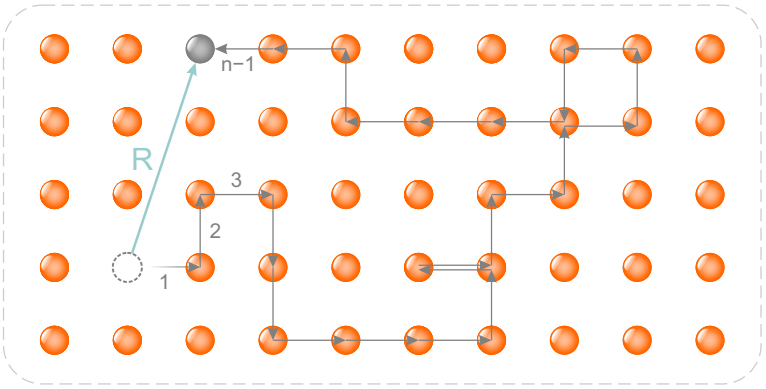

Figure 3.1: Uncorrelated random walk of a species along the lattice sites. Each grey arrow indicates a hopping process from one lattice site to the other. The total displacement is highlighted by a big aqua colored arrow from the initial site, drawn as a dashed circle, to the final site and the letter R. This illustration is based on Ref. [197].

3.2.1 Einstein-Smoluchowski Relation

The composition of the total displacement of particles, as illustrated in Figure 3.1, is described along the axes of a coordinate system as

$$R^2 = X^2 + Y^2 + Z^2. \tag{2.7}$$

For the sake of simplicity, atomic motion in the following derivation is only regarded in X-direction. Furthermore, the distribution function $W(X,\tau)$ is introduced to describe the probability of a atomic displacement along the x-projection X during a time τ. According to $\tau = t - t_0$, τ is defined as the time of the random walk. A concentration of diffusing particles C in a plane x at the time $t+\tau$ can be regarded as the sum of the same particles diffusing from other

planes following a certain distribution function.

$$C(x, t+\tau) = \sum_X C(x-X, t) W(X, \tau) \tag{2.8}$$

Expanding concentration related terms around $X = 0$ and $\tau = 0$ and defining the normalized distribution function in n^{th}-moments of X

$$\langle X^n \rangle = \sum_X X^n W(X, \tau), \tag{2.9}$$

yields an expression for the change in concentration by time

$$\frac{\partial C}{\partial t} = -\frac{\langle X \rangle}{\tau} \frac{\partial C}{\partial x} + \frac{\langle X^2 \rangle}{2\tau} \frac{\partial^2 C}{\partial x^2}, \tag{2.10}$$

assuming that higher order terms on the both sides are negligible due to very small values of τ. The magnitude of τ governs higher order terms of left-hand side term due to its expansion around $\tau = 0$, and the right-hand side term by increasing localization of the distribution function around $X = 0$. A closer look at the first term on the right-hand side of 2.10 reveals its purpose as drift term and considering the absence of driving force allows reduction of the equation according to Fick's second law (1.4) and yields the following expression for the diffusion coefficient

$$D_x = \frac{\langle X^2 \rangle}{2\tau}. \tag{2.11}$$

Analogous equations can be formulated along other directions of the coordinate system, viz., y and z. Regarding diffusion in an isotropic medium, *e.g.*, a cubic crystal, symmetry simplifies the displacements to

$$\langle X^2 \rangle = \langle Y^2 \rangle = \langle Z^2 \rangle = \frac{1}{3} \langle R^2 \rangle, \tag{2.12}$$

and yields the Einstein-Smoluchowski relation

$$D_x = \frac{\langle R^2 \rangle}{6\tau}. \tag{2.13}$$

The random walk theory differentiates in two cases of motion, viz., correlated and uncorrelated random walks. The former, as illustrated in Figure 3.1, distinguish jump directions by probability, *i.e.*, the reciprocal coordination number $1/Z$, and jump lengths seldom exceed the nearest-neighbor distance. The average squared net displacement of an ensemble of particles executing correlated random walks can be denoted as

$$\langle R^2_{\text{correlated}} \rangle = \sum_{i=1}^{n} \langle r_i^2 \rangle + 2 \sum_{i=1}^{n-1} \sum_{j=i+1}^{n} \langle r_i r_j \rangle, \tag{2.14}$$

where i denotes individual jumps and j considers follow-up jumps of the respective particle. In the case of an uncorrelated walking particle, all jumps are independent of each other. This jump sequence, as illustrated in Figure 3.1, is often called Markov sequence or memory free walk and implies that for every

r_i r_j consecutive jump another particle of the ensemble executes the exact same jump in the opposite direction. This yields a trimmed equation for the uncorrelated random walk

$$\langle R^2_{\text{uncorrelated}} \rangle = \sum_{i=1}^{n} \langle r_i^2 \rangle. \tag{2.15}$$

In both cases, jump vectors are limited to the coordination lattice Z and can only take a few definite values. Regarding the much simpler uncorrelated case, a reduction to the average number of jumps $\langle n \rangle$ and its squared jump length d can be performed.

$$\langle R^2_{\text{uncorrelated}} \rangle = \langle n \rangle d^2 \tag{2.16}$$

Furthermore, definition of the jump rate Γ and the mean residence time of an atom $\bar{\tau}$ gives a description for the diffusion coefficient in uncorrelated walk systems.

$$\Gamma \equiv \frac{\langle n \rangle}{Z t} \tag{2.17}$$

$$\bar{\tau} = \frac{1}{Z\Gamma} \tag{2.18}$$

$$D_{\text{uncorrelated}} = \frac{1}{6} d^2 Z\Gamma = \frac{d^2}{6\bar{\tau}} \tag{2.19}$$

Taking into account that the jump length d and the lattice parameter a exhibit lattice based relation to each other, the diffusion coefficient for primitive cubic

systems can also be described as

$$D_{\text{uncorrelated}} = a^2\Gamma. \tag{2.20}$$

Considering atomic diffusion mechanisms that are affected by memory effects, viz., correlated random walks, the successful jump of an atom ensues the movement of a, so-called, diffusion vehicle in opposite direction. Tracing the atom that diffuses through a defect bearing lattice reveals that such exchange processes are considered reversible and, thus, memory effects are considered detrimental. Nonetheless, fast ionic diffusion in solids is often defect-mediated, either by vacancies, vacancy pairs, self-interstitials or other diffusion vehicles. To relate both diffusion mechanisms to each other, the correlation factor was introduced in the early 50s [200, 201].

$$f = \lim_{n\to\infty} \frac{\langle R^2_{\text{correlated}}\rangle}{\langle R^2_{\text{uncorrelated}}\rangle} = 1 + 2 \lim_{n\to\infty} \frac{\sum_{i=1}^{n-1}\sum_{j=i+1}^{n}\langle r_i r_j\rangle}{\sum_{i=1}^{n}\langle r_i^2\rangle} \tag{2.21}$$

Here, the former term (+1) is associated to fully uncorrelated motions, whereas the latter term doubles the contribution of the correlated motions. Moreover, the latter term often yields negative values caused by higher probability of correlated jumps in reverse direction when compared to uncorrelated ones. Hence, the correlation factor f attains values between 0 and 1. Therefore, the correlation factor links the diffusivity of traced atoms to those that perform an

uncorrelated walk through the lattice

$$f \equiv \frac{D_{\text{correlated}}}{D_{\text{uncorrelated}}}. \tag{2.22}$$

The tracer diffusion coefficient D^{tr}, first introduced in (1.5) and meanwhile denoted as $D_{\text{correlated}}$, can also be defined as the f corrected diffusion coefficient for uncorrelated motion, also known as self-diffusion D^{sd}, previously defined in (2.19) and (2.20).

$$D^{\text{tr}} = \frac{1}{6} f d^2 Z \Gamma = f a^2 \Gamma = f D^{\text{sd}} \tag{2.23}$$

3.2.2 Temperature Dependence

Regardless of diffusion mechanism, mobile atoms have a finite probability to overcome an energy barrier and perform a successful jump to the next lattice site or interstitial site. This probability can be denoted as $e^{-\Delta H_{\text{m}}/\text{k}_\text{B} T}$, in which the change in migration enthalpy ΔH_{m} corresponds to the activation energy E_{a}. Changes in migration entropy ΔS_{m} solely result from the lattice vibrations generated by the atoms overcoming the E_{a}. Hence, the jump rate can be described as

$$\Gamma = \nu_0 e^{-\frac{\Delta S_{\text{m}}}{\text{k}_\text{B}}} e^{-\frac{\Delta H_{\text{m}}}{\text{k}_\text{B} T}}. \tag{2.24}$$

The attempt frequency, denoted as ν_0, ranges in the order of 10^{13} Hz and represents the vibration frequency of an atom around its equilibrium site in the target direction of its next jump. Figure 3.2 illustrates atoms hopping in a potential landscape.

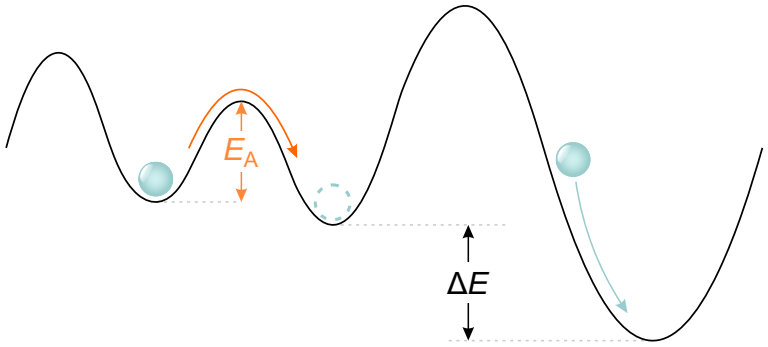

Figure 3.2: 1D Atoms jumping along energy landscape

3.3 Diffusion Mechanisms

Jumping processes of atoms in solid materials depend on a variety of factors. The most prominent and obvious among them are crystal structure, size and charge of the jumping atom and diffusion mediation by defects. The previously discussed correlation effects, *i.e.*, a series of jumps that occur in accordance with individual jump probabilities, play vital roles in some diffusion mechanisms, whereas others rely solely on uncorrelated motion.

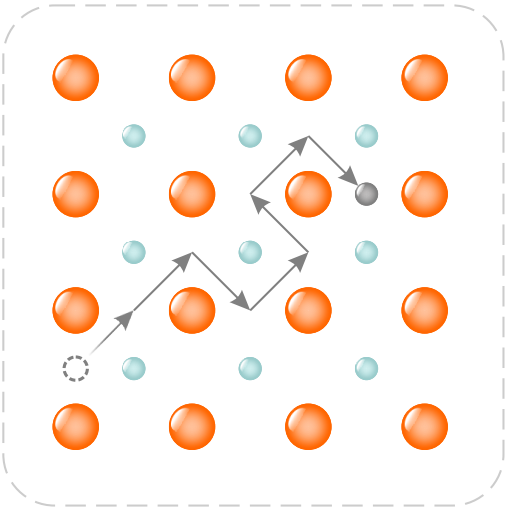

The *interstitial mechanism* describes the motion of a small foreign atom in a crystal structure in the absence of external influences. This mechanism solely relies on uncorrelated and unmediated motion of atoms on interstitial sites and interaction with the lattice only occurs by passing a saddle-point between two energetically favored interstitials. The event of a mobile species passing a saddle-point leads to lattice strain, but does not irreversibly affect the lattice. This diffusion mechanism is considered fairly fast.

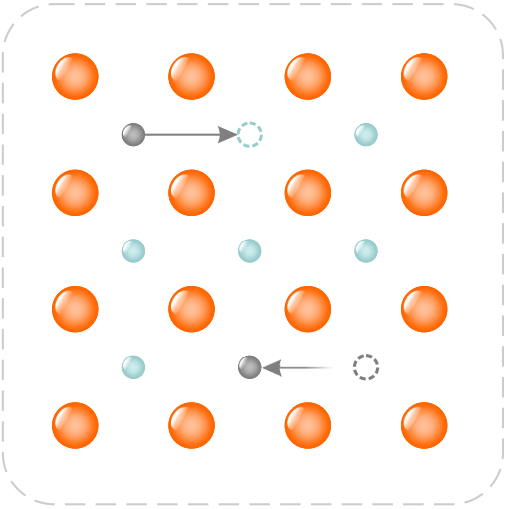

The *vacancy mechanism* is vital to describe diffusion of atoms through metals as well as ionic crystals. It establishes a connection between elevated temperatures and enhanced ion diffusion via inducing atomic defects in the crystal lattice. At high temperatures additional vacancies are generated and move along the lattice by undergoing exchange processes with tracer atoms. A series of exchanges between vacancy and tracer atom enables jumping throughout the crystal and results in diffusion. The divacancy mechanism is considered a special form of this procedure. At high temperatures two, sometimes even three, vacancies agglomerate due to binding energy and move as a pair. Even though this behavior was reported for fcc metals in particular, the monovacancy mechanism dominates the overall diffusion at temperatures 2/3 below the melting point.

The *interstitialcy mechanism* is also called the indirect interstitial mechanism and only occurs when the tracer atoms are comparable in size to lattice atoms. Here, tracer atoms exchange their positions on interstitial sites with those of lattice atoms, so that, lattice atoms finally reside on interstitial sites. These novel interstitials are referred to as self-interstitials and can also be generated by radiation, which leads to formation of vacancies on original lattice sites. Diffusion originating from such treatment is called radiation-induced diffusion and relies on vacancies formed during radiation. The collective nature of these interstitial exchange processes requires simultaneous motion of, at least, 2 atoms.

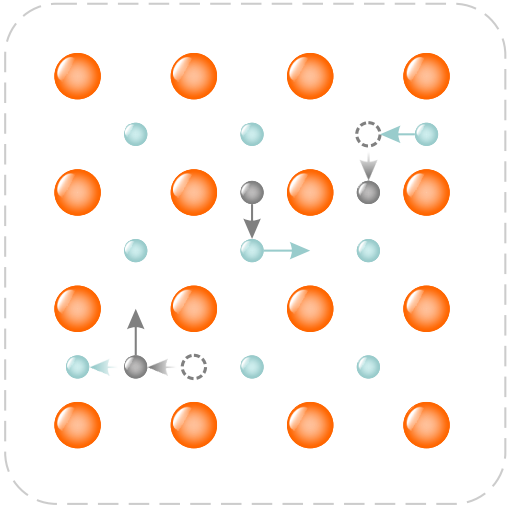

Collective Mechanisms. Direct exchange and the ring mechanism are regarded as further collective mechanisms. The former describes the simultaneous exchange of a tracer atom by a lattice atom while both reside on lattice sites. Considering closely packed crystal structures, this process entails enormous lattice distortions and requires high activation energy. The ring mechanism defines the simultaneous exchange of 3 or more atoms in the next neighborhood to each other. Compared to the single direct exchange, activation energies for such collective jump patterns are much lower and less lattice distortions occur.

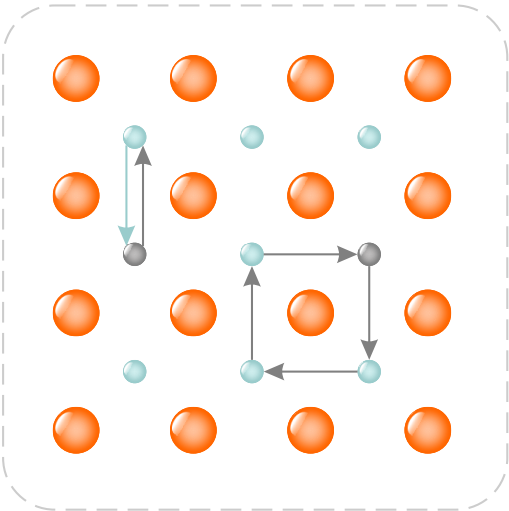

3.4 Origins of defects [202]

Mediated diffusion mechanisms rely on diffusion vehicles that are furthermore referred to as defects. These defects severely affect the diffusion of a mobile species through the crystal lattice and be classified according to their dimensionality.

3.4.1 Point defects (Zero-dimensional)

The simplest class of defects reposes on a missing atom on its original lattice site in a monatomic crystal structure. The absence of an atom at its original lattice site consigning a vacant site, as well as the occupation of an interstitial site, are considered two types of the same phenomenon. These defects can either occur naturally during crystal growth or, as mentioned earlier, are induced by radiation. At high temperatures, viz., during annealing of the crystals, the amount of intrinsic point defects is increased. Vacancies in crystals composed of differently charged ions exhibit Schottky defects and Frenkel defects. As illustrated in Figure 3.3 Schottky defects comprise anionic and cationic vacancies to maintain charge neutrality. Frenkel defects are generated by an ion moving from either the anion sublattice or the cation sublattice to an interstitial site and leaving behind a vacant lattice site. Another mechanism to generate

point defects is the substitution of ions by foreign atoms that is widely known as doping. Depending on the size of the foreign atom, doping entails either lattice expansion or compression. Introduction heterovalent dopants to the lattice system enhances vacancy formation to maintain charge neutrality of the overall system.

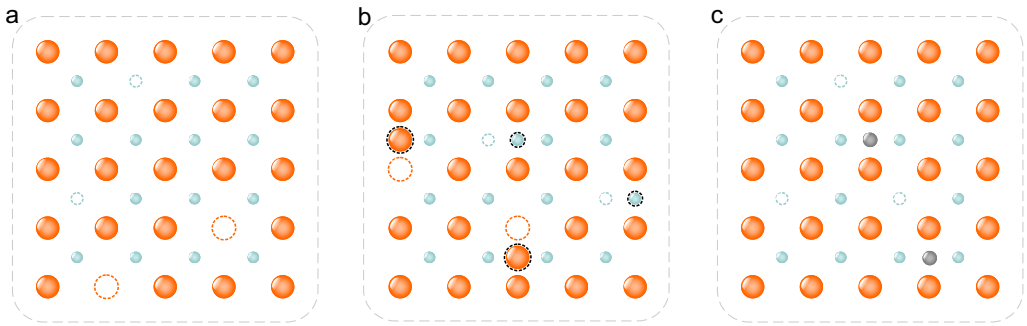

Figure 3.3: Illustration of point defect generation according to (a) Schottky, (b) Frenkel and (c) doping mechanism.

3.4.2 Dislocations (1-dimensional)

The class of linear defects is governed by dislocations that lead to an increase in entropy. The fact that dislocations are never in thermodynamic equilibrium with their surroundings renders them extrinsic defects. This class of defects is divided in subclasses that consist of edge dislocations, see Figure 3.4a, screw dislocations, as illustrated in Figure 3.4b, and mixed dislocations. Introduction of half planes in ionic crystals results in charged regions of positive or negative

nature, see red triangle in Figure 3.4a, that are able to affect the reactivity of the crystal when exposed at the surface.

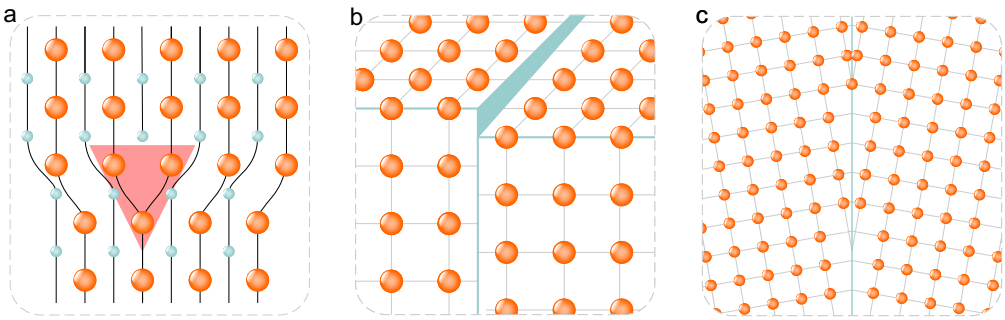

Figure 3.4: Non-zero-dimensional defects of the crystal lattice. (a) illustrates edge dislocations in ionic crystals exposing a charged tip. (b) represents a screw dislocation and (c) two mismatched lattices combined by a grain boundary.

3.4.3 Planar defects (2-dimensional)

Planar defects can be separated into external and internal surfaces; the latter are more prominent when topics like solid-state electrolytes are under investigation. The most popular case of internal surfaces is approached in grain boundaries. Here, the crystal lattices of at the edges of two grains build an interface, the so-called grain boundary. Besides the fact that a mismatch of crystal lattices at the interface of two grains is highly probable, impurity atoms tend to aggregate in said regions. Compared to the bulk, grain boundaries often exhibit diminished diffusivity, but tend to affect chemical reactivity and

other physicochemical properties in a beneficial way. Figure 3.4c illustrates a schematic of two mismatching grains at a grain boundary.

3.5 Experimental Probes for Ion Dynamics [197, 198, 203]

The most commonly used analysis technique for ionic conductivity is impedance spectroscopy. It is considered a powerful tool to probe dynamics in a broad frequency range and, therefore, elucidate long-ranged ion diffusion throughout the whole sample. To reveal localized jumps or dynamics on a shorter time scale, NMR is employed. This technique is very sensitive to hopping of a defined species and is often used to shed light on diffusion pathways in solid materials. Nowadays, a combination of both techniques is used to accurately characterize ion dynamics in a broad variety of materials.

3.5.1 Impedance Spectroscopy

Impedance spectroscopy, often denoted as electrochemical impedance spectroscopy (EIS) or complex electrical resistance, relies on a simple concept best

described by Ohm's Law

$$R = \frac{U}{I}. \tag{5.1}$$

Nonetheless, this relationship is only valid for ideal resistors which obey the rule at any circumstance. That said, the electrical resistance R of said circuit element is independent of alternating-current (AC) frequency and the phases of its current I and voltage U signals are not shifted towards each other, *i.e.*, in phase. When external voltage is applied to a completely homogeneous sample that fills the entire space between two current collectors, a uniform current passes through the sample and the resistance can be described by

$$R = \rho \frac{d}{A}. \tag{5.2}$$

Here, the resistance is composed of the dimensions of the sample, viz., the area A of the electrodes and the thickness of the sample d, and the characteristic electrical resistivity of the sample ρ. The latter is defined as the inverse of the conductivity σ. The conductivity reflects a materials ability to conduct charged species and is widely known as a variable to describe the performance of solid electrolytes.

The capacitor, or inductor, is another vital circuit element to describe impedance spectroscopy. In an ideal case it rejects any flow of current and stores

magnetic energy, generated by the applied electric field, at its electrodes that are separated by the dielectric sample. This system is expected to exhibit U and I responses that are completely out of phase. A characteristic variable for such elements is the capacitance, which can be denoted as

$$C = \frac{\epsilon_0 \epsilon A}{d}. \tag{5.3}$$

It introduces a ratio between the dielectric constant in vacuum ϵ_0 and the material related relative permittivity ϵ, *i.e.*, defined as a multiplier of ϵ_0 . However, actual impedance spectroscopy seldom deals with ideal resistors or capacitors. The majority of materials show influences of both systems and, on one hand, resist flow of the electrical current and, on the other hand, store electrical energy. This behavior is considered by definition of a resistive, real part, and a capacitive, imaginary part, of the impedance. Figure 3.5 illustrates the experimental setup that applies an AC voltage signal U of small amplitude U_A at a certain frequency f and detects the current response I that is of smaller amplitude I_A and shifted in phase ϕ.

$$U(t) = V_A \sin(2\pi f t) = U_A \sin(\omega t) \tag{5.4}$$

$$I(t) = I_A \sin(\omega t + \phi) \tag{5.5}$$

As executed in (5.4), the AC frequency can be converted to the radial frequency ω by multiplication with 2π. The measurement setup and the resulting interaction between variables is depicted in Figure 3.5. Furthermore, the aforementioned relation between voltage and current is only valid for linear or pseudo-linear systems. Formulating an expression for the complex impedance

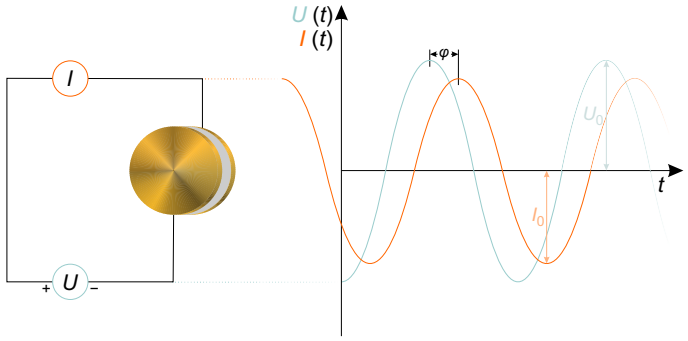

Figure 3.5: (a) impedance experiment setup depicting a sample with 2 gold current collectors attached to top and bottom surface, respectively. (b) plots the applied potential signal (aqua) and corresponding current signal (orange). Illustration based on figures published in Ref. [202, 203]

that comprises both terms, viz., that for input voltage and output current, yields an equation analog to Ohm's Law

$$Z^* = \frac{V(t)}{I(t)} = \frac{V_A \sin(\omega t)}{I_A \sin(\omega t + \phi)} = |Z| \frac{\sin(\omega t)}{\sin(\omega t + \phi)}. \tag{5.6}$$

Using Euler's relationship, (5.7), enables to distinguish between real and imaginary contributions to the complex impedance.

$$e^{i\omega t} = \cos(\omega t) + i \sin(\omega t) \tag{5.7}$$

Moreover, updated expressions for applied voltage and the corresponding current

$$V(t) = V_A \, \mathrm{e}^{i\omega t} \tag{5.8}$$

$$I(t) = I_A \, \mathrm{e}^{i(\omega t - \phi)} \tag{5.9}$$

are defined. Finally, the impedance can be denoted as complex number and the intermediates can be assigned to imaginary and real part of the impedance

$$Z^* = \frac{V}{I} = Z_A \, \mathrm{e}^{i\phi} = Z_A \, (\cos(\phi) + i \sin(\phi)) = Z' + i \, Z'', \tag{5.10}$$

whereas the phase angle ϕ is defined as the ratio of both components of the complex impedance

$$\phi = \arctan(\frac{Z''}{Z'}) \tag{5.11}$$

Plotting $-Z''$ against Z' illustrates the dependency on the radial frequency and yields a semi-circle. However, the absolute impedance $|Z|$ stretches from the center of the system of coordinates to the maximum of the semi-circle including the contiguous angle ϕ.

3.5.1.1 Immitance Functions

Measurement of the complex impedance Z^* enables determination of further sample properties that are closely connected to each other. These relations to the complex impedance are called immittance functions. In order to express them in a proper way, it is obligatory to determine the capacity of the empty measurement cell C_0. Regarding a simple parallel-plate capacitor geometry, in which a cylindrical pellet separates two current collectors, this variable can be described by

$$C_0 = \frac{\epsilon_0 A}{d}. \tag{5.12}$$

In this case, the capacity of the empty cell is solely based on cell geometry. Furthermore, introduction of the complex admittance, $Y = -Z^*$, and the complex capacitance, $C^* = Y/i\omega$, is vital to relate further immittance functions to the complex impedance.

Complex permittivity ϵ^* consists, analog to the complex impedance, of a real and an imaginary component. Dielectric analysis is employed to determine its magnitude that consists of contributions from dipole alignment ϵ' and ionic conduction ϵ''. Considering definitions for resistance R, (5.2), capacity for the empty cell C_0, (5.12), and capacitance C, (5.3), facilitates expression of the ϵ^*

in various ways.

$$\epsilon^* = \frac{Y}{i\omega C_0} = \epsilon' - i\epsilon'' \tag{5.13}$$

$$\epsilon' = \frac{Cd}{\epsilon_0 A} = \frac{C}{C_0} \tag{5.14}$$

$$\epsilon'' = \frac{d}{RA\omega\epsilon_0} = \frac{1}{\rho\omega\epsilon_0} = \frac{\sigma}{\omega\epsilon_0} \tag{5.15}$$

The last operation, viz., that yields an expression for the conductivity σ, is based on (5.2) and exploits the relationship between ρ and σ that was previously mentioned. Regarding the complex conductivity σ^*, definitions analog to those for the complex permittivity are obtained.

$$\sigma^* = \sigma' - i\sigma'' = \frac{1}{\rho^*} = \frac{Y}{C_0} = \frac{Yd}{\epsilon_0 A} \tag{5.16}$$

Both parameters, ϵ^* and σ^*, and their contributions to the overall impedance largely depend on the experimental setup. This includes material temperature, AC frequency and the magnitude of the sinusoidal voltage signal. The complex modulus represents another way to describe properties of a material with data gathered from dielectric analysis

$$M^* = M' - iM'' = i\omega C_0 Z = \frac{1}{\epsilon^*}. \tag{5.17}$$

Analysis of Experimentally Obtained Impedance Data [204–207] Considering the field of application of materials investigated during this work, analysis

and illustration of the acquired data as conductivity isotherms and in complex plane plots is of great interest.

For a measurement performed at constant temperature such isotherms are obtained by plotting the real part of the conductivity σ' against the frequency ν. Figure 3.6 depicts a classic form obtained for monocrystalline materials that is best illustrated by logarithmic representation of both variables. In general, a decrease in temperature results in shifting of the isotherms towards lower frequencies. Thus, at appropriately high temperatures and at reasonably low frequencies polarization effects at the current collectors can be observed. In such an event, these effects are referred to as electrode polarization, and arise from accumulation of ionic species at the electrode surfaces and, consequently, limited ionic conductivity. At intermediate frequencies to high frequencies, frequency independent conductivity plateaus σ_{DC} are obtained. These areas correspond to long-ranged ionic motion inside the material and can be, depending on the frequency, assigned to bulk or grain boundary diffusion processes. Provided that grain boundary diffusion in single crystals is negligible, the obtained plateau in Figure 3.6 is fully assigned to bulk conductivity. Analog to the temperature dependence of the diffusion in solids,

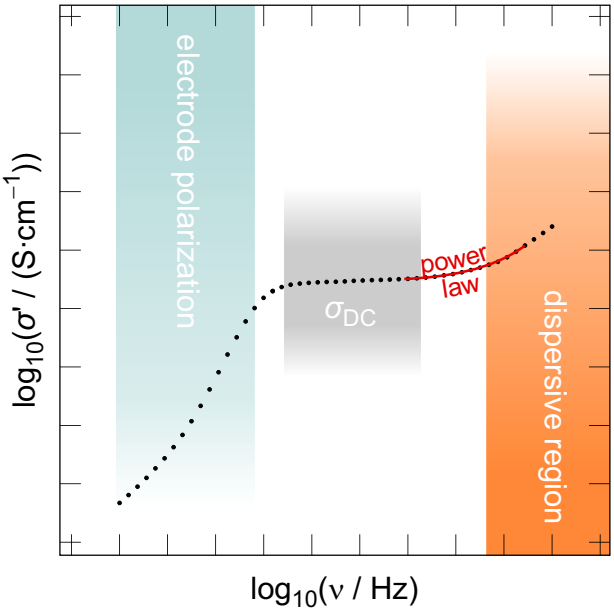

Figure 3.6: Conductivity isotherm of a single crystalline material. Specific regions are indicated by arrows or marked by color.

σ_{DC} enables calculation of the activation energy for long-ranged ion diffusion

$$\sigma_{DC} T \propto e^{-\frac{E_A^{DC}}{k_B T}}. \tag{5.18}$$

Moreover, σ_{DC} can be used to describe a coefficient that corresponds to the ionic conductivity D^{σ}. This coefficient is not described by Fick's First Law and, even though it exhibits units similar to a diffusion coefficient, cannot be denoted as a diffusion coefficient. Its definition is derived from the the Nernst-Einstein equation, and is given by

$$D^{\sigma} = \frac{k_B T \sigma_{DC}}{N q^2}. \tag{5.19}$$

Here, N is considered the charge carrier density and q specifies the charge of the carrier ions. Furthermore, D^{σ} is linked to the tracer diffusion coefficient D^{tr} via the Haven ratio [208].

$$H_{\mathrm{R}} = \frac{D^{\mathrm{tr}}}{D^{\sigma}} \tag{5.20}$$

In the case of uncorrelated random walks of a single species a connection to the correlation factor f is established $H_{\mathrm{R}} = f = 1$. Thus, both diffusion coefficients, viz., tracer and self diffusion, and the conductivity coefficient D^{σ} are equal. In case of divacancies the Haven ratio exhibits values > 1, whereas correlated motion and contributions of electrical conductivity lead to values < 1.

Leaving the DC-region of the conductivity isotherm an upcoming increase in σ introduces the dispersive region. Since σ_{DC} can be regarded as the maximum of the current response during impedance measurements, the dispersive region can be referred to as dielectric loss. In 1977 Jonscher formulated a relation to describe this transition

$$\sigma(\omega) = \sigma_0 + \epsilon_0 \omega \chi''(\omega), \tag{5.21}$$

and suggests proportionality between $\sigma(\omega)$ and ω^n. This is considered the Jonscher power law, in which $\omega = 2\pi\nu$, and ν denotes the frequency. Values of n range between 0 and 1 and can be used to estimate the dimensionality of the

underlying diffusion mechanism [209]. Here, values below 0.4 point towards 1D diffusion, $0.45 \leqslant n \leqslant 0.6$ describe 2D motion and n-values exceeding 0.66 are characteristic for 3-dimensional ion transport. In addition, temperature dependence of the real conductivity decreases with increasing temperature and exhibits a linear region, for which $\sigma' \propto \nu$ holds, called nearly constant loss (NCL). Taking this into account, yields an equation that describes the dispersive region and adds a linear term to include contributions from NCL, which is assumed to take place at very high frequencies.

$$\sigma(\nu) = \sigma_0 \left[1 + \left(\frac{\nu}{\nu_0} \right)^n \right] + Af \tag{5.22}$$

Figure 3.7 plots $-Z''$ against Z' yielding complex plane plot, which is often referred to as Nyquist plot or Cole diagram. As mentioned earlier, the complex impedance depends on the radial frequency and, therefore, complex plane plots are characterized by illustration of one or more semi-circles. Here, each of the semi-circles can be assigned to a particular phenomenon that occurs at certain conditions. A noteworthy detail is the descending frequency from the left side to the right side. To describe one of the depicted semi-circles, a parallel circuit comprising an ohmic resistance R and a capacitance C is regarded

$$Z^* = \frac{R}{1 + i\omega CR}, \tag{5.23}$$

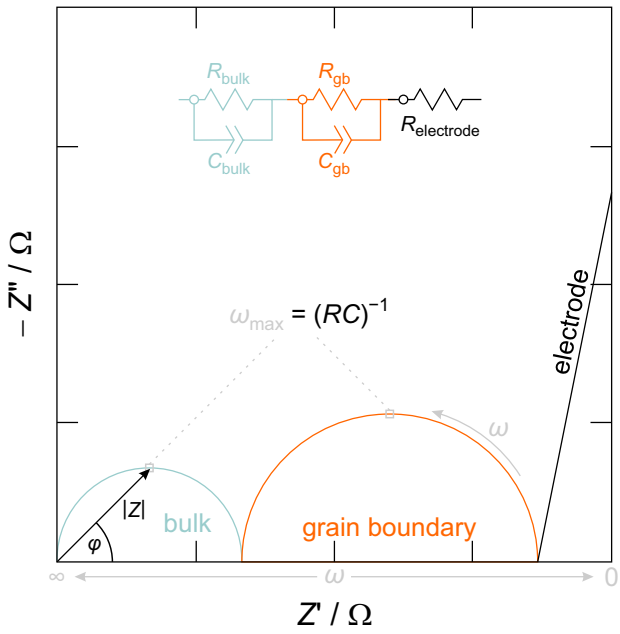

Figure 3.7: Illustration of a complex plane plot obtained from a ceramic sample. The equivalent circuit diagram is depicted in the top section of the graph and characteristic features are indicated either by text, color or arrows. This plot is based on Ref. [197].

with the angular frequency given as ω. This equation differentiates between three extreme cases, viz., the two intersections with the x-axis and the maximum of the semi-circle. Therefore, left minimum can be referred to as $\omega \rightarrow \infty$, the right one as $\omega = 0$ and the maximum of the semi-circle is defined by $\omega = (RC)^{-1}$. The latter are used to calculate characteristic capacitance values that can, futhermore, be ascribed to a specific phenomenon in the sample [210]. In general, bulk responses lead to much lower capacitances than any other phenomenon.

3.5.2 Solid-State Nuclear Magnetic Resonance [198, 211]

Nuclear Magnetic Resonance (NMR) is a nondestructive and potent tool to study diffusion properties of broad variety of materials. Its working principle relies on the sensitivity to localized field variations that are introduced by the interaction of the nuclear magnetic moment with the external magnetic field. Since the first reports on the impact of ion motion inside materials on the field variations measured by NMR [212], the influence of this technique on studies concerning ion dynamics grew continuously. In stark contrast to impedance spectroscopy, which measures a macroscopic electrical response caused by diffusing ions, NMR senses ion dynamics on a microscopic scale, viz., by resolving short-ranged and medium-ranged ion hopping through the crystal lattice. Fundamentals of NMR Atomic nuclei are often illustrated as spherical objects that exhibit a rotational axis and, for the sake of simplicity, the following expressions will stick to that theory. These nuclei carry an intrinsic angular momentum $\boldsymbol{P}$ that, according to quantum mechanics, can be quantisized to

$$\boldsymbol{P} = \sqrt{I(I+1)}\,\hbar. \tag{5.24}$$

The Planck's constant h is taken into account by $\hbar = 2\pi h$ and I is often referred to as nuclear spin and represents the angular momentum quantum number.

Usually, I is described by the values 0, $^1/_2$, 1, $^3/_2$, etc.. Thus, atoms that feature a nuclear spin equal to 0 are considered NMR inactive. To establish a connection between $\boldsymbol{P}$ and the magnetic moment $\boldsymbol{\mu}$, a constant that attains unique values for each nuclide, viz., the gyromagnetic ratio γ, is introduced

$$\boldsymbol{\mu} = \gamma \boldsymbol{P}. \tag{5.25}$$

Due to the role as proportionality factor, its magnitude severely affects the sensitivity of NMR towards certain nuclides. Nuclides that exhibit higher γ values are easier to detect than those showing low values.

Application of an external magnetic field $\boldsymbol{B}_0$ that is of static origin, leads to the orientation of $\boldsymbol{P}$ point towards the direction of said field. A part of the angular moment, namely, the part P_z facing z-direction, is aligned with the external field and best described by an integral or half-integral multiple of $\hbar$

$$P_z = m\hbar. \tag{5.26}$$

Directional quantization occurs and the orientation of the magnetic moment, as well as the angular frequency, is restricted to $(2I+1)$ different directions. Furthermore, the same quantity of values also defines the directional quantum number m. In the case of ^{7}Li or ^{23}Na nuclei, both exhibit nuclear spins of $^3/_2$, this calculation yields 4 m-values $(-^3/_2, -^1/_2, +^1/_2, +^3/_2)$. A combination of (5.25)

and (5.26) defines the magnetic moment along the z-axis and, therefore, the external magnetic field $\boldsymbol{B}_0$

$$\mu_z = m\gamma\hbar \tag{5.27}$$

Analog to a spinning top, the external magnetic field exerts a torque on the magnetic moment that results in precession of the nuclear dipoles. The frequency of the precession, the so-called Larmor frequency ν_{L}, is best described by its proportionality to the magnetic flux density B_0.

$$\nu_{\mathrm{L}} = \left|\frac{\gamma}{2\pi}\right| B_0 \tag{5.28}$$

Correspondingly, the magnetic moment in z-direction μ_z experiences splitting of its energy in $(2I+1)$ energy states the, so-called, Zeeman levels.

$$E = -\mu_z B_0 = -m\gamma\hbar B_0 \tag{5.29}$$

These energy values are, in the same manner as the Larmor frequency, proportional to the magnetic flux density. Figure 3.8 highlights the relation between the splitting of the angular momentum in z-direction and the creation of Zeeman energy levels. Here, the difference ΔE of two energy levels that only differ in sign, increases proportional to the magnetic flux density B_0. At thermal equilibrium, the entirety of spins is unequally distributed among the two possible orientations. This phenomenon is best described by Boltzmann statistics

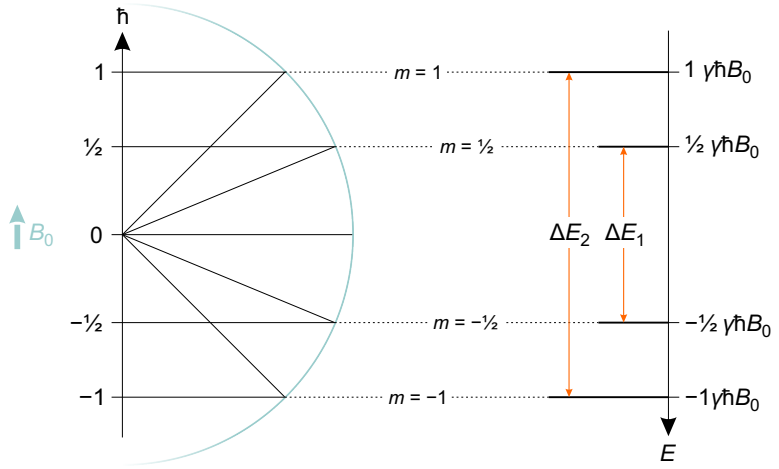

Figure 3.8: Energy splitting of a $I = {}^3/_2$ nucleus into its Zeeman levels. Dotted lines establish the connection to directional quantization of the angular momentum P_z. This representation merges several figures from [211]

that relate the occupation of the energy levels, referring to N^+ as the lower energy level and N^- as the upper energy level, to one another. Furthermore, the temperature dependence of the occupancy ratio is described as

$$\frac{N^-}{N^+} = \mathrm{e}^{-\frac{\Delta E}{\mathrm{k_B} T}} \approx 1 - \frac{\Delta E}{\mathrm{k_B} T}. \tag{5.30}$$

At reasonably high absolute temperature T, both energy levels are equally occupied. Here, the temperature-dependent term yields such low values that the ratio of the two occupancy numbers almost equals 1. Any other case is described by $N^-/N^+ < 1$ and, therefore, results in unequally occupied energy levels. NMR is highly sensitive to these differences that occur to extents in the parts per million range. As a result of the inability to probe isolated spins, an

amount of spins that experiences the same magnetic field strength is defined as spin ensemble. Regarding such ensembles, the magnetic moments of the particular spins can be added to define a net magnetization vector M_0. In a thermal equilibrium state, said vector M_0 solely consists of contributions in z-direction M_z and is, therefore, aligned with the external field $\boldsymbol{B}_0$. Contributions in x-direction, as well as y-direction, are averaged by the rotation of the system. To perform relaxation measurements on the aforementioned system, a radio frequency (rf) pulse is applied to disrupt the thermal equilibrium state. As a consequence, the net magnetization vector is deflected from its original z-direction. This operation results in a pseudo-equilibrium that characterized by

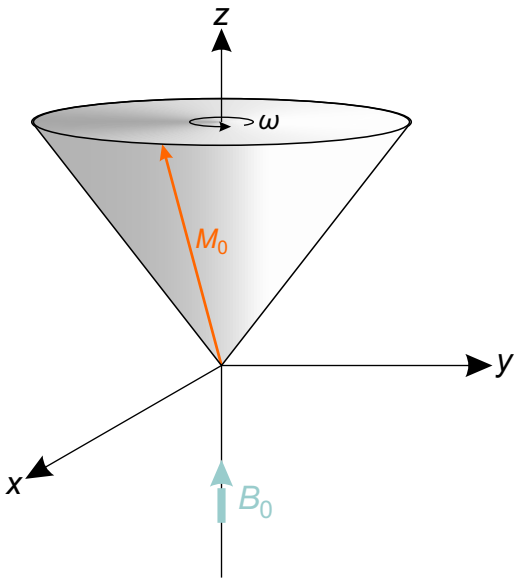

Figure 3.9: Precession of the net magnetization vector M_0 in a magnetic field $\boldsymbol{B}_0$. This schematic is based on an illustration in [211].

equal occupation of both energy levels. The application of the pulse is limited to a certain, usually very short, amount of time and is followed by relaxation of the excited system to its initial state. Two of those relaxation mechanisms, viz., spin-lattice and spin-spin, are of utmost importance to shed light on ion dynamics.

The spin-lattice relaxation time T_1, also known as longitudinal relaxation, defines a characteristic time that describes the materials ability to pass the energy, *i.e.*, formerly absorbed from the rf-pulse, to its crystal lattice without radiation. This process is best described by the first order expression

$$\frac{dM_z}{dt} = \frac{M_0 - M_z}{T_1}. \tag{5.31}$$

Spin-lattice relaxation performed in the laboratory frame of reference is widely used to study strictly localized ionic motion at frequencies in the MHz range. Weaker external magnetic fields, viz., in the kHz range, are applied to observe hopping processes on a larger time scale. These, so-called spin-lock, experiments yield spin-lattice relaxations times in the rotating frame of reference $T_{1\rho}$.

$$\frac{dM_{y'}}{dt} = \frac{M_\rho}{T_{1\rho}} \tag{5.32}$$

To process and analyze the resulting characteristic times T_1 and $T_{1\rho}$ Arrhenius representation is considered the state of the art. Kuhn et al. published

a comprehensive work that accurately describes the underlying principles of the phenomena depicted in Figure 3.10 [213]. As already mentioned, interpretation of relaxometry data was substantially influenced by the pioneer work of Bloembergen, Purcell and Pound (BPP)[212]. In the ideal case, Arrhenius

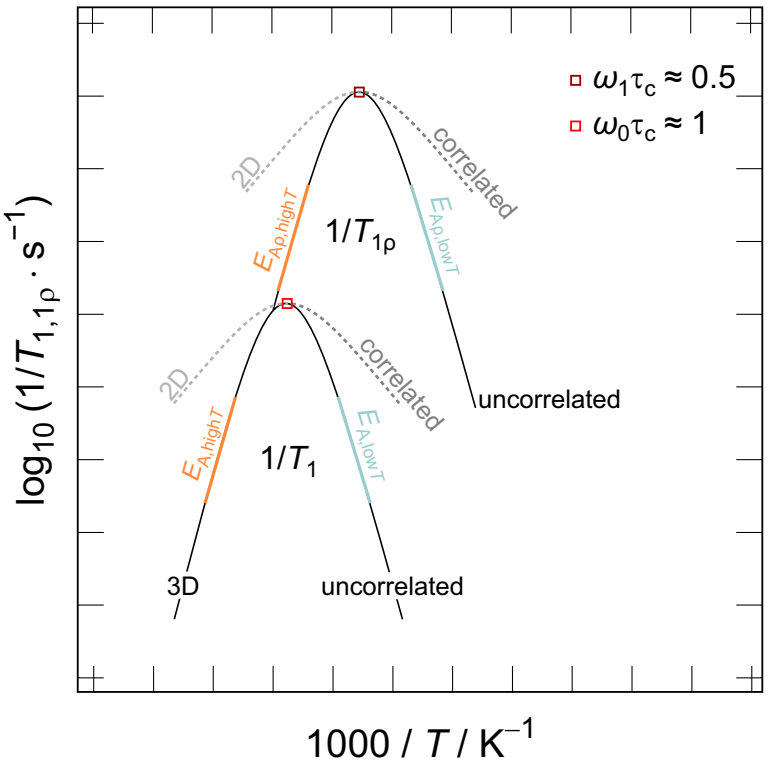

Figure 3.10: Arrhenius plot of spin-lattice relaxation data acquired in the laboratory frame of reference and rotating frame of reference, respecively. This illustration is based on a figure from Ref. [213].

representation of relaxometry data, regardless of the frame of reference, depicts a rate peak. Its maximum provides vital information on the jump rate τ that is within a factor of 2 identical to the correlation rate τ_c. Furthermore,

the maximum indicates a certain temperature at which the frame of reference dependent relation, which is denoted as $\omega_0\tau_c \approx 1$ for T_1 and $\omega_1\tau_c \approx 0.5$ for $T_{1\rho}$, holds and in which $\omega = 2\pi\nu_L$. The BPP model is based on the Fourier transformation of the motional correlation function $G(t) = \exp(-(|t|/\tau_c))$, *i.e.*, in its single exponential form valid for 3D uncorrelated motion, and results in a Lorentzian-shaped spectral density function

$$J(\omega) = \frac{2\tau_c}{1 + (\omega\tau_c)^2}, \tag{5.33}$$

that is proportional to the rates acquired from spin-lattice relaxation measurements. Considering the presence of defects or Coulombic interactions of the spins, the correlation function deviates from its single exponential form and is described by $G(t) = \exp(-(|t|/\tau_c)^\alpha)$. Here, α is a stretching exponent with values ranging between 0 and 1. Fourier transformation yields the corresponding spectral density function

$$J(\omega) = \frac{2\tau_c}{1 + (\omega\tau_c)^{1+\alpha}}. \tag{5.34}$$

Literature often introduces the correlation factor β, which is defined as $\beta = 1 + \alpha$, to describe three dimensional correlated motion. In Figure 3.10, BPP modeling of the rate peak discloses details on dimensionality of the jump processes, as well as correlation of the motion. The former are revealed by the

slope of the high-temperature flank ($\omega_0\tau_c \ll 1$) and ($\omega_1\tau_c \ll 0.5$), respectively. Regarding the slope of the low-temperature flank, defined as ($\omega_0\tau_c \gg 1$) or ($\omega_1\tau_c \gg 0.5$), enables differentiation between correlated and uncorrelated ion hopping. Considering an Arrhenius relationship, the previously discussed slopes are highly useful to determine activation energies for the previously discussed ion dynamics.

CHAPTER 4

RESULTS

4.1 Ion Dynamics in Aliovalently Substituted Garnet-Type $Li_7La_3Zr_2O_{12}$ Single Crystals

These two manuscripts, of which one is already under review (supporting information can be found in the Appendix section), focus on elementary Li hopping processes and elucidation of diffusion pathways in supervalently stabilized cubic $Li_7La_3Zr_2O_{12}$ (LLZO) single crystals. LLZO, that usually crystallizes in its tetragonal polymorph, can be stabilized in its cubic form by substitution of Li^+ and Zr^{4+}, respectively. The most popular option to yield the cubic structure is to exchange 3 Li^+ ion by 1 Al^{+3} or Ga^{3+} ion. This exchange is accompanied by

a steep increase in overall conductivity of at least 2 orders of magnitude. The overall conductivity of polycrystalline samples, however, is always quantified as a combination of bulk and grain boundary contributions. Additionally, the effect of inhomogeneous polycrystalline samples on the overall conductivity was recently discussed in literature. Here, Czochralski grown single crystals were probed to assure determination of bulk properties in a homogeneous sample. To resolve ion dynamics in a broad frequency range, impedance spectroscopy results were combined with those obtained from time-dependent ^{7}Li spin-lattice relaxation NMR. The latter is a powerful technique to sense short-ranged to medium ranged ionic motions. Checked against computational simulation, the acquired data provide even deeper insights in diffusion and enable the assignment ion diffusion paths.

The first article exposes the influence of Al^{3+} substitution, which resides on 24*d* lattices sites, on ionic motion. The investigated monocrystalline $Li_{6.46}Al_{0.15}La_3Zr_{1.95}O_{11.86}$ garnet exhibits ionic conductivities of 8.3×10^{-5} S cm^{-1} at 20 °C. Regarding long-ranged bulk dynamics, the material yields an activation energy of 0.36 eV and is, therefore, in good agreement with medium-ranged ion dynamics (0.35 eV to 0.38 eV) as sensed by ^{7}Li spin-lattice relaxation NMR in the rotating frame of reference ($1/T_{1\rho}$). Furthermore, strictly localized

ionic motion between 24*d* and 96*h* sites, as seen in the laboratory frame of reference ($1/T_1$), is characterized by considerably lower activation energies ranging from 0.18 eV to 0.2 eV. In agreement with computational studies, we can assume that blocking of Li^+ diffusion in close proximity to the Al^{3+} ions, viz., residing on 24*d* lattice sites, open the possibility of bypassing jumps between neighboring $96h - 96h'$ sites.

The second article, a manuscript, focusses on ionic motions in the acentric cubic (space group $I\bar{4}3d$, No. 220) polymorph $Ga_{0.2}Li_{6.54}La_{2.92}Zr_2O_{11.95}$. This single-crystalline material features a much higher room-temperature conductivity, viz., 1.1 mS cm^{-1}, than its Al-stabilized analog. Activation energies for long-ranged diffusion match with data obtained from the electric modulus, both methods yield 0.3 eV. Medium-ranged ion dynamics ($1/T_{1\rho}$) are governed by two jump processes that both exhibit rate maxima well below ambient temperature and, therefore, point towards very fast ion dynamics. This work in progress aims at assignment of said jump processes to Li^+ hopping between defined lattice sites and is, therefore, largely dependent on dynamics simulations.

Ion Dynamics in Al-Stabilized $Li_7La_3Zr_2O_{12}$ Single Crystals – Macroscopic Transport and the Elementary Steps of Ion Hopping

P. Posch[a*], S. Lunghammer[a], S. Berendts[b], S. Ganschow[c], G. J. Redhammer[d], A. Wilkening[a], M. Lerch[b], B. Gadermaier[a], D. Rettenwander[a], and H. M. R. Wilkening[a‡]

[a]Institute for Chemistry and Technology of Materials, Christian Doppler Laboratory for Lithium Batteries, Graz University of Technology (NAWI Graz), Graz, Austria

[b] Department of Chemistry, Berlin University of Technology, Berlin, Germany

[c] Leibniz-Institut für Kristallzüchtung (IKZ), Berlin, Germany

[d] Department of Chemistry and Physics of Materials, University of Salzburg, Salzburg, Austria

[*]p.posch@tugraz.at

[‡]see also for correspondence: wilkening@tugraz.at

Abstract

$Li_7La_3Zr_2O_{12}$ (LLZO) garnet-type ceramics are considered as very promising candidates for solid electrolytes and have been extensively studied in the past few years. Several studies report on an increase in ionic conductivity by doping with ions, such as Al^{3+} and Ga^{3+}, to stabilize the cubic modification of LLZO. Unfortunately, so far ion dynamics have mainly been studied using powdered samples. Such studies may suffer from chemical heterogeneities concerning Al distribution. Here, we took advantage of Al-stabilized LLZO single crystals to throw light on the elementary steps of ion hopping. We used ^{7}Li nuclear magnetic resonance (NMR) spin-lattice relaxation measurements and conductivity spectroscopy to probe dynamic parameters from both a microscopic and macroscopic point of view. At 293 K the total conductivity turned out to be 0.082 mS cm^{-1}, which is remarkably good for LLZO exhibiting an Al-content of only 0.37 wt%. Most importantly, ^{7}Li NMR spin-lock transients revealed two overlapping diffusion-induced processes. Overall, activation energies from spin-lock NMR excellently agree with that from conductivity measurements; both techniques yield values around 0.36 eV. The corresponding diffusion coefficients deduced from NMR and conductivity measurements almost coincide. The magnetic spin fluctuations sensed by NMR provide an in-depth look at the elementary jump processes, which can barely be revealed by macroscopic impedance spectroscopy. In particular, we were able to precisely measure the local hopping barrier (0.20 eV) characterizing forward-backward jumps between the sites 24*d* and 96*h*.

Keywords: garnets; single crystal; NMR; dynamics; conductivity

I. Introduction

By signing the Kyoto Protocol in 1999, 84 industrial nations agreed on subsequent reduction of greenhouse gas emissions [1]. Achieving these goals is accompanied by a drastic decrease of our annual fossil fuel consumption. One possibility to reduce such emissions is to store energy that is generated from renewable resources [2]. In recent decades, electrochemical energy storage devices have proven to be suitable candidates for this purpose [3]. It is envisaged that such devices will find applications in static power plants as well as in automotive industry and the aviation sector. Li-ion batteries (LiBs) belong to the so far leading products used in our daily life [4]. Improvements are, however, needed if we want to meet the current demands formulated by automotive industry [5, 6]. Commercial LiBs, independent of their size and energy density, may suffer from stability issues caused by flammable liquids used as electrolytes [7]. Solid electrolytes [8] may significantly improve both safety and lifespan of batteries using Li^+ [9] or even Na^+ [10] as ionic charge carriers.

To realize the next generation of Li batteries with ceramic electrolytes, battery research faces the request to explore electrochemically stable and non-flammable ceramics that feature very high Li-ion conductivities [9–11]. Replacing aprotic liquid electrolytes will, however, only be successful if we have economically friendly ceramics at hand that offer ion conductivities comparable to that of liquids [12, 13]. Combined with low activation energies for ionic transport such systems can be operated over a large temperature range. Most importantly, they will withstand much higher temperatures than conventional batteries. Clearly, the most suitable candidates should also exhibit negligible electronic conductivity, high chemical stability and low area specific resistances at the electrolyte | electrode interfaces [14]. From the broad variety of different materials, garnet-type [15, 16] electrolytes are regarded as the most promising choice for all-solid state LiB.

Since the first report of Murugan *et al.* on $Li_7La_3Zr_2O_{12}$ (LLZO) garnet, which exhibited a room-temperature ionic conductivity in the order of 10^{-3} to $10^{-4}\,S\,cm^{-1}$, the interest in garnet-type materials with cubic symmetry grew rapidly [12]. The ionic conductivity of the cubic form of LLZO is by two orders of magnitude higher than that of the tetragonal polymorph (space group $I4_1/acd$) [17–19]. Stabilization of cubic LLZO is possible by appropriate doping [20]. $Li_7La_3Zr_2O_{12}$ first prepared by Murugan *et al.* was stabilized by Al^{3+} doping [12]. Depending on the dopants, such as Al^{3+} or Ga^{3+}, cubic LLZO crystallizes with different symmetries (space groups $Ia\bar{3}d$ and $I\bar{4}3d$) [21]. Meanwhile a huge number of studies can be found in literature that deal with the question which dopants are best suited to achieve a high conductivity of the cubic form [16, 19, 21–23]. These studies also investigate the possibilities to substitute La^{3+} and Zr^{2+} by alio- and isovalent cations [20].

Aliovalent doping with Al^{3+}, *i.e.*, substitution of $3\,Li^+$ ions by one Al^{3+} cation, became the most popular method to stabilize cubic-LLZO and to create Li-ion vacancies [24]. Together with Li^+ the aluminium ions occupy the tetrahedral 24*d* sites in an irregular manner. As a consequence, cation and bond disorder is produced affecting the site preference of the Li ions. This effect is assumed to significantly boost ionic conductivity [25].

In a recent comparison, Wachter-Welzl *et al.* address the interaction between dopant quantity and synthesis conditions [26]. In numerous reports, aluminium contents range from 0.17 to 0.35 Al^{3+} ions per formula unit (pfu). Nonetheless, conductivities peak around 0.2 pfu [26]. Furthermore, co-doping with Ta further enhances Li^+ ion dynamics by shifting the Al^{3+} ions to 96*h* sites resulting in a reduction of Li^+ diffusion pathways blocked by the immobile Al^{3+} ions [27]. Quite recently, we reported on a single long-range Li^+ ion transport process through the lattice of Al-free single crystalline $Li_6La_3ZrTaO_{12}$ [28].

While doping is known to severely affect the Li ion transport behaviour, the preparation conditions also seem to have an enormous im-

pact on the properties of the final product. In 2014, an overview to which extent the properties of LLZO may vary has been presented by Pinzaru *et al.* [20]. Synthesis routes like field assisted sintering technique (FAST), hot isostatic pressing or sol-gel preparation lead to quite different dynamic properties of the resulting material [23, 29, 30]. This can mainly be attributed to the density of the material affecting grain boundary ionic conductivities. As shown by Kim *et al.*, lower sample density leads to increased grain boundary resistance, and thus, lowers the overall conductivity of the material [31][31].

To understand the elementary steps of ion hopping in Al-stabilized LLZO independent of the preparation and post-preparation conditions we take advantage of single-crystalline, Czochralski-grown $Li_7La_3Zr_2O_{12}$. We used contactless ^{7}Li nuclear-magnetic resonance (NMR) spectroscopy [18, 28, 32–36] to probe the electric and magnetic field fluctuations the Li spins are exposed to during self-diffusion. The resulting diffusion-induced ^{7}Li NMR spin-lattice relaxation rates, if studied as a function of temperature, entail information on both local hopping processes as well as long-range ion transport [35, 36]. Throwing light on the underlying diffusion mechanisms that govern fast translational Li ion dynamics in Al-stabilized LLZO is expected to assist in the design of improved LLZO ceramics [20]. We compare our NMR results with results from alternating current (AC) conductivity measurements [37], which are widely used to characterize long-range ion motions. This comparison helps us to describe the motional correlation functions controlling the fast cation exchange processes in LLZO-type materials.

II. Methods

Sample Preparation and Characterization

The Al-stabilized LLZO single-crystal was grown directly from the melt using the Czochralski method. The raw materials, Li_2CO_3 (5N, Alfa Aesar), La_2O_3 (4N5, Treibacher Industrie AG), Al_2O_3 (4N, HAM) and ZrO_2 (4N, Johnson-Matthey Chemicals), were dried and afterwards mixed in a stoichiometric ratio. The powder was pressed isostatically at 2 kbar and calcined at 680 °C for 70 h. The so-obtained body was melted in an inductively heated iridium crucible. On top of the crucible an active afterheater closed by a ring disc was placed; this arrangement was embedded in ceramic alumina insulation. The process chamber was rinsed with 5N nitrogen at a rate of 21 l/h. An iridium wire served as crystallization seed that was pulled with 1.5 mm h^{-1} and rotated at 10 rpm. Inductively coupled plasma mass spectrometry (ICP-MS) showed that the aluminium concentration in our single crystal was $[Al]_S$ = 0.37 wt.-%. Comparing this value with the aluminium amount in the initial melt, $[Al]_L$ = 0.92 wt.-% gives a first estimate for the aluminium distribution coefficient during the crystallization of the garnet phase from the melt: $k_{Al} = [Al]_S / [Al]_L = 0.4$. The concentration of 0.37 wt.-% yields a chemical composition of the crystal of $Li_{6.46}Al_{0.15}La_3Zr_{1.95}O_{11.86}$, which refers to 3 La^{3+} ions per formula unit. The single crystals (space group symmetry $Ia\bar{3}d$) were characterized by X-ray diffraction(see also Fig. S1); information on crystal data, structure refinement, atomic coordinates, bond lengths and occupation factors are shown in the Supporting Information (SI) section (Tables S1 to S3). All the crystals investigated turned out to be single crystalline in nature and of good quality with sharp Bragg reflections. We found no evidence for any kinds of intergrowth or for diffuse streaks indicative for chemical inhomogeneity.

One of the slightly yellow crystals (EK_Al3, see Tables S1 to S3, SI) was cut into smaller pieces of approximately 5 mm × 5 mm × 1 mm. These pieces were polished with a Struers LaboPol-25 device equipped with 300, 800, 1200, 2400 grit SiC abrasive paper at a speed of 300 rpm. Two gold electrodes, with a thickness of approximately 100 nm, were applied on top and bottom of one sample by using a Leica sputter device. For static ^{7}Li NMR measure-

ments another sample (EK_Al3, see SI) with dimensions of 1 mm × 1 mm × 8 mm was polished and then fused in a Norell SEPR250S quartz tube with a length of approximately 1.5 cm.

AC Conductivity Measurements

A Novocontrol Concept 80 broadband dielectric spectrometer was used to investigate impedance properties at frequencies ranging from 10 MHz to 0.1 Hz. In order to reveal temperature dependent properties, the device is equipped with a QUATRO cryosystem (Novocontrol) to vary the temperature. Here, we recorded conductivity isotherms in a temperature range from 173 K to 453 K. The cryostat works by vaporization of liquid N_2 that is stored in a dewar vessel. A heating element is used to create a constant gas flow of N_2. This setup allows us to control the temperature inside the sample cell with an accuracy of ± 0.1 K.

NMR Measurements

^{7}Li spin-lattice relaxation NMR measurements were performed using an Avance III spectrometer connected to an Ultrashield 500-MHz widebore magnet with a nominal field of 11 T. Additionally, we used an Avance III spectrometer in combination with an Ultrashield 300-MHz magnet (7 T). The magnetic fields correspond to ^{7}Li Larmor frequencies of $\omega_0/2\pi = 194$ MHz and 116 MHz, respectively. A ceramic probe head, constructed to withstand high temperatures, was used for all experiments. Depending on temperature, the $\pi/2$ pulse length varied from 2.4 μs to 3.4 μs maintaining a constant power output of 200 W throughout the measurements. The well-known saturation recovery sequence was used to acquire spin-lattice relaxation rates $1/T_1$. We also performed so-called spin-lock spin-lattice relaxation NMR measurements to study the temperature dependence of $1/T_{1\rho}$. For this purpose we took advantage of the spin-lock pulse sequence introduced by Lowe and Ailion. The locking frequency $\omega_1/2\pi$ was set to 33.3 kHz.

III. Results & Discussion

^{7}Li NMR Motional Line Narrowing

The fastest method and, in most cases, the first step to probe Li ion dynamics in solid materials is the acquisition of ^{7}Li NMR line spectra [32, 38, 39], see Figure 1. ^{7}Li is a spin-$^3/_2$ nucleus and consequently, as its quadrupole moment is small compared to other quadrupolar nuclei, the ^{7}Li NMR signal of single crystals is expected to be composed of a central line (spin quantum transition $+^1/_2 \leftrightarrow -^3/_2$) and two quadrupole satellites ($+^1/_2 \leftrightarrow +^3/_2$, $-^1/_2 \leftrightarrow -^3/_2$). In the case of a vanishing electric field gradient, because of cubic symmetry around the Li nucleus, the Zeeman energy levels remain, however, undisturbed and the three lines collapse to a single one. Here, only at low temperatures, particularly at $T = 213$ K, we notice quadrupole intensities of rather weak intensities. The intensities of the lines do not change much even if we use spin echo experiments to overcome receiver dead time effects. At very low temperature we observe a broad distribution of satellite transitions. With increasing temperature the broad hump sharpens, because of dipole-dipole averaging effects (see below), and distinct lines show up. We attribute these signals to the electrically inequivalent Li ions sensing non-vanishing electric field gradients (EFGs). In cubic LLZO the Li^+ ions reside on 24*d* and 96*h* sites. Moreover, some of the ions sense the Al^{3+} cations (24*d*) in their direct neighborhood. Full averaging of the EFGs is only seen at sufficiently high temperatures, *i.e.*, when the Li jump rate reaches values comparable to the quadrupolar splitting (50 kHz) [40]. Here, if temperatures up to 453 K are considered, they completely disappear.

The width of the *central* line is determined by homo- and heteronuclear spin interactions; in the case of ^{7}Li, homonuclear dipole-dipole interactions play the dominant role. At sufficiently low temperatures, *i.e.*, at temperatures where the Li diffusivity is frozen with respect to the NMR time scale, the width reaches its largest value, $\Delta\nu_R$. For many materials, dipolar coupling leads to values in the order of

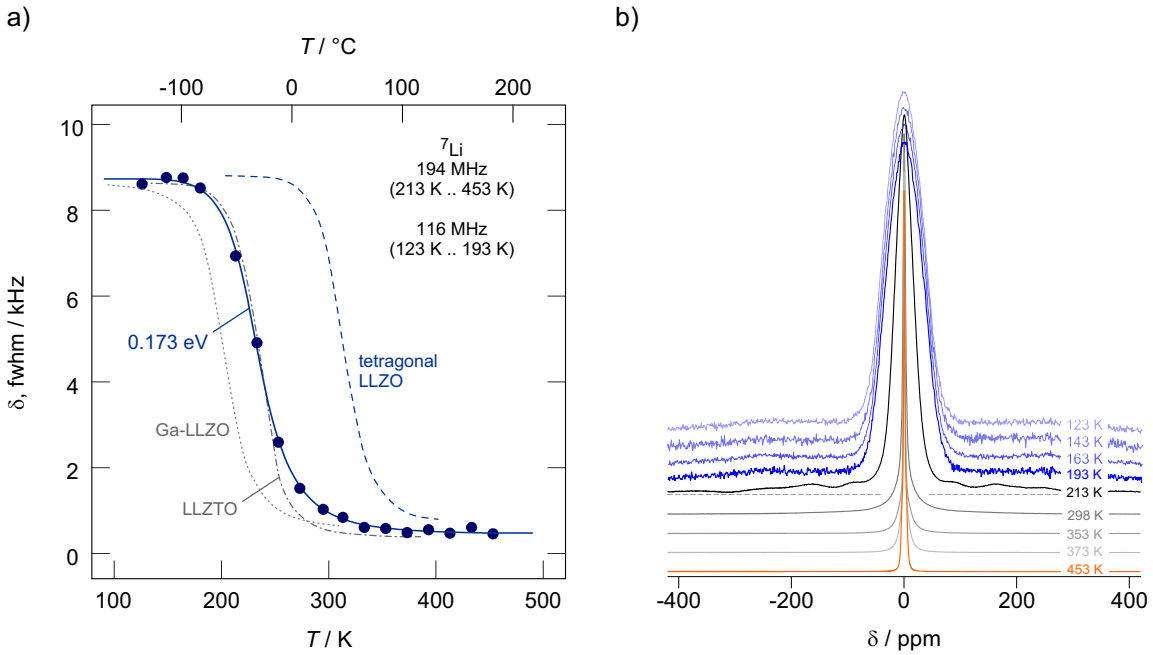

Figure 1: a) ^{7}Li NMR line narrowing of Al-stabilized $Li_7La_3Zr_2O_{12}$. Line widths (full width at half maximum, fwhm) have been determined from ^{7}Li NMR spectra obtained with a single pulse experiment. The line width is independent of the external magnetic field used to acquire the spectra. To record lines at temperatures below 200 K we used a cryo-probe. The solid line represent a fit according to Abragam's formula to describe averaging of homonuclear dipole-dipole interactions. Dashed, dotted and dashed-dotted lines indicate the position of line narrowing curves of powdered tetragonal LLZO, powdered Ga-stabilized LLZO and $Li_6La_3ZrTaO_{12}$ (LLZTO) single crystals. b) ^{7}Li NMR spectra of Al-stabilized LLZO single crystals recorded at the temperatures indicated; see text for further explanation. Again, at temperatures below 200 K spectra have been recorded at a Larmor frequency of 116 MHz.

3 to 15 kHz [39]. The onset of diffusive motions with rates in the order of 10^3 s^{-1}, that is, hopping of Li ions between magnetic inequivalent (and equivalent) sites, causes the line to narrow due to averaging of the effective dipolar couplings. This effect is similar to that of Brownian motion in the liquid state. Hopping between electrically inequivalent sites results in the above-mentioned averaging of EFGs.

Here, the so-called rigid lattice regime of the ^{7}Li NMR central line of single crystalline Al-LLZO is reached at 163 K. This regime features a constant line width $\Delta\nu_R$ of approximately 8.7 kHz, see Figure 1a). With increasing temperature the full width at half maximum (fwhm) of the NMR line continuously decreases, finally reaching a motionally narrowed line at 350 K. The change in fwhm shown in Figure 1 a) follows the behavior predicted by Abragam; it obeys the relationship

$$\Delta(T) = \Delta\nu_R \left[1 + \left(\frac{\Delta\nu_R}{B} - 1 \right) \exp \frac{E_{a,A}}{k_B T} \right]^{-1} + D \qquad (1)$$

which can be used to estimate a mean activation energy that governs motional line narrowing. B is a fitting parameter and k_B denotes Boltzmann's constant. Here, $E_{a,A}$ turned out to be in the order of 0.17 eV. This value perfectly agrees with that seen by ^{7}Li NMR spin-lattice relaxation measurements, which were carried out in the laboratory frame of reference, see below. At the inflexion point of the narrowing curve, the mean Li^+ jump rate (τ^{-1}) is

expected to be in the order of

$$\tau^{-1} = \Delta\nu_R \times 2\pi \quad (2)$$

With $\Delta\nu_R = 8.7$ kHz eqn. (1) yields a rate of ($\tau^{-1} \approx 5.5 \times 10^4$ jumps per second at $T = 233$ K. The position of the whole narrowing curve of single crystalline Al-LLZO is highly comparable to that seen for $Li_6La_3ZrTaO_{12}$ single crystals (see the dashed-dotted line in Fig. 1a), which has been stabilized in its cubic form by replacing one half of the Zr (16*c*) ions by Ta. Both materials also exhibit very similar ionic conductivities. Although similar in shape and in $\Delta\nu_R$, the corresponding curve of polycrystalline, tetragonal $Li_7La_3Zr_2O_{12}$ [28], see the dashed line in Fig.1a), is shifted toward much higher temperature; the onset of line narrowing has been observed at $T = 280$ K pointing to the well-known difference in ion conductivity by a factor of 100 when compared with Al-stabilized LLZO. For comparison, also the motional narrowing curve of a Ga-stabilized LLZO powder sample has been included in Figure 1a), see the dotted line. Depending on the kind and the amount of substituents, Ga^{3+} or Al^{3+}, the onset of the line narrowing curve can be shifted down to temperatures as low as 150 K. Optimized garnet-type LLZO will then exhibit ionic conductivities of at least 1 mS cm^{-1} at room temperature.

7Li NMR Spin-Lattice Relaxation Rates

To throw further light on the underlying Li^+ diffusion mechanisms in Al-LLZO single crystal, we recorded diffusion-induced ^{7}Li NMR spin-lattice relaxation rates ($1/T_1$), see Fig 2a). At low temperatures ($T < 250$ K), the $1/T_1$ rates recorded at $\omega_0/2\pi = 116$ MHz show a non-diffusive, weaker-than-activated background (0.03 eV). All the magnetization transients, some of them are shown in Fig. 2b), follow almost single exponential behavior. If we use stretched exponential to approximate longitudinal recovery, we found the stretching exponents γ_1 to take values very close to 1, see the upper graph of Fig. 2a). Above 280 K rates $1/T_1$ pass into the so-called low-temperature flank of the diffusion-induced rate peak $1/T_1$ ($1/T$) that shows up at $T_{max} = 500$ K. The activation energy $E_{a,NMR1}$ of the low-T flank is 0.20(1) eV, the same value is, as expected, found for $1/T_1$ measured at a higher Larmor frequency of $\omega_0/2\pi = 194$ MHz. Most likely, $E_{a,NMR1}$ is to a large extent influenced by local Li^+ jump processes in the garnet structure. Li^+ ions jump have access to a 3D network of diffusion pathways generated by the 24*d* and 96*h* sites.

In the low-T regime characterized by $\omega_0\tau_c \gg 1$, with τ_c being the motional correlation time, the rate $1/T_1$ depend on frequency. For 3D uncorrelated motion the model of Bloembergen, Purcell and Pound predicts $1/T_1 \propto \omega_0^{-\beta}$ with $\beta = 2$. As $\omega_0\tau_c \approx 1$ is valid at the temperature, T_{max}, at which the peak appears, the peak shifts toward higher T the higher ω_0 has been chosen. As with our setup we are limited in reaching temperatures above 500 K, we could only detect the peak maximum at a frequency of 116 MHz. According to $\omega_0\tau_c \approx 1$ we estimate that the mean Li^+ jump rate $1/\tau$, which is within a factor of 2 expected to be equal to $1/\tau_c$, is in the order of 7.3×10^8 s^{-1}.

Slower Li motional processes can be probed if ω_0 is drastically reduced. Typically, the so-called spin-lock technique is applied to record diffusion-induced spin-lattice relaxation rates at frequencies in the kHz range. By using a locking frequency of 33 kHz the absolute rates increase and the peaks shift toward lower T. This change can be clearly seen in Fig. 2a). If we parameterize the spin-lock magnetization transients with a single stretched exponential we recognize that the corresponding rates $1/T_{1\rho}$ seem to pass through two relaxation peaks. A similar behavior has recently been observed for polycrystalline $Li_{6.5}La_3Zr_{1.75}Mo_{0.25}O_{12}$. The peak at lower temperature, viz. that showing up at 265 K, reveals an activation energy of 0.35 eV in the low-T regime. In contrast to R_1, relaxation in the presence of the much weaker spin-lock field is sensitive to long-range ion transport rather than to short-range motional processes in LLZO. At $T_{max} = 265$ K the associated motional correlation jump rate can be calculated according to $\omega_1\tau_c \approx 0.5$; here we obtain 4.1×10^5 s^{-1}.

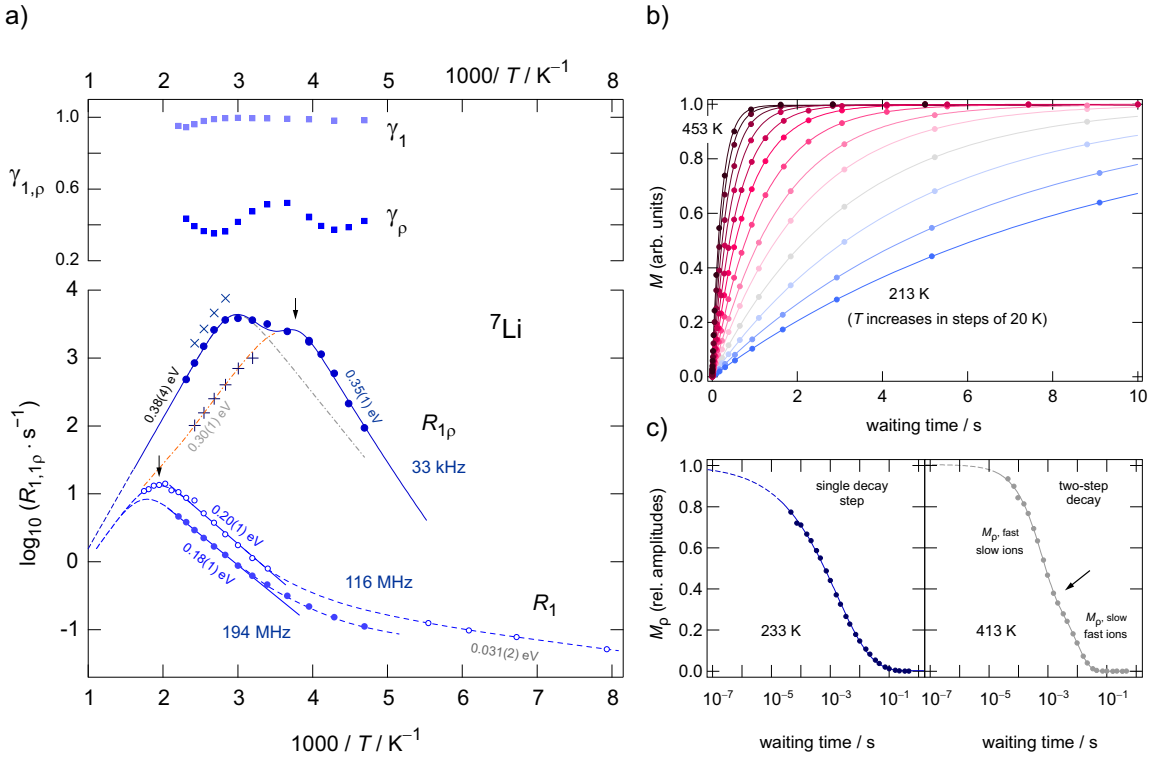

Figure 2: a) ^{7}Li NMR spin-lattice relaxation rates of single crystalline LLZO that were recorded in either the laboratory frame of reference $1/T_1 \equiv R_1$ (116 MHz and 194 MHz) or in the rotating frame of reference ($1/T_{1\rho} \equiv R_{1\rho}$ (33 kHz)). Dashed lines and dashed-dotted lines are to guide the eye. Solid lines show either Arrhenius fits (R_1) or are used as a guide to the eye to illustrate the temperature behaviour of the spin-lock $R_{1\rho}$ rates. We used either stretched exponential functions or a sum of two single exponential functions to parameterize longitudinal (R_1) and transversal relaxation ($R_{1\rho}$). In the upper graph, the corresponding stretching exponents, γ_1 and γ_ρ, are shown. In b) and c) selected magnetization transients M and M_ρ are depicted. Above room temperature the shape of M_ρ is better described by a sum of two stretched exponentials. See text for further explanation.

Interestingly, careful inspection of the spin-lock transients shows that their shape can be best described with a two-step decay behavior. If we do so and use a sum of two stretched exponential functions to parameterize M_ρ, we obtain the rates shown by crosses in Fig. 2a). Obviously, the rates $1/T_{1\rho}$ corresponding to the slower spin-lock relaxation process, marked as $M_{æ,\mathrm{slow}}$ in the two-step decay curve shown in Fig. 2c), represent the high-temperature flank of the rate peak located at $T = 265$ K. Its high-T activation energy of 0.3 eV points to an almost symmetric $1/T_{1\rho}$ ($1/T$) rate peak. Symmetric peaks, whose low-temperature flank is characterized by a slope not smaller than that in the high-T regime ($\omega_1\tau_c \ll 0.5$), are expected for uncorrelated Li ion diffusion. If we extrapolate these rates to higher temperatures we see that they almost coincide with those of the $1/T_1$ ($1/T$) peak recorded at 116 MHz. Hence, the $1/T_{1\rho}$ ($1/T$) peak showing up at 265 K corresponds to the peak seen by the laboratory-frame spin-lattice relaxation measurements.

The spin-lock peak seen at higher temperatures, viz. at $T = 336$ K, points to an activation energy of 0.38 eV. This value is similar to that seen by $T_{1\rho}$ NMR at low temperatures. The rates extracted from our analysis with two stretched exponentials agree well with the rates obtained if we simply use a single (stretched)

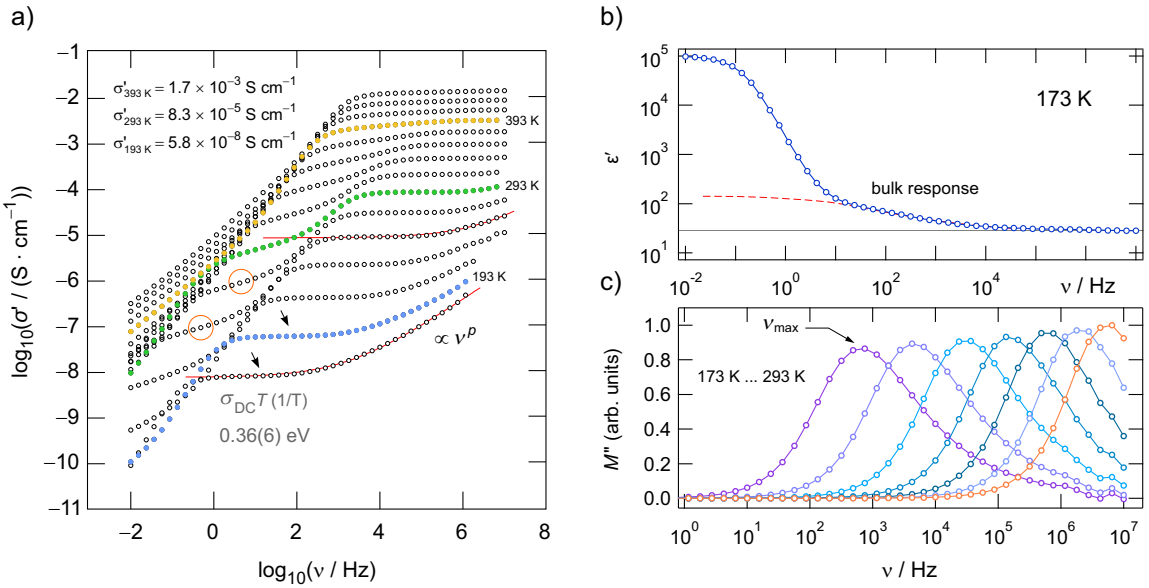

Figure 3: a) Conductivity isotherms of single crystalline Al-stabilized $Li_7La_3Zr_2O_{12}$. Isotherms were constructed by plotting the real part σ' of the complex conductivity versus frequency ν. Solid lines show fits with Jonscher's power law; $p = 0.6$ indicates 3D Li diffusion. At room temperature the frequency independent conductivity plateau yields 8.3×10^{-5} S cm^{-1}. b) Permittivity spectrum of Al-stabilized $Li_7La_3Zr_2O_{12}$ recorded at 173 K. c) Electric modulus spectra; the characteristic frequencies at the top of the peaks, if analyzed in terms of an Arrhenius diagram, reveal almost the same temperature dependence as σ_{DC}, see Figure 5b).

exponential function. This agreement is because the amplitude of this fast relaxation process, $M_{\rho,\text{fast}}$, is larger than $M_{\rho,\text{slow}}$ (see Fig.2c)) and, thus, dominates the fitting results when analyzing the transients this way. While $M_{\rho,\text{fast}}$ is characterized by stretching exponents ranging from 0.75 to 0.82; the exponents for $M_{\rho,\text{slow}}$ range from 0.92 to 1. It is difficult to decide whether $M_{\rho,\text{fast}}$ is to a certain extent already influenced by transversal spin-spin relaxation. Nevertheless, ^{7}Li NMR spin-spin relaxation is expected to be governed by the same activation energy as spin-lock relaxation in the regime $\omega_1\tau_c \ll 1$. Again, the activation energy of 0.38 eV, as seen in the limit $\omega_1\tau_c \ll 1$, reflects long-range Li ion transport in Al-stabilized $Li_7La_3Zr_2O_{12}$. This interpretation is supported by the fact that conductivity measurements on the same sample reveal a very similar value.

Conductivity measurements

In Fig.3a) conductivity spectra $\sigma'(\nu)$ of Al-stabilized LLZO are shown. While electrode polarization dominates the electrical response at low temperatures and low frequencies, well-defined frequency independent plateaus show up at higher frequencies. From these plateaus, which are marked by arrows, we read off direct current ionic conductivities σ_{DC} (see Figure4b)). Permittivity spectra (see Figure 3b)) and Nyquist plots (Figure 4a)) reveal that σ_{DC} refers to capacitance values that are characteristic for bulk electrical relaxation processes. $\epsilon'(\nu \to 0)$ shows values in the order of 100 as expected for bulk ion dynamics, see the dashed line in Fig. 3b). The curvatures seen at frequencies lower than the main dc plateau, marked by a circle in Figure 3a), correspond to permittivities in the order of 10^5. Thus, we do not attribute this response to bulk properties. As expected for such large permittivities (and capacitances) the corresponding peak in electric modulus spectra is reduced by a factor of 10^4 compared to the main peaks shown in Fig-

ure 3c). Most likely, a small poorly conducting layer between the Au electrode and the LLZO single crystal is responsible for this response.

The σ_{DC} plateaus pass into dispersive regions that roughly follow Jonscher's power law. Solid lines in Fig. 3a) represent fits using $\sigma'(\nu) \propto \nu^p$ to approximate the frequency dependence in these regimes. At 193 K we obtained p = 0.6. Values ranging from 0.6 to 0.8 are typically expected for 3D motions of the charge carriers. In general, dispersive regions are indicative for non-independent hopping of the ions; furthermore, they point to time-scale dependent dynamic parameters. Here, at least at low temperatures, the ions are subjected to correlated motions involving the partly occupied 24*d* sites (occupation factor of approximately 0.58, see SI, Table S2 (EK_Al3)) and the 96*h* sites (occupation factor of ca. 0.34, see also SI, Table S2) in LLZO. It is likely that they sense a heterogeneous potential energy landscape and are exposed to forward-backward jump processes. Thus, depending on the time scale the method used to study ion dynamics is sensitive to, different results for activation energies and jump rates are expected. From this point of view it is possible to understand why also R_1 and $R_{1\rho}$, recorded either at frequencies in the MHz or kHz range, deliver quite different activation energies (0.2 eV (R_1) vs. 0.38 eV ($R_{1\rho}$)). Dispersive regions in $\sigma'(\nu)$ result in (slightly) depressed semi-circles when impedance data are presented in a complex plane plot. In Figure 4a) the imaginary part, $-Z''$, of the complex impedance is plotted against its real part Z'. At the apex frequencies $\omega_a = 1/(RC)$ we estimate that the capacitance associated with the electrical response is given by C = 7.5 pF, R denotes the resistance that can be determined from the intercept with the Z' axis. Values in the pF range show that any contributions from gain boundary regions, which would be characterized by capacitances larger than 100 pF, are absent, as expected for a single crystal. Solid lines in Figure 4a) represent fits using an equivalent circuit consisting of the resistance R connected in parallel to a constant phase element (CPE). The shape of the curves in the Nyquist plots does not vary much with temperature. Thus, in the range of low temperatures no change in ionic transport process is seen by impedance spectroscopy.

At room temperature, the ionic conductivity is slightly lower than 10^{-4} S cm^{-1} ($\sigma_{DC} = 8.3 \times 10^{-5}\, S\, cm^{-1}$). Compared to values reported in the literature for Al-LLZO, this value is lower because the amount of Al^{3+} in our single crystal corresponds to only 0.15 mol per formula unit (pfu), as determined by ICP-MS. The optimal Al content to reach conductivities up to 10^{-3} S cm^{-1} should be between 0.2 and 0.3 Al^{3+} pfu.

In Fig. 5b) the temperature dependence of $\sigma_{DC}T$ is shown. The activation energy of $E_{a,DC}$ = 0.36(6) eV is very similar to that seen by spin-lock ($R_{1\rho}$) NMR (0.35 to 0.38 eV, see above) showing that ^{7}Li NMR spin-lattice relaxation if carried out in the rotating-frame of reference is able to probe long-range ion transport. Both, σ_{DC} and ($R_{1\rho}$ take advantage of a frequency window with values in the kHz region to sense the electrical and magnetic fluctuations associated with ionic transport. A very similar activation energy is also obtained if we analyze the temperature dependence of the characteristic relaxation frequencies from the electric modulus peaks of Fig. 3b). In the upper graph of Fig. 4 the change of the rate ω_{max} ($= 2\pi\nu_{max}$) with increasing temperature is shown in an Arrhenius diagram. The fact that $E_{a,DC}$ is a bit higher than $E_{a,M}$ points to a temperature dependent charge carrier concentration N. Obviously, N slightly increases with increasing temperature.

Comparison of Jump Rates from NMR and with Results from Conductivity Spectroscopy

To further compare our results from conductivity measurements with those from NMR relaxometry we converted σ_{DC} into Li^+ jump rates using the Nernst-Einstein equation which connects σ_{DC} with the solid-state diffusion coefficient D_σ.

$$D_\sigma = \frac{\sigma_{DC} \cdot k_B T}{q^2 N} \tag{3}$$

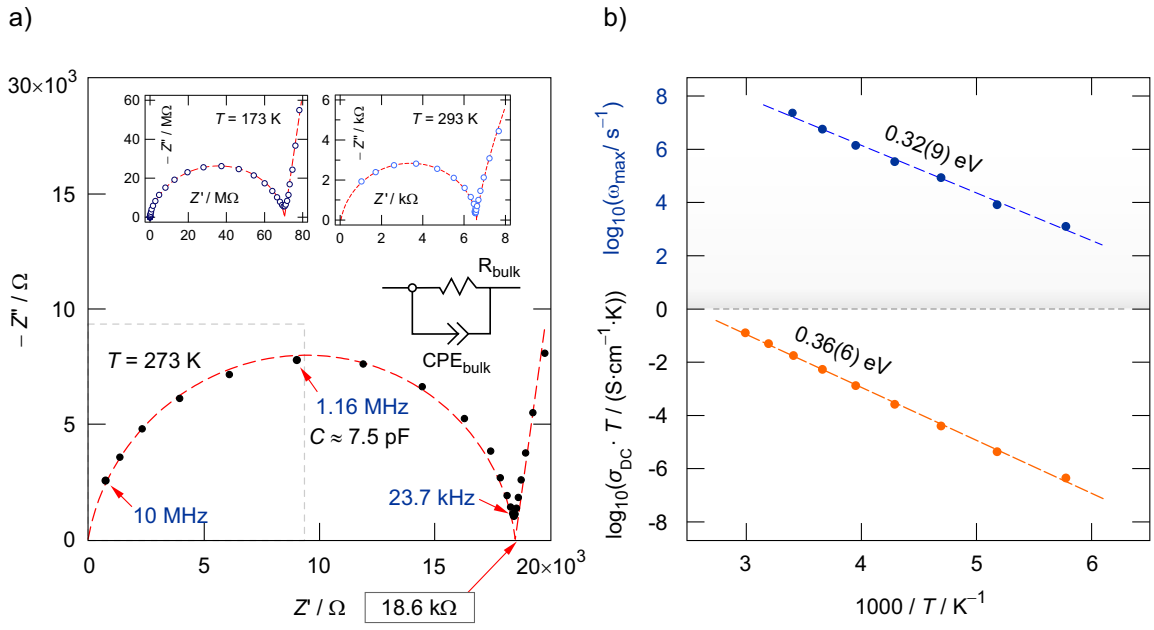

Figure 4: a) Nyquist plots of Al-LLZO single crystals recorded at the temperatures indicated. Dashed lines show simulations with an equivalent circuit that is a combination of a resistor shunt with a CPE, depicted in the in the center section of the graph. b) Temperature dependence of $\sigma_{DC}T$ and ω_{max}, extracted from conductivity spectra and electric modulus peaks. The dashed lines show linear fits following an Arrhenius law.

where q denotes the charge of the ions and N the number density of the charge carriers. D_σ is related to the macroscopic tracer diffusion coefficient via $D_\sigma = (1/H_R)\ D_t$. D_t itself is linked to the self-diffusion coefficient D, which is available by NMR, according to $D_t = fD$. H_R as well as f represent the Haven ratio and the correlation factor, respectively. With $D = D_{NMR} = a^2/(6\tau)$, where a denotes the jump distance, we obtain

$$\tau^{-1} = (H_R/f)\frac{6k_BT}{q^2Na^2}\sigma_{DC} \qquad (4)$$

$1/\tau$ rates from either σ_{DC} or NMR have been plotted vs. the inverse temperature in Fig. 5b). If we first consider the jump rates only deduced from the maxima of the two relaxation rate peaks associated to each other, their position in Fig. 5b) suggests an activation energy comparable to that seen by $\sigma_{DC}T$ (0.36 eV). Results from molecular dynamics simulations, suggesting concerted ion movements, agree with this value [41, 42].

The rates $1/\tau_\sigma$ were calculated by assuming two different jump distances. If we use the 24d-96h distance of 1.67 Å the rates $1/\tau_\sigma$, if referenced to $1/\tau_{NMR}(T_1)$ are larger by a factor of $H_R/f = 0.44$ (≈ 0.5) pointing to correlated ionic motion. Agreement between $1/\tau_\sigma$ and $1/\tau_{NMR}(T_1)$ is achieved if a is increased from 1.67 Å to 2.5 Å. The latter distance serves a good approximation to also include jumps performing $24d - [96h] - 24d$ hopping processes and/or jumps between two $96h$ sites bypassing the $24d$ site (see below and Figure 5a) and Figure 6a)).

We also notice that $1/\tau_{NMR}(T_{1\rho})$ takes a value that is lower than expected by $1/\tau_{NMR}(T_1)$ and $1/\tau_\sigma$. This small difference can be explained by the influence of local magnetic fields that need to be taken into account when estimating $1/\tau_{NMR}$ via $\omega_1\tau_{NMR} = 0.5$ at the maximum of the $1/T_{1\rho}(1/T)$ peak. Replacing ω_1 by an effective frequency $\omega_{eff} = 2\omega_1$ increases $1/\tau_{NMR}(T_{1\rho})$ such that $1/\tau_{NMR}$ agrees

with $1/\tau_\sigma$ if calculated using a = 2.5 Å.

Diffusion Pathways and Assignment of Activation Energies

Coming back to the activation energies seen by NMR spin-lattice relaxation measurements, which range from 0.18 eV to 0.38 eV, and considering possible Li^+ diffusion pathways also discussed in the literature, we suggest the following assignment to Li^+ jump processes. In LLZO, the Li^+ ions are distributed over the 24*d* and 96*h* sites. The latter is a so-called split-atom site; only one of the neighboring 96*h* sites is occupied by one Li^+ ion because of strong repulsive interactions. Li^+ moving in the 96*h*–96*h* (= [96h]) cage (see Figure 5a) and 6a)) is presumably characterized by activation energies lower than 0.1 eV. Such localized motional processes might influence the $1/T_1$ rates governing spin-lattice relaxation at temperatures below 250 K, as suggested before. The $1/T_1$ flank seen above 250 K is, however, assumed to reflect the hopping barrier connecting the sites 96*h* and 24*d* (Figure 5a) and 6a)). The corresponding activation energy (0.18 eV to 0.20 eV, 0.37 wt.-% Al^{3+}) is in good agreement with calculated values that have been presented in literature for Al-LLZO [43]or related structures [44]. If we compare activation energies extracted from the low-T flank of the $1/T_1(1/T)$ NMR spin-lattice relaxation peaks of Al-LLZO powder samples with varying Al content, we see that lower activation energies (0.12 eV (0.9 wt.-% Al^{3+}) [17]; 0.13 eV (0.5 wt.-% Al^{3+}) [21]) are obtained for samples with higher amounts of Al^{3+} ions. Hence, Al^{3+} incorporation does not only stabilize the cubic crystal structure, it also seems to influence the mean activation energy of the elementary, local 24*d*-96*h* forward-backward jump process. However, this conclusion has to be taken with great care as powder samples prepared by sintering in many cases suffer from chemical inhomogeneity. As has been shown recently for powdered samples, Al^{3+} tends to heterogeneously distribute over the crystallites [26]. Such heterogeneous distribution has even been found inside the μm-sized grains. Here, for the dense single crystal investigated a homogenous distribution is present.

The activation energy seen by $1/T_{1\rho}$ measurements in the limit $\omega_1\tau_c = 1$ (0.3 eV) is expected to be governed by long-range transport processes, thus taking into account 24*d*-[96*h*]-24*d* hopping processes (Figure 5a)). The activation energy of 0.3 eV agrees with those calculated for this type of pathway [45].

Even higher values ranging from 0.35 to 0.38 eV, which perfectly agree with $E_{a,DC}$, are anticipated to reflect further exchange processes. Although still under debate, direct Li^+ jumps between two [96*h*] voids (a = 0.234 Å), using a curved pathway, might contribute to the overall ion transport in Al-LLZO, too [43]. As has been shown recently by García Daza *et al.* [46] using molecular dynamic simulations, Li^+ diffusivity in the direct neighborhood of Al^{3+} (see Figure 6a)) is decreased compared to the regions farther afield. They showed that vacancies generated by trivalent doping remain in the direct vicinity of Al^{3+} without any effect in enhancing the Li^+ diffusivity of the adjacent Li^+ ions. We also suppose that the second $1/T_{1\rho}$ NMR peak yielding an activation energy of 0.38 eV reflects less mobile Li^+ ions that are indeed influenced by the blocking effect of the Al^{3+} ions. As Al^{3+} is almost immobile with respect to the rapidly diffusing Li^+ ions, the pathway $24d - [96h] - Al^{3+}(24d) - [96h] - 24d$ in its direct vicinity is blocked [47]. This blocking effect might force the ions to bypass the 24*d* position, thus directly jumping between two [96*h*] voids – possibly these jumps occur in the outer spheres of the regions blocked by Al^{3+}.

Single Crystals versus Powder Samples

Finally, we compare ^{7}Li NMR $1/T_{1\rho}$ data from powder samples with that obtained in this study, see Figure 6b). It has been a mystery why the response in powders samples prepared by solid-state reaction always lead to an extremely broad $1/T_{1\rho}$ "peak" [17, 21]. Most likely, chemical inhomogeneity concerning Al^{3+} distribution, as mentioned above, leads to a superposition of several $1/T_{1\rho}(1/T)$ peaks hindering the very accurate determination of activation energies. For the single

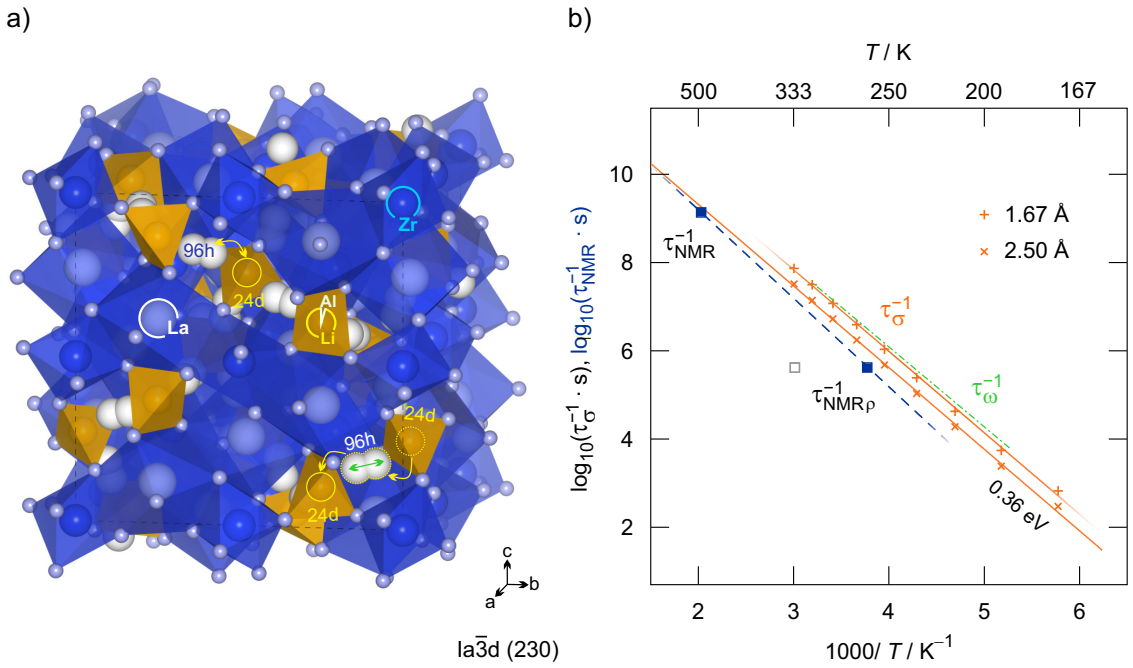

Figure 5: a) Crystal structure of LLZO. The Li ions jump between the sites 24*d* and 96*h*. Also jumps directly between 96*h*, passing by the tetrahedral site 24*d*, which is partly occupied by the immobile Al^{3+} ions, are indicated, see also Figure 6a) that shows possible Li^+ pathways in more detail. b) Li jump rates as deduced from conductivity and NMR spectroscopy. For comparison, characteristic hopping rates obtained from analyzing electric modulus spectra are also included; these rates have been indicated by the dashed-dotted line. $1/\tau_\sigma$ has either been calculated with a = 1.67 Å (+) or with a = 2.50 Å (×). The open symbol (■) refers to the $1/T_{1\rho}(1/T)$ NMR peak showing up at high temperatures.

crystal studied here, this distribution is much smaller leading to sharp diffusion-induced ^{7}Li NMR rate peaks.

Interestingly, heterogeneous Al^{3+} distribution is only reflected in long-range ion dynamics, to which $T_{1\rho}$ NMR is sensitive. The shape of the $1/T_1(1/T)$ rate peaks, on the other hand, seem to be less influenced by the overall distribution of the trivalent cations.

IV. Conclusion

Ion dynamics in Al-stabilized Czochralski-grown single crystals of the composition $Li_{6.46}Al_{0.15}La_3Zr_{1.95}O_{11.86}$ was studied by both ^{7}Li NMR relaxometry, including line shape measurements, and broadband conductivity spectroscopy. As compared to powder samples, which are usually prepared by solid-state reaction and, thus, may suffer from chemical inhomogeneities, we benefit here from a highly dense sample whose Al^{3+} distribution is assumed to be homogeneous. While conductivity spectroscopy probes long-range ion transport that is governed by an overall activation energy of 0.36 eV, ^{7}Li NMR spin-lattice relaxation measurements provided details about activation energies (0.18 eV – 0.38 eV) that describe both local barriers of the elementary jump processes and diffusion on a larger length scale. In particular, Li^+ exchange between the vacancy-rich crystallographic sites 24*d* and 96*h* turned out to be characterized by relatively low activation energies ranging from 0.18 eV to 0.20 eV. From an experimental point of view, we cannot exclude that also direct jumps between two neighboring 96*h*-96*h*′ voids bypassing the tetrahedral 24*d* sites do also participate in overall

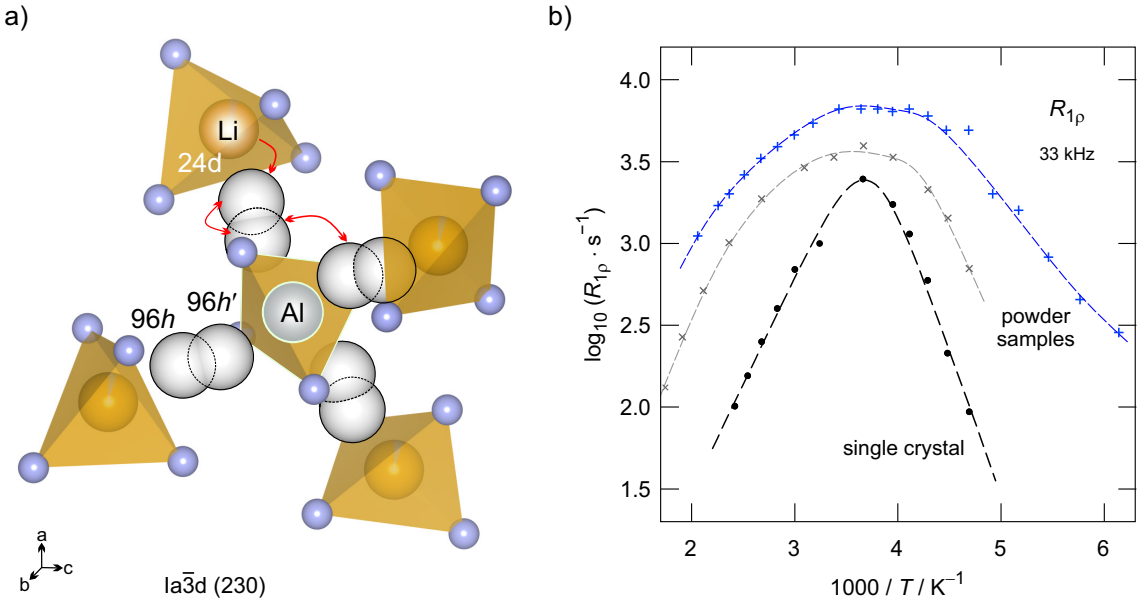

Figure 6: a) Li^+ jump processes using the sites 24*d* and 96*h*. Al^{3+} ions located at 24*d* block the pathway $96h - 24d - 96h$. b) Comparison of diffusion-controlled ^{7}Li NMR $1/T_{1\rho}$ rates of Al-LLZO powder samples (data points taken from ref. [21](×, 0.49 wt.-% Al^{3+}) and ref. [17] (+, 0.9 wt.-% Al^{3+}) with those measured in this study using a single crystal (0.37 wt.-% Al^{3+}). The extremely broad $1/T_{1\rho}(1/T)$ rate peak seen for powder samples is, most likely, due to a heterogeneous distribution of Al^{3+} cations leading to a superposition of relaxation rate peaks.

ion dynamics.

V. Acknowledgement

This project has received funding from the European Union's Horizon 2020 research and innovation programme under grant agreement no. 769929. Financial support by the Federal Ministry of Science, Research and Economy and the National Foundation for Research, Technology and Development (CD-Laboratory of Lithium Batteries: Ageing Effects, Technology and New Materials) is also gratefully acknowledged. Moreover, we thank NAWI Graz and the DFG for further financial support (WI3600, 2-1/4-1). Additional financial support by the FFG in the frame of the K-project 'safe battery' for financial support is also gratefully acknowledged.

References

[1] U. Nations, *United Nation* **1998**, *7*, 214–217.

[2] D Larcher, J.-M. Tarascon, *Nature Chemistry* **2014**, *7*, 19.

[3] M. Winter, R. J. Brodd, *Chemical Reviews* **2004**, *104*, 4245–4270.

[4] I. Buchmann, *Batteries in a portable world : A handbook on rechargeable batteries for non-engineers. 2nd ed.* Cadex Electronics Inc., Richmond, BC, Canada, **2001**.

[5] M Armand, J.-M. Tarascon, *Nature* **2008**, *451*, 652.

[6] M. M. Thackeray, C. Wolverton, E. D. Isaacs, *Energy and Environmental Science* **2012**, *5*, 7854–7863.

[7] P. G. Balakrishnan, R. Ramesh, T. Prem Kumar, Safety mechanisms in lithium-ion batteries, **2006**.

[8] F. Zheng, M. Kotobuki, S. Song, M. O. Lai, L. Lu, *Journal of Power Sources* **2018**, *389*, 198–213.

[9] Y. Kato, S. Hori, T. Saito, K. Suzuki, M. Hirayama, A. Mitsui, M. Yonemura, H. Iba, R. Kanno, *Nature Energy* **2016**, *1*, 16030.

[10] A. Hayashi, K. Noi, A. Sakuda, M. Tatsumisago, *Nature Communications* **2012**, *3*, 856.

[11] Y. Wang, W. D. Richards, S. P. Ong, L. J. Miara, J. C. Kim, Y. Mo, G. Ceder, *Nature Materials* **2015**, *14*, 1026.

[12] R. Murugan, V. Thangadurai, W. Weppner, *Angewandte Chemie - International Edition* **2007**, *46*, 7778–7781.

[13] N. Kamaya, K. Homma, Y. Yamakawa, M. Hirayama, R. Kanno, M. Yonemura, T. Kamiyama, Y. Kato, S. Hama, K. Kawamoto, A. Mitsui, *Nature Materials* **2011**, *10*, 682.

[14] M. Uitz, V. Epp, P. Bottke, M. Wilkening, *Journal of Electroceramics* **2017**, *38*, 142–156.

[15] V. Thangadurai, D. Pinzaru, S. Narayanan, A. K. Baral, *The Journal of Physical Chemistry Letters* **2015**, *6*, 292–299.

[16] S. Ohta, T. Kobayashi, J. Seki, T. Asaoka, *Journal of Power Sources* **2012**, *202*, 332–335.

[17] H. Buschmann, J. Dölle, S. Berendts, A. Kuhn, P. Bottke, M. Wilkening, P. Heitjans, A. Senyshyn, H. Ehrenberg, A. Lotnyk, V. Duppel, L. Kienle, J. Janek, *Physical Chemistry Chemical Physics* **2011**, *13*, 19378–19392.

[18] A. Kuhn, S. Narayanan, L. Spencer, G. Goward, V. Thangadurai, M. Wilkening, *Physical Review B - Condensed Matter and Materials Physics* **2011**, *83*, 1–11.

[19] J. Awaka, N. Kijima, H. Hayakawa, J. Akimoto, *Journal of Solid State Chemistry* **2009**, *182*, 2046–2052.

[20] V. Thangadurai, S. Narayanan, D. Pinzaru, *Chemical Society Reviews* **2014**, *43*, 4714–4727.

[21] R. Wagner, G. J. Redhammer, D. Rettenwander, A. Senyshyn, W. Schmidt, M. Wilkening, G. Amthauer, *Chemistry of Materials* **2016**, *28*, 1861–1871.

[22] J. L. Allen, J. Wolfenstine, E. Rangasamy, J. Sakamoto, *Journal of Power Sources* **2012**, *206*, 315–319.

[23] E. Rangasamy, J. Wolfenstine, J. Sakamoto, *Solid State Ionics* **2012**, *206*, 28–32.

[24] D. Rettenwander, G. Redhammer, F. Preishuber-Pflügl, L. Cheng, L. Miara, R. Wagner, A. Welzl, E. Suard, M. M. Doeff, M. Wilkening, J. Fleig, G. Amthauer, *Chemistry of Materials* **2016**, *28*, 2384–2392.

[25] B. Kozinsky, S. A. Akhade, P. Hirel, A. Hashibon, C. Elsässer, P. Mehta, A. Logeat, U. Eisele, *Physical Review Letters* **2016**, *116*, 055901.

[26] A. Wachter-Welzl, J. Kirowitz, R. Wagner, S. Smetaczek, G. C. Brunauer, M. Bonta, D. Rettenwander, S. Taibl, A. Limbeck, G. Amthauer, J. Fleig, *Solid State Ionics* **2018**, *319*, 203–208.

[27] D. O. Shin, K. Oh, K. M. Kim, K.-Y. Park, B. Lee, Y.-G. Lee, K. Kang, *Scientific Reports* **2015**, *5*, 18053.

[28] B. Stanje, D. Rettenwander, S. Breuer, M. Uitz, S. Berendts, M. Lerch, R. Uecker, G. Redhammer, I. Hanzu, M. Wilkening, *Annalen der Physik* **2017**, *529*, 1–9.

[29] I. Kokal, M. Somer, P. Notten, H. Hintzen, *Solid State Ionics* **2011**, *185*, 42–46.

[30] Y. Zhang, F. Chen, R. Tu, Q. Shen, L. Zhang, *Journal of Power Sources* **2014**, *268*, 960–964.

[31] Y. Kim, H. Jo, J. L. Allen, H. Choe, J. Wolfenstine, J. Sakamoto, *Journal of the American Ceramic Society* **2016**, *99*, 1367–1374.

[32] V Epp, Ö Gün, H.-J. Deiseroth, M Wilkening, *Physical Chemistry Chemical Physics* **2013**, *15*, 7123–7132.

[33] V. Epp, Ö. Gün, H. J. Deiseroth, M. Wilkening, *Journal of Physical Chemistry Letters* **2013**, *4*, 2118–2123.

[34] P. Bottke, D. Rettenwander, W. Schmidt, G. Amthauer, M. Wilkening, *Chemistry of Materials* **2015**, *27*, 6571–6582.

[35] A. Kuhn, M. Kunze, P. Sreeraj, H. D. Wiemhöfer, V. Thangadurai, M. Wilkening, P. Heitjans, *Solid State Nuclear Magnetic Resonance* **2012**, *42*, 2–8.

[36] M. Wilkening, P. Heitjans, *ChemPhysChem* **2012**, *13*, 53–65.

[37] S. Narayanan, V. Epp, M. Wilkening, V. Thangadurai, *RSC Advances* **2012**, *2*, 2553–2561.

[38] M Wilkening, V Epp, A Feldhoff, P Heitjans, *The Journal of Physical Chemistry C* **2008**, *112*, 9291–9300.

[39] M. Wilkening, S. Indris, P. Heitjans, *Physical Chemistry Chemical Physics* **2003**, *5*, 2225–2231.

[40] R. Bertermann, W. Müller-Warmuth, *Zeitschrift fur Naturforschung - Section A Journal of Physical Sciences* **1998**, *53*, 863–873.

[41] S. Adams, R. P. Rao, *Journal of Materials Chemistry* **2012**, *22*, 1426–1434.

[42] R. Jalem, Y. Yamamoto, H. Shiiba, M. Nakayama, H. Munakata, T. Kasuga, K. Kanamura, *Chemistry of Materials* **2013**, *25*, 425–430.

[43] K. Meier, T. Laino, A. Curioni, *Journal of Physical Chemistry C* **2014**, *118*, 6668–6679.

[44] L. J. Miara, S. P. Ong, Y. Mo, W. D. Richards, Y. Park, J. M. Lee, H. S. Lee, G. Ceder, *Chemistry of Materials* **2013**, *25*, 3048–3055.

[45] M. Xu, M. S. Park, J. M. Lee, T. Y. Kim, Y. S. Park, E. Ma, *Physical Review B - Condensed Matter and Materials Physics* **2012**, *85*, 1–5.

[46] F. A. García Daza, M. R. Bonilla, A. Llordés, J. Carrasco, E. Akhmatskaya, *ACS Applied Materials & Interfaces* **2019**, *11*, 753–765.

[47] D. Rettenwander, P. Blaha, R. Laskowski, K. Schwarz, P. Bottke, M. Wilkening, C. A. Geiger, G. Amthauer, *Chemistry of Materials* **2014**, *26*, 2617–2623.

^{7}Li NMR Resolves Diffusion Pathways in Single Crystalline Ga-Stabilized $Li_7La_3Zr_2O_{12}$

Patrick Posch[a]*, Lincoln J. Miara[b], Stefan Berendts[c], Steffen Ganschow[d], Daniel Rettenwander[a], H. Martin R. Wilkening[a]‡

[a]Institute for Chemistry and Technology of Materials, Christian Doppler Laboratory for Lithium Batteries, Graz University of Technology (NAWI Graz), Graz, Austria

[b]Advanced Materials Lab, Samsung Research America, 3 Van de Graaff Drive, Burlington, Massachusetts, United States

[c]Department of Chemistry, Berlin University of Technology, Berlin, Germany

[d]Leibniz Institute for Crystal Growth (IKZ), Berlin, Germany

*p.posch@tugraz.at

‡see also for correspondence: wilkening@tugraz.at

Abstract

High Li-ion conductivities in combination with high electrochemical stability are the prerequisites for solid electrolytes needed to enable future solid-state batteries with high power density and energy density. Among known solid electrolytes, $Li_7La_3Zr_2O_{12}$ (LLZO) belongs to the most promising candidates fulfilling these requirements. Despite of all the research performed on this class of materials, in particular questions about the fundamental Li-ion transport properties remain unanswered. Therefore, we employ ^{7}Li nuclear magnetic resonance (NMR) spin-lattice relaxation and conductivity spectroscopy of Czochralski grown single crystals of acentric cubic structured Ga-stabilized LLZO to shed light on diffusion processes over a broad time frame. Long-ranged ion dynamics exhibit an overall conductivity of 1.1 mS cm^{-1} at 293 K with an activation energy of 0.3 eV. Diffusion processes on shorter ranges, as sensed by the spin-lock NMR technique, can be divided into 2 Li^+ hopping pathways. These two processes can be assigned to Li^+ motion between distinct sites by using computer assisted simulations. One of these motional processes is activated at much lower temperatures than the other one, viz., 203 K opposed to 243 K. At even smaller time frames, as sensed by spin-lattice relaxation NMR, an energy barrier of 0.13 eV characterizes local forward-backward Li^+ jumps between 12*a* and 48*e* sites of the lattice. To fully elucidate Li dynamics in the highly conductive acentric garnet modification, identification of the individual hopping processes is of utmost importance.

Keywords: LLZO, single crystal, Ga-substituted, NMR, dynamics

I. Introduction

Mobility and transportation play vital roles in our modern economy [1, 2]. Electric mobility taps new markets all over the globe and throughout all classes of society [3–5]. Latest reports on incidents with electrochemical energy storage devices, especially such comprising flammable liquid electrolytes, call manufacturers to action [6–8]. All-solid-state batteries (ASSBs) emerge as highly potent candidates to resolve this issue [9, 10]. Centerpiece of such ASSBs is the solid-state electrolyte that connects the batter-

ies electrodes via ion diffusion. A variety of solid electrolyte materials, including sulfides, oxides and polymer based systems, entered the spotlight in the last decade [11–13]. To be considered suitable replacements, such electrolytes must exhibit wide electrochemical stability windows, good stability at ambient conditions and reasonably high ionic conductivity [14, 15]. A promising candidate for commercialization is garnet-type $Li_7La_3Zr_2O_{12}$ [16]. The three common polymorphs of LLZO garnets were established so far, viz., the tetragonal structure ($I4_1/acd$), the cubic phase with centric space group ($Ia\bar{3}d$) and the acentric cubic polymorph ($I\bar{4}3d$), are illustrated in Figure 1 [17–19]. However, the high conductivity requirements for solid-electrolyte application are only met by the cubic polymorphs that exhibit room-temperature (RT) conductivities of more than 2 magnitudes higher ($\sigma_{total} > 10^{-4}$) than their tetragonal analogs ($\sigma_{total} > 10^{-6}$) [16]. Luckily, stabilization of said cubic phases at RT is accomplished by introducing small amounts of supervalent cations to the structure. Initiated by unintended incorporation of Al^{3+} from alumina crucibles [20, 21], a multitude of other cations surfaced that served the same purpose [22–27]. Furthermore, said substitution with supervalent cations entails formation of Li^+ vacancies according to $3\,Li^+ \rightarrow M^{3+} + 2\,\square_{Li}$ or $Zr^{4+} + Li^+ \rightarrow M^{5+} + \square_{Li}$. The site preference of the introduced stabilization cations is a controversially discussed topic. Aside from initial thoughts, recent reports show that the garnet-type structure ($Ia\bar{3}d$) also exists in an acentric cubic modification ($I\bar{4}3d$, No. 220) [19]. This novel polymorph, *i.e.*, only formed by incorporation of Ga^{3+} or Fe^{3+} ions, comprises a reduction in symmetry that is most probably caused by the site preference of the substituents [28]. The assumption that supervalent substituents that reside on Li^+ sites adversely affect the Li diffusion by blocking lattice sites does not hold for Ga^{3+} and Fe^{3+} stabilized LLZO garnets, which exhibit the highest conductivities ever reported for this class of materials. However, the particular influence of substituents on the ion dynamics in Li bearing garnets is yet unclear. The complexity to study these Li-ion dynamics in ion conducting ceramics as a fundamental material property, rather than sample specifics, is strongly related to chemical inhomogeneities within samples and is governed by strong sample-to-sample variations [29, 30].

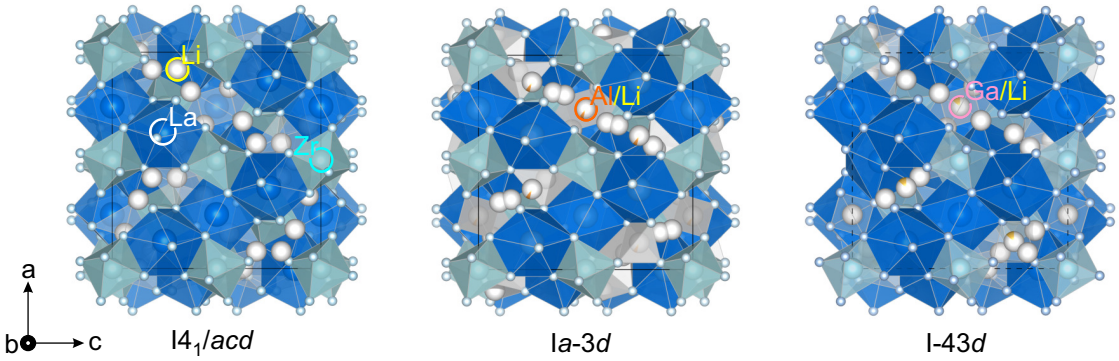

Figure 1: Crystal polymorphs of $Li_7La_3Zr_2O_{12}$, tetragonal $I4_1/acd$ (left), centric cubic $Ia\bar{3}d$ (middle) and acentric cubic $I\bar{4}3d$ (right). ZrO_6 octahedra are depicted in light blue, whereas the LaO_8 trigonal dodecahedra are shown in dark blue. Lithium ions are illustrated as white spheres and occupy several lattice sites in the particular structures. In $Ia\bar{3}d$ Li^+ ions reside on 24*d* tetrahedral sites and hop between 4-fold coordinated 96*h* and distorted 6-fold coordinated 48*g* sites. In the acentric polymorph, those 24*d* sites are split into 12*a* and 12*b* positions that are connected by 6-fold coordinated 48*e*, viz., an equivalent to 48g, sites. Foreign atom stabilization of the cubic polymorphs with Al^{3+} on 24*d* sites in $Ia\bar{3}d$ and Ga^{3+} on 12*a* sites in $I\bar{4}3d$ is indicated by open circles.

These inhomogeneities, that also occur among the particles of polycrystalline samples, entail difficulties in accurate description of the underlying structural and dynamic properties.

Therefore, this work is dedicated to disclosure of bulk ion dynamics of Ga-stabilized LLZO single crystals grown by Czochralski method. We sense long-range ionic motion with the help of alternate current (AC) conductivity spectroscopy. To resolve ion hopping in smaller time frames, ^{7}Li nuclear magnetic resonance (NMR) is employed. Temperature variable spin-lattice relaxation measurements are carried out in both, the laboratory and the rotating frame of reference to enhance comparability with AC conductivity data. In stark contrast to ion dynamics in polycrystalline materials, experiments performed in the rotating frame of reference sense 2 distinctive jump processes in the single crystalline sample.

II. Methods

Synthesis

The widely known Czochralski method was used to grow single crystalline Ga-substituted LLZO directly from the melt. Li_2CO_3 (99 % Merck), La_2O_3 (99.99 %, Aldrich), Ga_2O_3 (99.0 %, Aldrich) and ZrO_2 (99.0 %, Aldrich) were dried and subsequently used as reagents for the synthesis. A stoichiometric mixture, consisting of the aforementioned educts and an excess of 10 wt% Li_2CO_3, was uniaxially pressed into pellet form and annealed at 1123 K for 4 h. The heating rate was set to 5 K per minute. Afterwards, the sintered pellet was melt in an inductively heated iridium crucible that was combined with a 25-kW microwave generator. In inert nitrogen atmosphere, the crystal was pulled from the melt at constant rotation and speed, viz., 10 rpm and 1.5 mm h^{-1}, respectively. An iridium rod served as crystallization seed. Inductively coupled plasma mass spectrometry (ICP-MS) was carried out to determine the exact chemical composition of the crystal. Considering its Ga^{3+} weight content of 1.67 % and normalizing the formula to 2 Zr^{4+} yields a composition of $Ga_{0.2}Li_{6.54}La_{2.92}Zr_2O_{11.95}$.

Sample Preparation

The colorless crystal was cut to smaller pieces of approximately 3 mm × 4 mm × 2 mm, which were then polished using a Struers LaboPOL-25 device. SiC abrasive paper with a large variety of grits, viz., 500, 800, 1200, 2400 and 4000, was employed to smoothen the surface before polishing with 3 μm diamond suspension to yield a high shine finish. A Leica sputter device was used to apply 100 nm thick gold electrodes on top and bottom surfaces of one crystal. To prepare another crystal for static ^{7}Li NMR measurements, its dimensions were reduced to approx. 1 mm × 1 mm × 4 mm to fit the Duran NMR-tube. Leftover pieces of Whatman GF/B glass filters were used to center the sample and shield it from overheating during the fire sealing process.

AC Conductivity

Conductivity measurements were performed using a Novocontrol Concept 80 broadband analyzer. The device was connected to a BDS 1200 cell that sported an active ZGS cell interface for precise tuning of the measurement environment. Temperature-variable measurements were carried out with the help of a QUATRO cryosystem that evaporates liquid nitrogen in a dewar vessel. At specified pressures, the gaseous nitrogen flows through the measuring cell and enables precise control of the temperature with deviations lower than ± 0.1 K. This setup is used to record data at frequencies ranging from 100 mHz to 10 MHz at temperatures between 173 K and 453 K.

^{7}Li Nuclear magnetic resonance

An Avance III spectrometer, in combination with an Ultrashield 300 MHz widebore magnet, was used to acquire ^{7}Li spin-lattice relaxation data. At a nominal field of 7 T, the Larmor frequency ($\omega_0/2\pi$) of the ^{7}Li nucleus equals 116 MHz. A ceramic probe head is employed to perform temperature-variable measurements

ranging from 183 K to 573 K. Temperatures were set by a Eurotherm temperature controller and measured by a Cu-CuNi thermocouple in close proximity to the sample. At a power output of 200 W, $\pi/2$ pulse lengths varied between 2.02 and 2.23 μs. Measurements between 116 K and 183 K were performed with a cryo probe head that makes use of freshly evaporated liquid N_2 to reach cryogenic temperatures. The latter is controlled by a Lakeshore Model 311 that is equipped with two Cernox resistance sensors to keep track of the temperature at the cryostat and close to the sample. The use of this probe head enables measurements at an output power of 80 W and corresponding $\pi/2$ pulse lengths between 4.28 and 4.65 μs. ^{7}Li spin-lattice relaxation rates (R_1) in the laboratory frame of reference were acquired by employing the renowned saturation recovery pulse sequence, $10 \times \pi/2 - t_d - \pi/2 -$ acquisition (acq.) [31]. Multiple initial $\pi/2$ pulses are applied in a fast destructive manner to observe the relaxation of M_z as a function of delay time (t_d) and free from remaining longitudinal magnetization. Spin-lock NMR experiments were carried out with the help of a pulse sequence introduced by Ailion and Slichter [32–34]. Here, a spin-lock pulse $p(t_{lock})$) is employed directly after a $\pi/2$ pulse to lock the magnetization (M_ρ) in the $(x, y)'$-plane. The decay of said magnetization in the locking field B_1, in our case $\gamma B_1 = \omega_1 = 207$ kHz, follows the duration of the locking pulse in functional dependency and is usually induced by slow Li ion motion. The acquired data shed light on correlation rates and energy barriers of aforementioned ionic motions.

III. Results & Discussion

^{7}Li line shape measurements and motional narrowing

Prior to spin-lattice relaxation measurements, temperature variable static ^{7}Li NMR line spectra of Ga-stabilized LLZO, as shown in Fig. 2, provide initial insight into ion dynamics. These lines are, as a consequence of ^{7}Li being a $^3/_2$ spin nucleus with a rather small quadrupole moment, expected to consist of a central transition and two quadrupolar satellite signals. In our case, however, only collapsed lines can be observed; a clear indication for cubic symmetry surrounding the Li nucleus. Otherwise, disturbance of the Zeeman energy levels would lead to the expected line splitting. An attempt to employ a solid echo pulse sequence ($\pi/2 - t_d - \pi/2 - t_d - \pi/2 -$ acq.), usually applied to overcome receiver dead times and resolve satellite signals, results in similar line spectra. However, at temperatures below RT electrically inequivalent Li ions respond to non-vanishing electric field gradients (EFGs), which results in broadening of the central transition. At much lower temperatures, viz., below 203 K, a wide distribution of satellite transitions takes part in generating a very broad central signal. Many materials enter the rigid lattice regime at sufficiently low T, *i.e.*, total immobilization of the Li ions in the material, as seen by NMR. Figure 1a shows that monocrystalline Ga stabilized LLZO leaves the rigid lattice regime, exhibiting a line width of $\Delta\nu_{RL} \approx 9$ kHz, at approximately 110 K. This material specific temperature is often referred to as the onset temperature. It represents a fast and qualitative method to compare ion mobility in various materials. To make use of this feature, the graph also illustrates motional narrowing of other garnet single crystals, viz., $Li_6La_3ZrTaO_{12}$ (LLZTO) and $Li_{6.46}Al_{0.15}La_3Zr_{1.95}O_{11.86}$ (Al-LLZO), that both exhibit an onset temperature of 163 K at a $\Delta\nu_{RL}$ of 8.7 kHz. Additionally, motional narrowing of its unsubstituted tetragonal ancestor $Li_7La_3Zr_2O_{12}$ is represented in light grey dotted lines and reveals an onset temperature of 280 K at similar $\Delta\nu_{RL}$. Li ions start hopping between magnetically equivalent and inequivalent sites and line narrowing sets in. After its slow start, motional narrowing picks up speed and reaches the inflection point. At this point, the mean Li^+ jump rate, τ^{-1}, can be calculated according to the relation $\tau^{-1} = \Delta\nu_{RL} \times 2\pi$. Hence, τ^{-1} yields 5.7×10^4 jumps per second at T = 195 K at a frequency $\Delta\nu_{RL}$ of 9 kHz. As

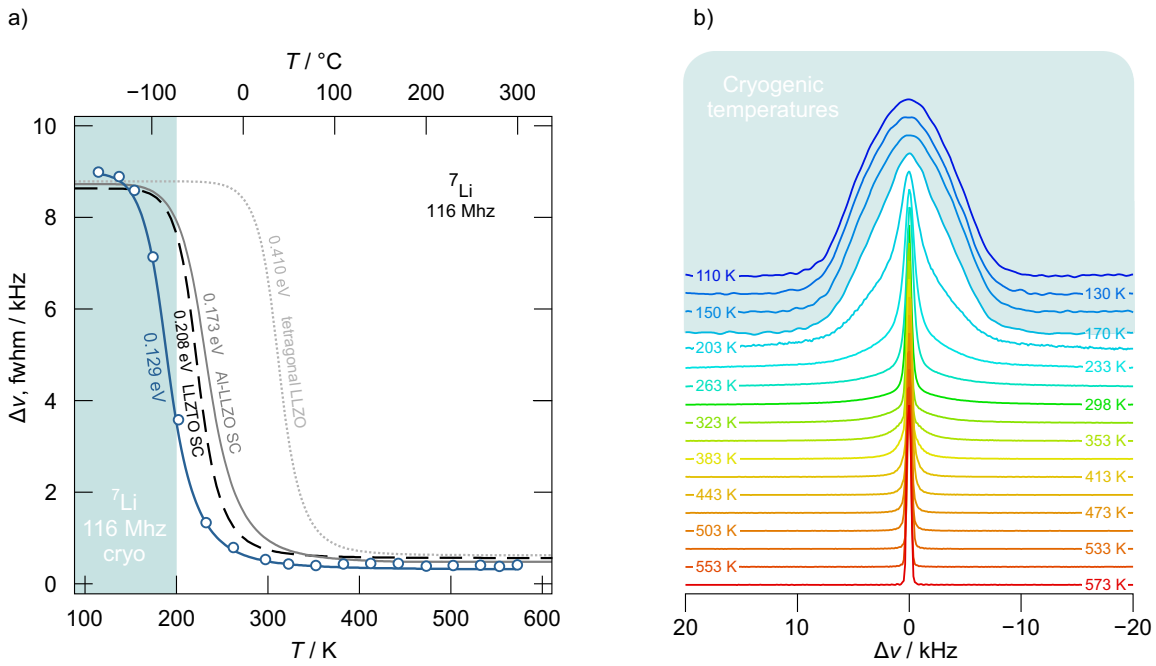

Figure 2: a) ^{7}Li NMR line measurements carried out at Larmor frequency of 116 MHz. a) illustrates motional narrowing behavior of monocrystalline Ga-substituted LLZO (solid blue), $Li_6La_3ZrTaO_{12}$ (LLZTO, dashed black), Al-LLZO (solid grey) and polycrystalline tetragonal LLZO (dotted grey) samples. b) depicts line narrowing of a Ga-substituted LLZO single crystal. Aqua colored background indicates cryogenic temperatures.

a consequence of comparable line widths in the rigid lattice regime, calculations of the different materials yield almost similar Li^+ jump rates. The corresponding temperatures of the inflection points, however, reveal tremendous differences in Li diffusivity. Slowest movement of Li ions can be observed in tetragonal LLZO, which exhibits $\tau^{-1} = 5.5 \times 10^4\,s^{-1}$ at 280 K. The temperature dependence of the inflection points ranks Ga-LLZO > LLZTO > Al-LLZO > tetragonal LLZO in terms of Li^+ diffusivity from fast to slow. Previous studies report conductivity differences of 2 orders of magnitude between tetragonal and cubic LLZO symmetries, which will be discussed in more detail later on [35]. At sufficiently high T the line width is mainly governed by inhomogeneities of the external magnetic field. In this, so-called, regime of extreme narrowing further increase in temperature does not affect the line width and Li jump rates almost equal quadrupolar splitting frequencies. The latter results in vanishing of the EFG contributions to the line shape. Fully developed motional narrowing curves enable simulation of the motional narrowing curve using different approaches [36, 37]. The obtained datasets are best described by the Abragam relationship:

$$\Delta\nu(T) = \sqrt{\Delta\nu_{RL}^2 \tfrac{2}{\pi} \arctan\left[\varsigma \Delta\nu(T) \tau_0^{MN} exp\left(\tfrac{E_{a,A}}{k_B T}\right)\right]^{-1} + \Delta\nu_{inf}^2}$$

Here, ς is considered a fitting parameter, k_B is an acronym for the Boltzmann constant and τ_0^{MN} denotes the pre-exponential factor of the corresponding correlation time. Conducting a fit according to this relationship yields an activation energy $E_{a,A}$ of 0.13 eV, a value almost identical to the one obtained from spin-lattice relaxation rates (R_1). Compared to the other members of the LLZO family, $E_{a,A}$ can be ranked in an ascending order Ga-LLZO > Al-LLZO > LLZTO > tetragonal LLZO.

^{7}*Li spin-lattice relaxation*

To better understand Li^+ diffusion mechanisms indicated by previously presented data, diffusion-induced ^{7}Li NMR spin-lattice relaxation rates (R_1) were recorded over a wide temperature range at $\omega_0/2\pi$ = 116 MHz. Magnetization transients (M_z) acquired during these experiments can be well described by exponential functions. To obtain better results, stretched exponential functions were employed and yield stretching factors (γ) between 0.94 and 1. Characteristic relaxation times τ can be extracted from the transients and inverted to attain the rates plotted in Fig. 3a. These rates follow uncorrelated 3D motion that is best described by a model established by Bloembergen, Purcell and Pound (BPP) in 1948. For such three-dimensional diffusion processes, the model predicts β-values close to 2 and obeys the relationship $R_1 \propto \omega_0^{-\beta}$. The frequency ω_0, which can be directly derived from the Larmor frequency, is connected to the mean correlation rate $1/\tau_c$ in direct proportionality ($\omega_0\tau_c \approx 1$). Equality of the mean correlation rate and the mean Li^+ jump rate, $1/\tau$, within a factor of 2, enables calculation of the latter. This relation only applies at the maximum of the rate peak, therefore, ion jump rates can only be derived at a certain temperature. Here, the calculation yields a rate in the order of $7.3 \times 10^8\ s^{-1}$ at 493 K. At the low-T flank of said rate peak, a regime where $\omega_0\tau_c \gg 1$ applies, an

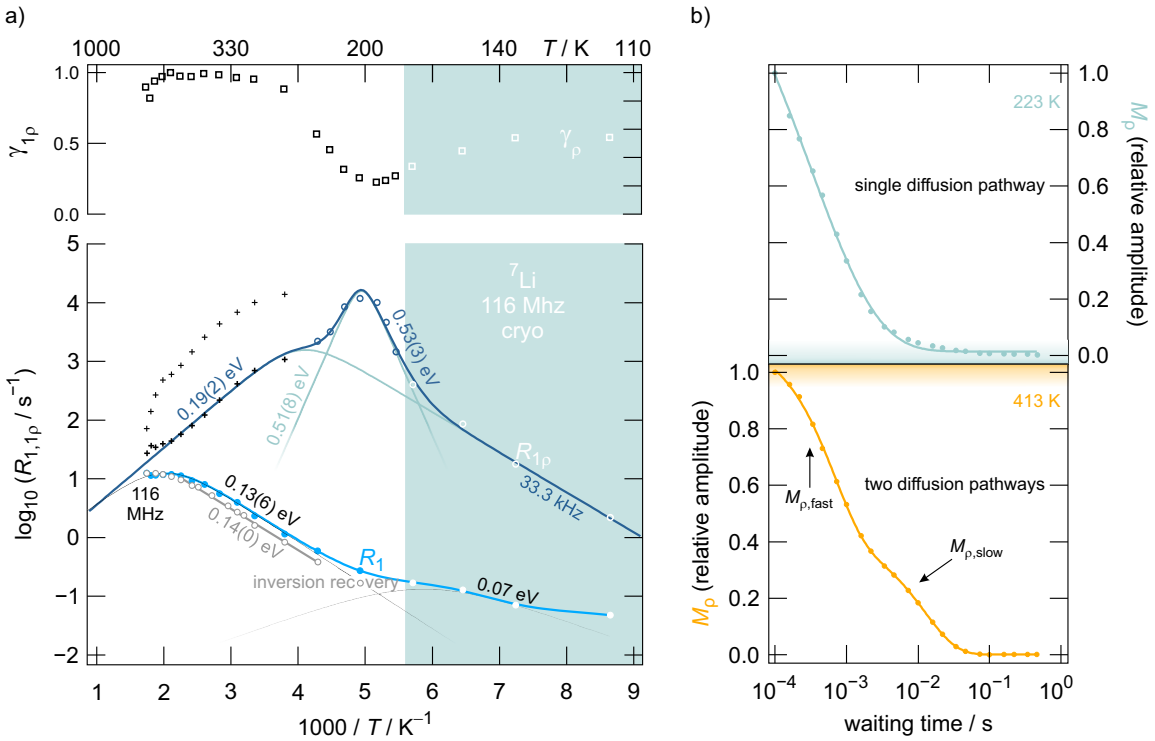

Figure 3: ^{7}Li NMR spin-lattice relaxation measurements carried out in the laboratory (R_1) and rotating frame of reference ($R_{1\rho}$) at 116 MHz and 33.3 kHz, respectively. a) plots obtained rates against inverse temperature. Black crosses indicate double exponential fitting curves, whereas blue and white circles are derived from single exponential curves. The BPP model is employed for both techniques. Aqua background denotes measurements in a cryogenic regime. b) depicts magnetization decay (M_ρ) in the rotating frame of reference. Data in the upper part is best described by single exponential decay, whereas the lower part needs an additional exponential function to be fitted sufficiently. $M_{\rho,\mathrm{fast}}$ and $M_{\rho,\mathrm{slow}}$ indicate two simultaneously happening diffusion processes.

activation energy $E_{a,NMR}$ of 0.13(6) eV of the underlying ion jump process can be derived. This energy barrier mainly describes local Li ion hopping between neighboring energetically inequivalent lattice sites. At much lower temperatures, the model reveals another ion hopping process that can be assigned to very fast motion between almost identical lattice sites. Its activation energy is, therefore, negligibly low exhibiting a barrier of only 0.07 eV. Energy barriers in this order of magnitude usually origin from weaker than activated backgrounds, in this case, *au contraire*, a local maximum at around 170 K can be detected. Inversion recovery experiments confirm rates acquired by saturation recovery pulse sequence. Obtained data are almost identical to R_1 rates and exhibit similar activation energy, both facts suggest observation of the same Li hopping process. At significantly lower frequencies, viz., in the kHz range, slower Li dynamics are sensed by the so-called spin-lock technique. Here, a locking frequency of $\omega_1/2\pi = 33.3$ kHz is employed to resolve diffusion processes at comparatively low temperatures. The obtained transients, as seen in Fig.3b, are best described by stretched single exponential functions up to a temperature of 263 K. Exceeding this limit reveals an additional slow Li diffusion process that is indicated by an arrow and the letters $M_{\rho,slow}$ in the lower plot of Fig.3b. These transients exhibit a decay behavior similar to a blend of 2 stretched exponential functions. Regarding the amplitudes of the decay processes separately, a much larger amplitude can be obtained for $M_{\rho,slow}$. Stretching factors for $M_{\rho,fast}$ range from 0.94 to 1, while values for $M_{\rho,slow}$ fluctuate between 0.81 and 1. When executing calculations within these boundaries, we obtain the $R_{1\rho}$ rates plotted in Fig. 3a. Double exponentially processed data is indicated by black crosses, single exponential analogues are drawn as blue circles and white circles, respectively. These rates consist of 2 ion diffusion processes whose contributions can be perfectly separated from each other by applying the BPP model. A narrow symmetric peak, which exhibits a maximum at $T_{max} = 203$ K, catches the eye. According to $\omega_1\tau_c \approx 0.5$, a Li jump rate of $4.2 \times 10^5\,s^{-1}$ can be determined at T_{max}. Regarding the activation energies at the low-T flank $E_{a,low} = 0.53(3)$ eV and its high-T flank opponent $E_{a,high} = 0.51(8)$ eV, points towards a very fast uncorrelated Li diffusion process in the material. At higher T another diffusion process, with $T_{max} = 243$ K, becomes apparent. In stark contrast to its predecessor, this peak appears to be much broader. Calculating an activation energy of 0.19(2) eV at its high-T flank verifies this initial thought. A closer look at the BPP models used to describe the rates in the rotating frame of reference ($R_{1\rho}$) as well as the laboratory frame of reference (R_1) reveals convergence of both curves at very high temperatures. This leads to the assumption that the peak at $T_{max} = 243$ K, sensed by the spin-lock technique, corresponds to the same diffusion process as the peak obtained in the laboratory frame of reference at 493 K. Spin-lattice relaxation measurements confirm line shape results that already pointed towards a very fast solid ion conducting material.

Conductivity measurements

Figure 4a illustrates conductivity isotherms acquired from monocrystalline Ga-stabilized LLZO in a frequency range of 0.01 Hz to 10^7 Hz. Frequency independent plateaus that shift towards higher frequencies can be detected. Their visibility turns out to be best between 173 K and 333 K. These plateaus enable determination of direct current ionic conductivity σ_{DC}, viz., $1.1 \times 10^{-3}\,S\,cm^{-1}$ at 293 K. After passing the plateau region, towards low-T, isotherms enter a dispersive region that can be well described by the Jonscher power law [38, 39]. According to the relation between plateau and dispersive region, this model describes the dimensionality of the ionic diffusion by the parameter p. Typical values for 3D motion, as introduced earlier by the BPP model, range between 0.6 and 0.8. Fitting of 2 isotherms with said model, depicted as red lines in Fig. 4a, both yield p-values of 0.64 for 173 K and 193 K, respectively. Dispersive regions of these isotherms indicate correlated

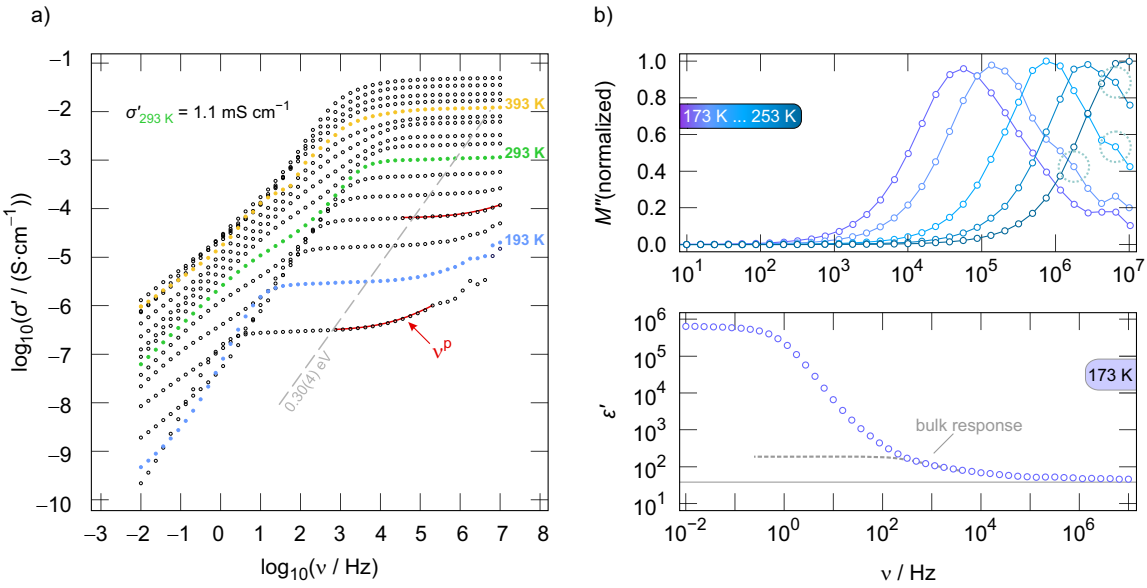

Figure 4: AC conductivity measurements of Ga-stabilized LLZO at oscillating potential V_{rms} = 100 mV. a) shows conductivity isotherms at temperatures from 173 K to 473 K. An overall conductivity of 1.1 mS cm^{-1}is obtained at 293 K. Red lines indicate Jonscher-type modeling. The upper graph of b) plots the electric modulus (M″) against the frequency (ν). Dotted circles point to a second diffusion process shifted towards high frequencies. The lower part of b) depicts one permittivity isotherm at 173 K. The bulk response is highlighted by dashed lines.

ion hopping and time-scale dependent ion dynamics. Regarding differences in energy barriers sensed by NMR and conductivity measurements, observation of ionic motion significantly depends on the time frame. Nonetheless, compared to previously published data on Al-stabilized LLZO, we obtain weaker dispersive regions at much lower temperatures. At temperatures below 233 K, Li ions most likably sense a heterogeneous potential landscape and undergo forward-backward jump processes. These ionic motions, as detected by conductivity measurements, purely consist of bulk ion dynamics, which is confirmed by the permittivity isotherm at 173 K in Figure 4b. Here, ϵ' values around 50, at frequencies approaching 0, clearly point towards bulk ion dynamics. Normalized data of the electric modulus is plotted in the upper graph of Fig. 4b. In perfect agreement with NMR rates, the acquired modulus data verify two diffusion processes that merge with increasing temperature. The second process, which is shifted to higher frequencies, is indicated by dashed circles.

Capacitances calculated from the complex plane plot at 193 K, seen in Fig. 5a, corroborate absence of grain boundary contributions and are highly feasible for single crystalline materials. These graphs plot the real part of the impedance (Z') against its imaginary antagonist ($-Z''$). Dispersive regions, as seen in Fig. 4a, tend to compress the shape of the obtained semi-circles. To gather more information and enhance visibility of these semi-circles, data are fitted using an equivalent circuit that features a resistance (R) shunt in parallel to a constant phase element (CPE) and depicted in solid orange lines. At its apex, for which $\omega_{apex} = 1/RC$ holds, the corresponding frequency is indirectly proportional to resistance R and capacitance C. An R value of 621 kΩ is determined at its intercept with the abscissa. The capacitance values were calculated using the relation $C = (R^{1-n}CPE)^{1/n}$,in which n is the fitting value that indicates the deviation from an ideal behavior. This yields

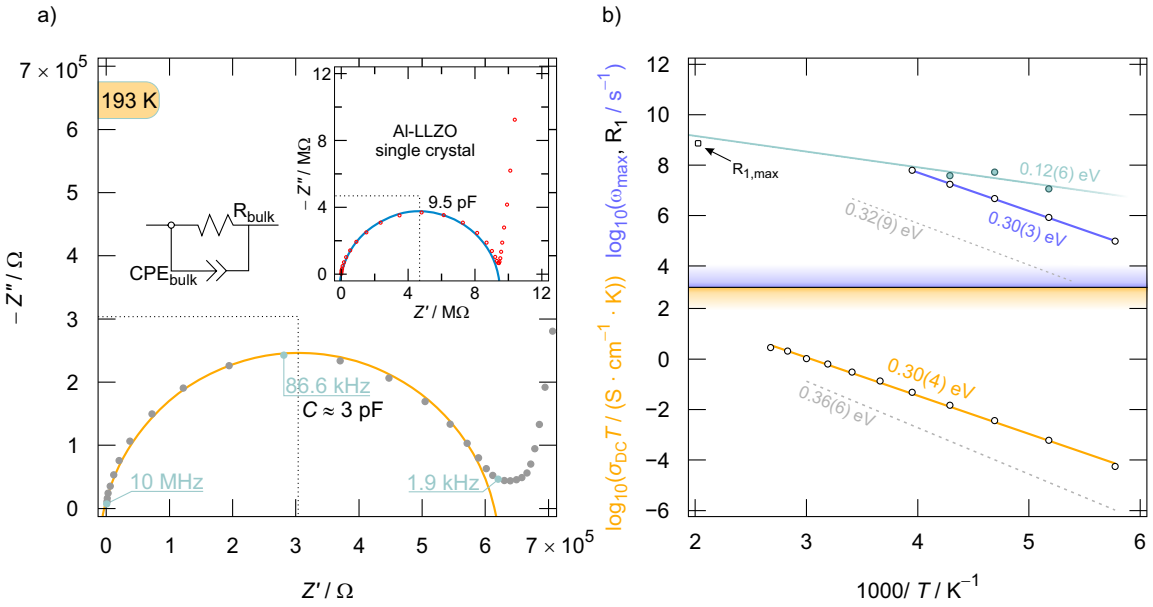

Figure 5: a) complex plane plot obtained from a Ga-stabilized LLZO single crystal at 193 K. Aqua-colored dots indicate characteristic frequencies of the bulk response. Simulation of a depressed semi-circle, shown as orange colored solid lines, is carried out with a resistance (R_{bulk}) shunt in parallel to a constant-phase element (CPE_{bulk}) and yield a capacitance of 3 pF. The insert in the upper right corner is deduced from monocrystalline Al-substituted LLZO at the same temperature. Simulations yield 9.5 pF at the apex of the depressed semi-circle. b) compares σ_{DC} values, derived from the isotherm plateaus, to ω_{max} calculated from the maxima of the modulus graph in Fig. 4b. Orange, blue and aqua colored solid lines represent linear fits. The aqua colored dots are derived from the second process seen in the modulus datasets. The proximity to the black square (R_{max}) indicates their origin from the same process.

a capacitance of 3 pF, which is typical for a bulk process and similar with the value published for its single crystalline Al^{3+}-stabilized analog (single-crystalline(sc) Al-LLZO; see inset Fig. 5a). Compared to monocrystalline Al-LLZO, the obtained conductivities for Ga-stabilized LLZO single crystals differ by more than one order of magnitude and, therefore, indicate superiority of the present sample over its Al-substituted analog.

Figure 5b plots σ_{DC} and ω_{max} ($= 2\pi \times \nu_{\mathrm{max}}$) against the inverse temperature. A linear fit is executed on both datasets in order to calculate the activation energy from their slopes. Results indicate similar activation energy for $E_{\mathrm{a,DC}}$= 0.30(4) eV and $E_{\mathrm{a,M}}$= 0.30(3) eV. Compared sc Al-LLZO (dashed lines), which exhibits a difference in activation energy between σ_{DC} and ω_{max}, the charge carrier density (N) in monocrystalline Ga-bearing LLZO does not vary with temperature. Apart from this fact, obtained $E_{\mathrm{a,DC}}$values largely differ from $E_{\mathrm{a,high}}$ acquired at the high-T flank of spin-lock NMR rates. We assume this difference to origin from long-ranged diffusion processes that conductivity measurements are sensitive to. Here, $E_{\mathrm{a,high}}$ is calculated for one diffusion process that is sensed almost independently from the other one, whereas $E_{\mathrm{a,DC}}$ can only give an overview of both diffusion processes in coexistence. Aqua colored dots in the modulus part of the graph are obtained from the second process in the modulus spectra. These processes are marked with dotted circles in Fig. 4b, and their maxima are transferred to this graph to enhance comparability. The employed linear fit, which yields an activation energy of 0.12(6) eV, is extrapolated to high temperatures. At 493 K

the line approaches the value of the Li^+ jump rate transferred from the R_1 maximum sensed by NMR. We consider this vital evidence for observation of the same local Li motion using two different techniques.

Influence of substituents on ion dynamics

Figure 6a represents a comparison of spin-lock relaxation rates obtained from 3 different single crystals. Regarding the shape of the rate peaks, potential landscapes for Li motion do not differ significantly in all three samples. Addressing the role of the substituent, substitution on the garnet Li-ion sublattice yields higher Li^+ mobility, compared to the substitution of Zr^{4+} by supervalent cations. This can be seen at first glance by the peak maxima shifts towards lower temperatures. Rates acquired from a Ta-substituted LLZO garnet peak at 288 K, which is slightly higher than 270 K obtained for Al-bearing garnet. A remarkable difference between those 2 materials is the significant reduction in activation energy at the high-T flank.

Here, Al-LLZO generates a vacancy-rich conduction path along its 24*d* and 96*h* lattice sites and, thus, yields much lower activation energy. As shown in the previous chapters, Ga-LLZO is capable of setting a new benchmark and exhibits an activation energy of 0.19(2) eV at its high-T flank. Such low activation energies for medium-ranged ion transport can be achieved by formation of an acentric cubic structure. In this material ion hopping between $12a - 48e - 12b$ sites leads to much faster ion dynamics. This is not only indicated by lowered activation energy of Li diffusion, but also by significant shift of rate maximum. T_{max} of the investigated sample can be located at 237 K, notably, this sample exhibits 2 diffusion pathways that are both sensed by spin-lock NMR in the kHz range. Similar findings are also observed for the Al-substituted LLZO garnet. Even though there is only one process shown in Fig. 6a, contributions of another Li pathway can be detected at higher temperatures. We consider this evidence for blocking of diffusion pathways by the dopant materials. Simulations performed in the recent past corroborate this theory [40].

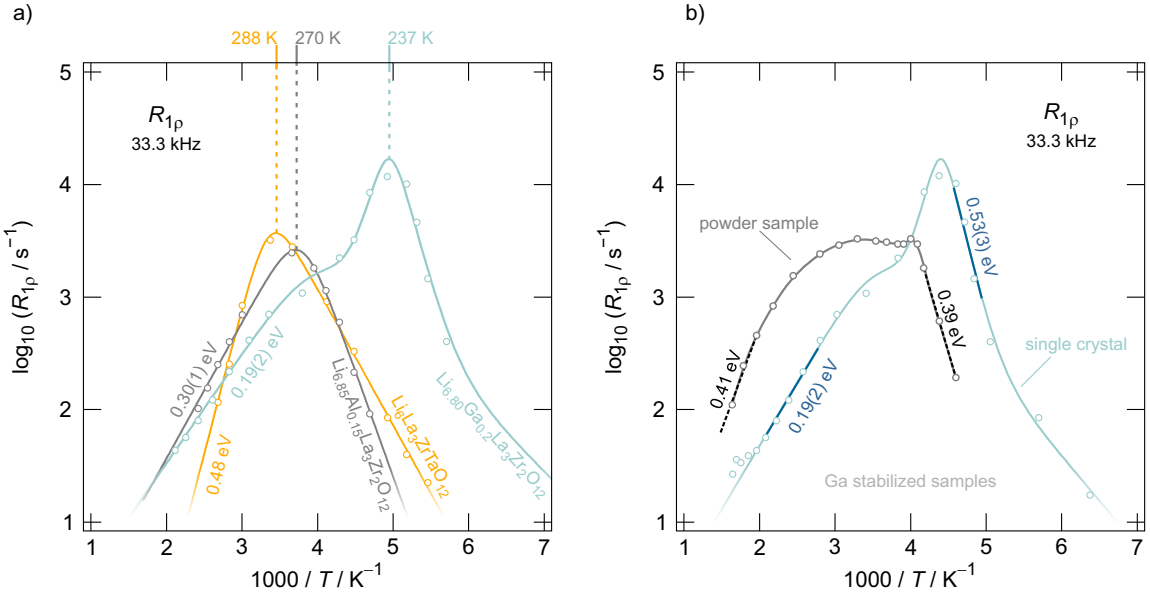

Figure 6: NMR $R_{1\rho}$ rates obtained for garnet-type LLZO at a spin-lock frequency of 33.3 kHz. Solid lines correspond to fits generated by the BPP model. Activation energies are derived directly from the fit and denoted in eV. a) compares Al, Ta and Ga-stabilized LLZO single crystals. b) points out differences between polycrystalline and single crystalline Ga-doped LLZO samples.

Figure 6b compares $R_{1\rho}$ rates obtained for monocrystalline Ga-doped LLZO with others acquired from a polycrystalline sample. Even though the powder sample exhibits a local maximum towards lower temperatures, the overall appearance of the rates is broadened throughout the whole temperature range and shifted to higher temperatures. Here, the local maximum can be assigned to the rate maximum obtained for our sample. The broad hump observed towards high T in the polycrystalline sample can be explained by (I) superposition of the slower hopping process inside the material and (II) influence of grain boundaries on the overall diffusion. Regarding the latter option and taken into account that Ga will, at least to some extent, block Li diffusion pathways, a combination of both cases is theoretically feasible. The difference in E_a at the high-T flank confirms an enormous difference in diffusivity.

IV. Conclusion

To provide deeper understanding of the fundamental hopping processes in garnet-type LLZO materials is considered the key to enable tailor-made garnet solid electrolytes. Inhomogeneities in polycrystalline samples render general statements on ion dynamics in such samples a highly difficult task. Here, we employed conductivity measurements and ^{7}Li NMR spectroscopy to gather information on diffusion properties of Czochralski-grown $Ga_{0.2}Li_{6.54}La_{2.92}Zr_2O_{11.95}$. This implies observation of bulk properties only and, therefore, results in better resolution of the underlying ionic motion processes. Long-ranged conductivity yields an overall activation energy of 0.3 eV and is in good agreement with data acquired from the electric modulus. Additionally, the latter also senses fast forward-backward ion motions, activated when exceeding 0.12 eV, that correspond to NMR rates in the laboratory frame of reference. Medium-ranged spin-lattice relaxation measurements, on the other hand, reveal 2 diffusion pathways in this single crystalline material. The first one is activated at temperatures as low as 203 K and senses a high energy barrier of 0.51 eV in both, its high-T and low-T, regimes. The second one requires a much lower activation energy of 0.19 eV and exhibits a local maximum at 243 K. To further proceed with the assignment of these results to diffusion pathways, simulations will be carried out in the future.

References

[1] J. Firnkorn, M. Müller, *Business Strategy and the Environment* **2012**, *21*, 264–280.

[2] H. U. Rashid Khan, M. Siddique, K. Zaman, S. U. Yousaf, A. M. Shoukry, S. Gani, Sasmoko, A. Khan, S. S. Hishan, H. Saleem, *Journal of Air Transport Management* **2018**, *70*, 18–35.

[3] T. Lieven, *Transportation Research Part A: Policy and Practice* **2015**, *82*, 78–93.

[4] N. Rietmann, T. Lieven, *Journal of Cleaner Production* **2019**, *206*, 66–75.

[5] Z. P. Cano, D. Banham, S. Ye, A. Hintennach, J. Lu, M. Fowler, Z. Chen, *Nature Energy* **2018**, *3*, 279–289.

[6] F. Larsson, P. Andersson, B.-E. Mellander, *Systems Perspectives on Electromobility* **2014**, 34–48.

[7] N. Mancini, J. S. M. Mardall, J. Kopitz, C. R. O'Donnell, D. Hanks, H. Li, OPTIMAL SOURCE ELECTRIC VEHICLE HEAT PUMP WITH EXTREME TEMPERATURE HEATING CAPABILITY AND EFFICIENT THERMAL PRECONDITIONING, US2019070924, **2019**.

[8] G. Kano, A. Horai, K. Arihara, H. Satou, Y. Ohsawa, R. Senbokuya, M. Chumon, E. Minegishi, SECONDARY BATTERY AND SECONDARY BATTERY CONTROL METHOD (WO2018158955), **2018**.

[9] J. M. Tarascon, *Philosophical Transactions of the Royal Society A: Mathematical Physical and Engineering Sciences* **2010**, *368*, 3227–3241.

[10] J. Janek, W. G. Zeier, *Nature Energy* **2016**, *1*, 1–4.

[11] T. Minami, A. Hayashi, M. Tatsumisago, *Solid State Ionics* **2006**, *177*, 2715–2720.

[12] L. Porcarelli, C. Gerbaldi, F. Bella, J. R. Nair, *Scientific Reports* **2016**, *6*, 1–14.

[13] N. Kamaya, K. Homma, Y. Yamakawa, M. Hirayama, R. Kanno, M. Yonemura, T. Kamiyama, Y. Kato, S. Hama, K. Kawamoto, A. Mitsui, *Nature Materials* **2011**, *10*, 682.

[14] J. B. Goodenough, Y. Kim, *Chemistry of Materials* **2010**, *22*, 587–603.

[15] F. Han, Y. Zhu, X. He, Y. Mo, C. Wang, *Advanced Energy Materials* **2016**, *6*, 1–9.

[16] R. Murugan, V. Thangadurai, W. Weppner, *Angewandte Chemie - International Edition* **2007**, *46*, 7778–7781.

[17] J. Awaka, N. Kijima, H. Hayakawa, J. Akimoto, *Journal of Solid State Chemistry* **2009**, *182*, 2046–2052.

[18] J. Awaka, A. Takashima, H. Hayakawa, N. Kijima, Y. Idemoto, J. Akimoto, *Key Engineering Materials* **2011**, *485*, 99–102.

[19] R. Wagner, G. J. Redhammer, D. Rettenwander, A. Senyshyn, W. Schmidt, M. Wilkening, G. Amthauer, *Chemistry of Materials* **2016**, *28*, 1861–1871.

[20] C. A. Geiger, E. Alekseev, B. Lazic, M. Fisch, T. Armbruster, R. Langner, M. Fechtelkord, N. Kim, T. Pettke, W. Weppner, *Inorganic Chemistry* **2011**, *50*, 1089–1097.

[21] H. Buschmann, J. Dölle, S. Berendts, A. Kuhn, P. Bottke, M. Wilkening, P. Heitjans, A. Senyshyn, H. Ehrenberg, A. Lotnyk, V. Duppel, L. Kienle, J. Janek, *Physical Chemistry Chemical Physics* **2011**, *13*, 19378–19392.

[22] E. Rangasamy, J. Wolfenstine, J. Sakamoto, *Solid State Ionics* **2012**, *206*, 28–32.

[23] M. Kotobuki, K. Kanamura, Y. Sato, T. Yoshida, *Journal of Power Sources* **2011**, *196*, 7750–7754.

[24] Y. Li, J. T. Han, C. A. Wang, S. C. Vogel, H. Xie, M. Xu, J. B. Goodenough, *Journal of Power Sources* **2012**, *209*, 278–281.

[25] Y. Jin, P. J. McGinn, "Al-doped Li7La3Zr2O12 synthesized by a polymerized complex method", **2011**.

[26] J. Wolfenstine, J. Ratchford, E. Rangasamy, J. Sakamoto, J. L. Allen, *Materials Chemistry and Physics* **2012**, *134*, 571–575.

[27] D. Rettenwander, P. Blaha, R. Laskowski, K. Schwarz, P. Bottke, M. Wilkening, C. A. Geiger, G. Amthauer, *Chemistry of Materials* **2014**, *26*, 2617–2623.

[28] D. Rettenwander, G. Redhammer, F. Preishuber-Pflügl, L. Cheng, L. Miara, R. Wagner, A. Welzl, E. Suard, M. M. Doeff, M. Wilkening, J. Fleig, G. Amthauer, *Chemistry of Materials* **2016**, *28*, 2384–2392.

[29] A. Wachter-Welzl, J. Kirowitz, R. Wagner, S. Smetaczek, G. C. Brunauer, M. Bonta, D. Rettenwander, S. Taibl, A. Limbeck, G. Amthauer, J. Fleig, *Solid State Ionics* **2018**, *319*, 203–208.

[30] S. Smetaczek, A. Wachter-Welzl, R. Wagner, D. Rettenwander, G. Amthauer, L. Andrejs, S. Taibl, A. Limbeck, J. Fleig, *Journal of Materials Chemistry A* **2019**, *7*, 6818–6831.

[31] E Fukushima, S. B. W. Roeder, *Experimental pulse NMR: a nuts and bolts approach*, Addison-Wesley Pub. Co., Advanced Book Program, **1981**.

[32] D. Ailion, C. P. Slichter, *Physical Review Letters* **1964**, *12*, 168–171.

[33] C. P. Slichter, D. Ailion, *Physical Review* **1964**, *135*, A1099–A1110.

[34] D. C. Ailion, C. P. Slichter, *Physical Review* **1965**, *137*, A235–A245.

[35] J. L. Allen, J. Wolfenstine, E. Rangasamy, J. Sakamoto, *Journal of Power Sources* **2012**, *206*, 315–319.

[36] J. Hendrickson, P. Bray, *Journal of Magnetic Resonance (1969)* **1973**, *9*, 341–357.

[37] J.-M. Abragam, Anatole; Winter, *Comptes Rendus de l'Academie des Sciences - Serie III* **1959**, *249*, 1633–1634.

[38] A. K. Jonscher, *Physica Status Solidi (a)* **1975**, *32*, 665–676.

[39] A. K. Jonscher, *Nature* **1977**, *267*, 673–679.

[40] F. A. García Daza, M. R. Bonilla, A. Llordés, J. Carrasco, E. Akhmatskaya, *ACS Applied Materials & Interfaces* **2019**, *11*, 753–765.

4.2 Phase Formation in Chemically Sodiated Spinel-Type $Li_4Ti_5O_{12}$

Li-ion battery systems comprising spinel-type $Li_4Ti_5O_{12}$ (LTO) anode materials are nowadays well established and commercially available. Application of LTO as high voltage anode ($\approx 1.55\,V$ vs. Li/Li^+) results in enhanced durability of non-aqueous liquid electrolyte systems. Furthermore, its negligible lattice expansion during lithium insertion (lithiation) and de-lithiation extends the battery lifetime to more than 10,000 cycles and, additionally, provides a stable system that can handle high cycling rates. Literature provides deeper insights into the lithiation process that is best described by the formation of a solid solution intermediate from spinel $Li_4Ti_5O_{12}$ to rock-salt $Li_7Ti_5O_{12}$ structure. In Na-ion systems, however, reports specified a three phase sodium insertion (sodiation) process.

This manuscript provides better understanding of the phase formation process in commercial spinel-type LTO samples from SüdChemie AG that were chemically sodiated using 1 M biphenyl−1,2−dimethoxyethane. Specific sodium insertion amounts, viz., given in mol Na per mol LTO and referred to as $x = 0.1$, 0.5 and 1.5, enable accurate determination of changes in ^{7}Li and ^{23}Na

ion mobility that are resolved by spin-lattice relaxation NMR. Close observation of ^{7}Li dynamics reveal that Li mobility steadily increases until $x_{\mathrm{Na}} = 0.5$ and subsequently decreases at higher sodiation ratios. The lack of evidence to underpin a multi-phase process suggests the formation of a solid solution that accommodates both Li and Na ions. In addition to this solid solution, the partial formation of the $Li_{4+x}Ti_5O_{12}$ solid solution, *i.e.*, also observed in lithiated LTO, largely contributes to Li ion dynamics.

Phase Formation in Chemically Sodiated Spinel-Type $Li_4Ti_5O_{12}$ Sensed by Solid-State NMR

Patrick Posch,[a*] Sarah Lunghammer,[a] H. Martin R. Wilkening[a‡]

[a]Institute for Chemistry and Technology of Materials, Christian Doppler Laboratory for Lithium Batteries, Graz University of Technology (NAWI Graz), Graz, Austria

[*]p.posch@tugraz.at
[‡]see also for correspondence: wilkening@tugraz.at

Abstract

Spinel-type $Li_4Ti_5O_{12}$ (LTO) is considered a promising anode material for sodium-ion battery application. During discharge, the intercalation of Na ions intiates a complex three-phase mechanism that leads to volume expansion. Starting from the surface of the material, Na occupies 16*c* sites. Hence, Li ions, residing on 8*a* lattice sites, move towards inner regions to form $Li_4Ti_5O_{12}$. We performed solid-state ^{7}Li and ^{23}Na NMR to closely investigate diffusion properties of these nuclei. Our results suggest the formation of a solid solution interphase between Na-rich and pristine LTO phases. Compositional changes of this solid solution, initiated by the growth of a Na-rich phase, have a significant impact on the overall Li diffusivity. High sodium insertion quantities result in the formation of solid solutions with moderate Li mobility. The formation is accompanied by disappearance of pristine LTO. To further elucidate this mechanism, ^{6}Li magic angle spinning NMR was employed. We were able to resolve the contribution of each crystallographic Li site to the overall Li diffusivity. Li residing on 16*c* sites in Na-rich LTO increasingly contribute to the overall diffusivity, whereas Li mobility between 8*a* and 16*c* sites slows down. Considering Na dynamics, ^{23}Na spin-lattice relaxation NMR senses two differently activated diffusion pathways at elevated temperatures.

Keywords: NMR, sodiation, LTO, solid solution, phase formation

I. Introduction

Rechargeable energy storage devices increase their impact on our economy day by day [1–3]. Lithium batteries offer a large field of application that stretches from miniature devices to electric transport [4–7]. Gradual exhaustion of lithium resources gives motive to speculate on the replacement of this charge carrier. A highly abundant, and therefore low-cost alternative would be sodium. Since early research stages, lithium and sodium storage devices were investigated in parallel until the commercialization of the first lithium ion battery by Sony in 1991 [8, 9]. Recent reports state that sodium batteries become more and more popular in the research community [10, 11].

Most reports focus on cathode materials, like Na_xCoO_2 or $Na_3V_2(PO_4)_3$/C, while very little research aims at anode materials [12–14]. Established anode materials like hard carbon and $Na_2Ti_3O_7$ suffer from low insertion potentials and therefore raise the risk of sodium plating at the electrode surface [15–17]. Well known from lithium battery application and most famous for its zero-strain properties, $Li_4Ti_5O_{12}$ entered the spotlight as promising

anode material several years ago [18–20].

Spinel-type LTO crystallizes in the $Fd\bar{3}m$ space group, in which the lithium ions occupy 16*d* octahedral and 8*a* tetrahedral sites. According to the Wyckoff notation, the general formula is given as $[Li]_{8a}[Li_{1/3}Ti_{5/3}]_{16d}[O_4]_{32e}$ locating lithium atoms at 8*a* and 16*d* sites. During lithium insertion, Li ions residing at 8*a* sites move to the initially vacant 16*c* sites and form rock-salt coordinated LTO $[Li_2]_{16c}[Li_{1/3}Ti_{5/3}]_{16d}[O_4]_{32e}$ [21, 22].

Upon sodiation, first reports suggest a multi-step insertion of sodium in the spinel structure; developing a sodium-rich $Na_6LiTi_5O_{12}$ phase and simultaneously enriching the lithium phase with excess lithium. According to Sun *et al.*, this process leads to the formation of rock-salt LTO, and a sodium-rich $[Na_2]_{16c}[Li_{1/3}Ti_{5/3}]_{16d}[O_4]_{32e}$ phase. It is stated that the occupation of the formerly vacant 16*c* sites is accompanied by a shift of Li from 8*a* to 16*c* sites and therefore leaving vacant 8*a* sites [23, 24]. Later on, *in situ* X-ray diffraction points towards the formation of a solid solution rather than establishing a network of three coexisting phases [25]. Moreover, transmission electron microscopy (TEM) investigations of sodiated polycrystalline and single-crystalline LTO do not only prove coexistence of the aforementioned phases but also reveal sodium-phase growth from the material surface to the inner region. Lattice disorder, measuring approx. 15 Å in width, can be observed along the interface of the two-phase system leading to local strains, dislocations or defects [26]. Latest research points towards the formation of a sodium-poor phase, $[Na]_{8a}[Li_{1/3}Ti_{5/3}]_{16d}[O_4]_{32e}$, which is formed at intermediate to high Na-extraction rates between 1 and 10 C. Due to small volume changes between sodium-poor and sodium-rich phase, purification of this phase is expected to enable strain-free cycling of LTO in sodium-ion batteries [27].

Here, we shed light on the sodium insertion mechanism in spinel-type LTO. Hence, a series of chemically sodiated samples ($x = 0.1, 0.3$ and 1.5) were prepared. To distinguish between multi-phase and solid solution mechanism, spin-lattice relaxation NMR is employed for ^{7}Li and ^{23}Na nuclei. To achieve better understanding of the ion dynamics, relaxation measurements are carried out in the laboratory and rotating frame of reference.

II. Methods

Preparation

Polycrystalline $Li_4Ti_5O_{12}$ (LTO), EXM 1037 purchased from SüdChemie AG, was mechanochemically treated to reduce the grain size of the initially microcrystalline powder. To obtain nanocrystalline powder, high-energy ball milling was performed using multiple zirconia balls with a diameter of 4 mm in a ZrO_2 beaker in a Fritsch Pulverisette 7 planetary mill. Milling was carried out in ethanol at rotational speeds of 600 RPM for 200 minutes. The powder was dried at ambient conditions before stripping Li_2CO_3 residues from the particles at 573 K under vacuum. Further handling of the material was carried out in an Ar-filled glovebox (MBraun MB-G 200) at inert atmosphere.

Chemical Sodiation

Dimethoxyethane (DME), supplied by Fluka Chemicals, was mixed with Biphenyl in stoichiometric amounts to yield 1M biphenyl$-1,2-$dimethoxyethane. To form a dark blue sodiating agent, $\approx$2.3 g sodium metal were added to 100 mL of the aforementioned 1M biphenyl-DME solution. LTO was immersed into the solution at a specific molar ratio to obtain different insertion states. Calculated ratios were 0.1:1, 0.5:1 and 1.5:1 mol Na per mol LTO, furthermore referred to as $x = 0.1, 0.5$ and 1.5. The higher the sodium content the more titanium gets reduced, which results in darkening of the blue color. The sodiation was carried out by stirring LTO in reducing medium for several hours. Unless the sodiating agent is used in excess, the completion of the sodiation process is indicated by color fading of the reagent. To remove all reagent residues, the sodiated

powder was washed 3 times with DME and afterwards dried in vacuum for 24 hours.

Nuclear Magnetic Resonance

Sodiated LTO samples were fire-sealed in quartz NMR tubes (NORELL SEPR250S) with a length of approximately 2 cm. Quartz wool was used to center the powder sample in the tube and prevent the sample from heating during the sealing process.

NMR spectroscopy was performed using an Avance III spectrometer coupled with an Ultrashield 500 MHz WB magnet at a nominal field of 11.7 T. The magnetic field was tuned to Larmor frequencies of $\omega_0/2\pi = 194$ and 132 MHz for ^{7}Li and ^{23}Na, respectively. A ceramic probe head was used to perform ^{7}Li measurements. Sodium measurements, which cannot be performed properly with ceramic probe heads, were carried out with a teflon probe head. At constant power output of 200 W, $\pi/2$ pulse lengths vary with temperature in a range from 2 to 4.8 μs for ^{7}Li and 2.2 to 2.9 μs for ^{23}Na. ^{23}Na and ^{7}Li spin-lattice relaxation rates, $1/T_1$ were acquired by saturation recovery experiments. The well-known saturation recovery pulse sequence, $10 \times \pi/2 - t_d - \pi/2 -$ acquisition (acq.), set with a time delay (t_d) five times longer than T_1 is executed [28]. Additionally, spin-lock spin-lattice relaxation NMR measurements were performed to investigate the temperature dependence of $1/T_{1\rho}$. This technique, $\pi/2$ p(t_{lock}) – acq., features a variable spin-lock pulse and was introduced by Ailion and Slichter in 1964 [29–31]. To ensure comparability, the spin-locking frequency, ν_{lock}, was set to 33.3 kHz for all experiments.

^{6}Li magic angle spinning (MAS) was carried out using a 2.5 mm probe head (Bruker) and employ a spinning frequency of 30 kHz. 128 scans of a single pulse sequence were recorded to accumulate 1D spectra. To ensure longitudinal relaxation of all components, recycle delays were set to 600 s. LiCl served as reference material to correct non material originated chemical shifts.

III. Results & Discussion

^{7}Li motional narrowing and line spectra

The first approach to study ionic diffusivity via NMR is to analyze temperature-variable line spectra. For this purpose, investigation of the ^{7}Li nucleus (spin-quantum number $I = {}^3/_2$) is of great advantage. At temperatures well below ambient, the central transition of the spin $^3/_2$ nucleus is only governed by dipolar interactions. At such temperatures, often called the rigid lattice regime (δ_{rl}), diffusion of Li ions is too slow to affect the overall line width. As the temperature is gradually raised, dipolar interactions between the spins average and result in narrowing of the central line. It can be observed that this effect, referred to as motional narrowing (MN), sets in at a specific temperature called the onset temperature. At high T, the narrowing process is finished and the line width solely represents the inhomogeneity of the applied static magnetic field. The inflection point of the MN curve, defined as exactly half the difference of δ_{rl} and complete narrowing, can be used to estimate the lithium jump rate (τ^{-1}) according to the equation $\tau^{-1} = \delta_{rl} \times 2\pi$. Figure 1a shows motional narrowing curves obtained for samples at several sodiation states (x = 0, 0.1, 0.5 and 1.5). It can be seen that δ_{rl} values of the samples 0 and 0.1 are almost identical. LTO structures bearing higher amounts of sodium, viz., x = 0.5 and 1.5, exhibit an increased central line width in the rigid lattice regime. According to the relation between τ^-1 and δ_{rl}, jump rates of $3.1 \times 10^4 s^{-1}$ can be calculated at the inflection points of samples sodiated with 0 and 0.1 mol Na. Insertion of sodium into the LTO structure exceeding amounts of x = 0.1 broaden the line in the rigid lattice regime and, therefore, lead to an increased Li jumping rate of $\approx 3.7 \times 10^4\, s^{-1}$. This increase in line width can either be caused by paramagnetic interaction between Ti^{3+} centers and Li spins, or decrease in Li–Li distance. The latter originates from movement of Li from 8*a* to 16*c* sites, and as a consequence thereof, increasing dipolar interaction between the particular ions [32]. As shown by Schmidt *et al.*,

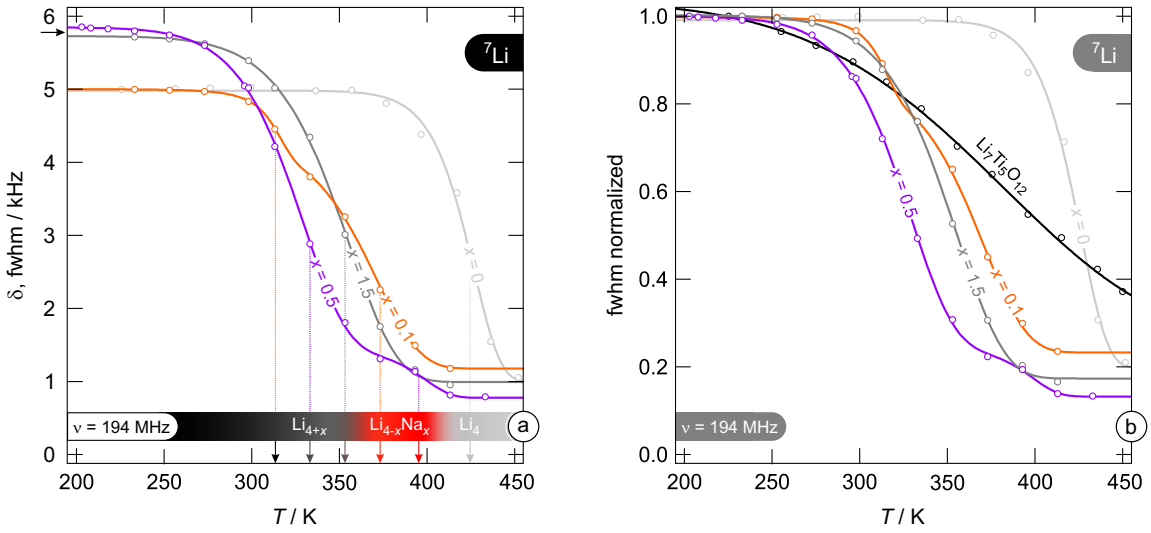

Figure 1: ^{7}Li NMR motional narrowing of sodiated $Na_xLi_{4-x}Ti_5O_{12}$ samples, viz., x = 0.1, 0.5 and 1.5, compared to unsodiated $Li_4Ti_5O_{12}$. a) plots the fwhm in kHz against the temperature in K and exhibits differences in rigid lattice line width. b) depicts normalized line widths to enhance comparability of the different samples.

these effects broaden the line to about 23 kHz when the material is fully converted to rock-salt LTO, *i.e.*, insertion of 3 mol Li per mol LTO. As known from previous reports, the sodium-rich phase, $[Na_2]_{16c}[Li_{1/3}Ti_{5/3}]_{16d}[O_4]_{32e}$, stretches the lattice and leads to volume expansion. We assume that this expansion increases the distance between neighboring 16*c* Li ions, resulting in narrowing of the line in the rigid lattice regime. Most notably, this effect is observed when exceeding x = 0.5 Na in the LTO structure (indicated by an arrow in Fig.1a). It verifies the formation of a sodium-rich phase with larger lattice constants, viz., a = 8.69 Å opposed to a = 8.35 Å, as suggested by Kitta *et al.* [27]. Interesting changes in motional narrowing behavior are displayed in Fig. 1b. Normalizing the line width enhances the comparability among the different samples and greatly accentuates the temperature shift of the inflection points. It can be clearly seen that the MN curves shift towards lower temperatures, indicating increased Li diffusivity, when increasing the sodiation ratio. However, exceeding an insertion amount of x = 0.5 reverses this behavior, resulting in a backward shift towards x = 0. Inconsistency in motional narrowing, predominantly observable at low sodium insertion states, indicates contribution of a second phase to the overall Li diffusion. We assign this process to Li motion in a $Na_xLi_{4-x}Ti_5O_{12}$ solid solution bearing small amounts of Na. Considering growth of the sodiated LTO phase from the surface to the center of particles, the formation of lithiated phase is limited to the ions leaving 8a sites. This mechanism comprises two options (I) the formation of a lithiated LTO solid solution core, and (II) a sodium containing solid solution $Na_xLi_{4-x}Ti_5O_{12}$ forming an outer shell that slowly replaces all Li and turns to $Na_6LiTi_5O_{12}$. Interpreting the changes in motional narrowing behavior from x = 0.1 to x = 0.5, a combination of both options fits the scheme. Therefore, the low to moderate T part of the MN curves can be ascribed to sparsely lithiated $Li_{4+x}Ti_5O_{12}$ solid solution that enables much faster ion diffusion. Further increase in sodium content to 1.5 mol entails disappearance of the additional diffusion pathway. We consider this vital evidence for fading of the combined solid solution $Na_xLi_{4-x}Ti_5O_{12}$, and decrease in overall diffusivity is explained by moderate to low

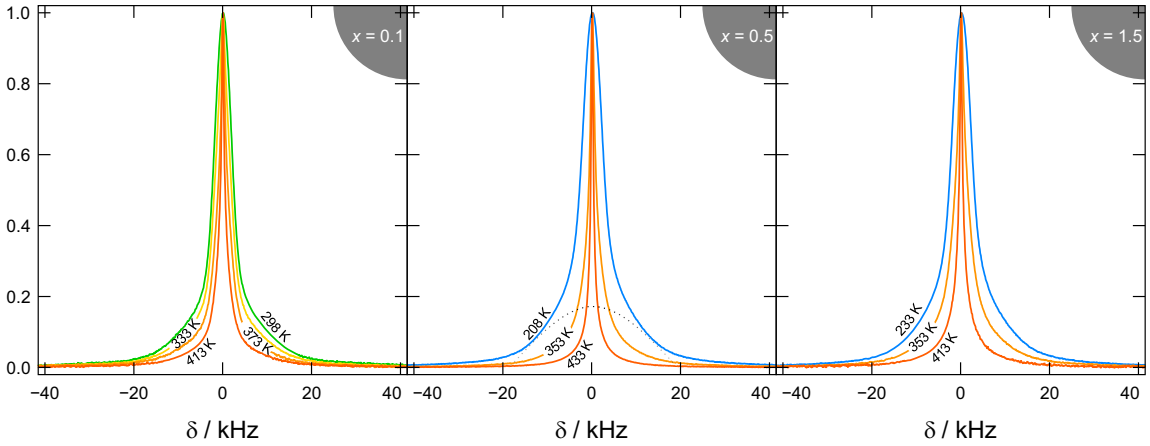

Figure 2: Line spectra acquired from ^{7}Li NMR experiments at different sodiation states, namely, x = 0.1, 0.5 and 1.5. Each part consists of lines in the rigid lattice regime, a fully narrowed line and characteristic temperatures inbetween those regimes. The quadrupolar powder pattern is indicated by dotted lines in x = 0.5. Experiment temperatures are given next to the lines in black color. All lines are normalized for comparison reasons.

Li motion in highly lithiated LTO. In addition to shift of the MN curves, line narrowing over a wide temperature range of said curves can be monitored. This change in narrowing behavior is strongly pronounced at x = 0.5, in which the full narrowing of the central transition spans from 230 K to 420 K. This behavior is a strong indication for the coexistence of several Li diffusion pathways and, therefore, a wide distribution of energy barriers inside the material. A stepwise activation of diffusion processes is known to cause such narrowing behavior. Interestingly, this stretching is reduced when inserting more Na ions into the lattice, as for x = 1.5 the effect diminishes. Therefore, we assume less pathways are involved in the Li diffusion process at high intercalation states, which was already suggested by Sun *et al.* [23]. Figure 2 compares the line widths of the rigid lattice, intermediate states and fully narrowed lines for all three samples. A closer look at the temperatures for fully narrowed and rigid lattice lines implies that line narrowing happens over a much wider temperature range in x = 0.5. This effect is caused by the coexistence of highly mobile Li in $Li_{4+x}Ti_5O_{12}$ solid solution and less mobile Li in $Na_xLi_{4-x}Ti_5O_{12}$. A noteworthy detail is the less pronounced quadrupolar powder pattern that is usually caused by interaction of the quadrupole moment of ^{7}Li spins with a non-vanishing electric field gradient. This is in stark contrast to the findings for lithiated LTO, which exhibits much more pronounced quadrupolar powder patterns at low T throughout the measurement series from x = 0.1 to x = 3 [32].

^{6}*Li magic angle spinning NMR*

A comparison between lithium mobility in sodiated and lithiated LTO is drawn by 1D ^{6}Li MAS NMR and graphically portrayed in Figure 3. Pure spinel $Li_4Ti_5O_{12}$ was thoroughly investigated in the past and is displayed on top of the graph for comparison reasons [33]. Figure 3a depicts changes in line-shape and shift of the lines at various lithiation states, viz., x_{Li} = 0.1, 0.3 and 1, that are used as reference materials to determine differences in diffusion behavior [34]. Paying close attention to the shift of line closest to 0 ppm, defined as $Li_{8a(16c)}$, is necessary to understand the phase growth mechanism of the sodiated phase. Upon lithiation, such a shift is assigned to either Li insertion into Li_2TiO_3 or interaction with this superficial amorphous phase. In stark contrast to lithiated LTO, sodiated systems omit

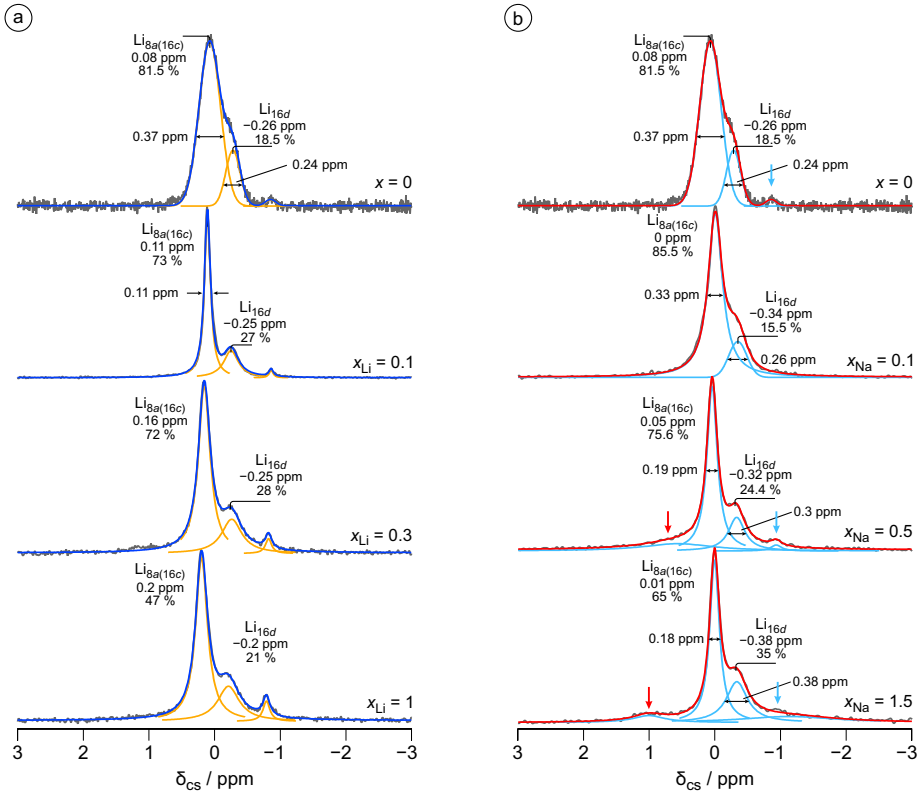

Figure 3: ^{6}Li MAS spectra of treated LTO acquired at 30 kHz spinning frequency and a constant temperature of 303 K. a) displays published data acquired after chemical insertion of Li that serve as reference. b) depicts lines with ascending sodium content, in which blue arrows indicate the Li_2TiO_3 side phase and red arrows point towards Li^+ occupation of the 16*d* lattice site in $Na_xLi_{4-x}Ti_5O_{12}$.

these interactions and exhibit no shift of the $Li_{8a(16c)}$ line with ascending sodium content. Additionally, the initial peak of said phase at a chemical shift (δ_{CS}) of -0.87 ppm, indicated by blue arrows in Fig. 3, decreases in intensity with rising x_{Na}. On the other hand, ascending lithium contents, as seen in x_{Li} = 0.1, 0.3 and 1, lead to its intensification and to growing shifts of the central transition. To evaluate Li diffusivity from line widths is vital to distinguish between simultaneously occurring processes in different phases. Regarding the line widths of the 8*a*(16*c*) transition, rising sodium contents expose an increase in Li diffusivity. Observation of the same transition at various lithiation states reveal significant differences in phase formation. Opposed to steep decrease in line width from 0.37 ppm to 0.11 ppm at x_{Li} = 0.1, uniform line narrowing occurs during sodium insertion. Rock-salt $Li_7Ti_5O_{12}$ contributions at shifts ≈ -11 ppm cannot be observed in sodiated samples with $x_{Na} \leq 1.5$. All facts point towards partial formation of a fast $Li_{4+x}Ti_5O_{12}$ solid solution with an additional sodium containing $Na_xLi_{4-x}Ti_5O_{12}$ phase that lowers overall diffusivity of the Li ions. We assign the additional peak, which is observable at positive shifts when exceeding x_{Na} = 0.5 and indicated by red arrows, to Li residing at 16*d* sites of sodium-rich $Na_xLi_{4-x}Ti_5O_{12}$. Growth of said peak with increasing sodium content facilitates the assignment process.

^{7}Li and ^{23}Na spin-lattice relaxation NMR

^{7}Li spin-lattice relaxation measurements of LTO with Na insertion amounts from x = 0.1 to x = 1.5, performed at a Larmor frequency

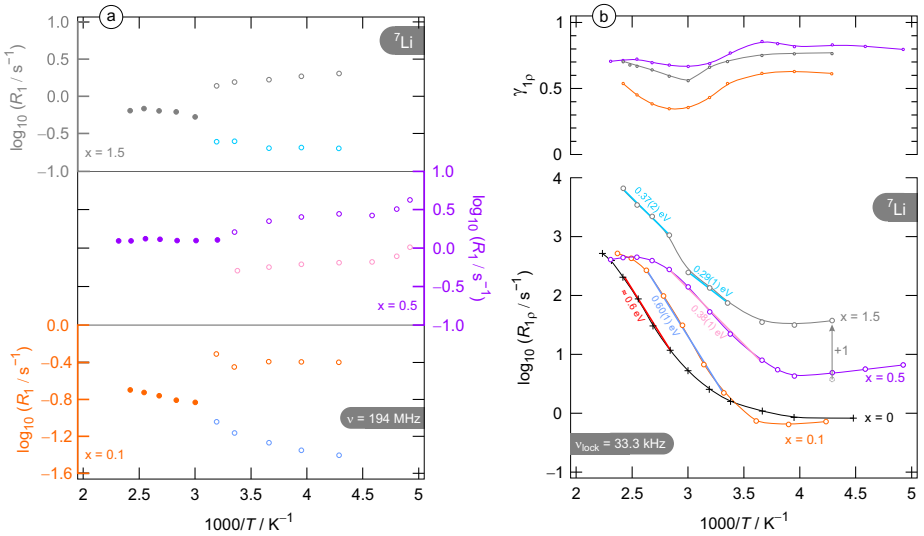

Figure 4: ^{7}Li spin-lattice relaxation NMR of $Na_xLi_{4-x}Ti_5O_{12}$ after chemical sodiation to x = 0.1, 0.5, 1.5. a) depicts local relaxation rates acquired in the laboratory frame of reference at a Larmor frequency of 194 MHz. Circles indicate data from transients best described by double exponential decay. b) sheds light on medium ranged dynamics of the same samples at a locking frequency 33.3 kHz. Activation energies are determined by the slope of linear datapoints at the low-T flank, *i.e.*, best described by $\omega_1\tau_c \gg 0.5$.

of 194 MHz, reveal paramagnetic relaxation behavior according to Curie–Weiss [35]. Figure 4a draws a comparison between the different $1/T_1$ rates, furthermore referred to as R_1 rates, for each sample.

Similar to motional narrowing, coupling of Li spins with the Ti^{3+} centers affect the values of R_1. Therefore, rates are significantly increased from x = 0.1 to x = 0.5, whereas further sodiation to x = 1.5 leads to a slight decrease of the obtained R_1 rates. These observations are in good agreement with the ones found in the rigid lattice regime for the same samples. In addition, rates at moderate to low T shed light on the phase segregation of $Li_4Ti_5O_{12}$ and $Li_7Ti_5O_{12}$. As verified by neutron diffraction, phase separation starts at 250 K and becomes more pronounced at lower temperatures. Furthermore, said phases start to build up submicrometer sized domains [36]. The saturation recovery pulse sequence senses jump processes at such small ranges that phase segregation in these domains can be easily distinguished from solid solutions. A slight decrease in T, *i.e.*, below 293 K, entails a change in dynamics for all investigated samples. This change manifests in description of the transients by stretched double exponential functions. Hence, at least two phases take part in the Li diffusion process with one providing faster ion dynamics than the other. These data match the previously discussed motional narrowing results outstandingly well.

Compared to R_1, rates obtained from measurements in the rotating frame of reference, furthermore referred to as $R_{1\rho}$, detail ion dynamics at extended ranges. Hence, presence of multiple diffusion processes that exhibit different energy barriers will lead to a higher mean activation energy. The spin-lock technique is able to sense multiple domains simultaneously to yield diffusion characteristics of the solid solution throughout the temperature range of the measurement series. Therefore, activation energies resemble Li dynamics in solid solution. A closer look at Figure 4b reveals a drastic decrease in activation energy at the $R_{1\rho}$ low-T flank, *i.e.*, described by $\omega_1\tau_c \gg 0.5$, of the sam-

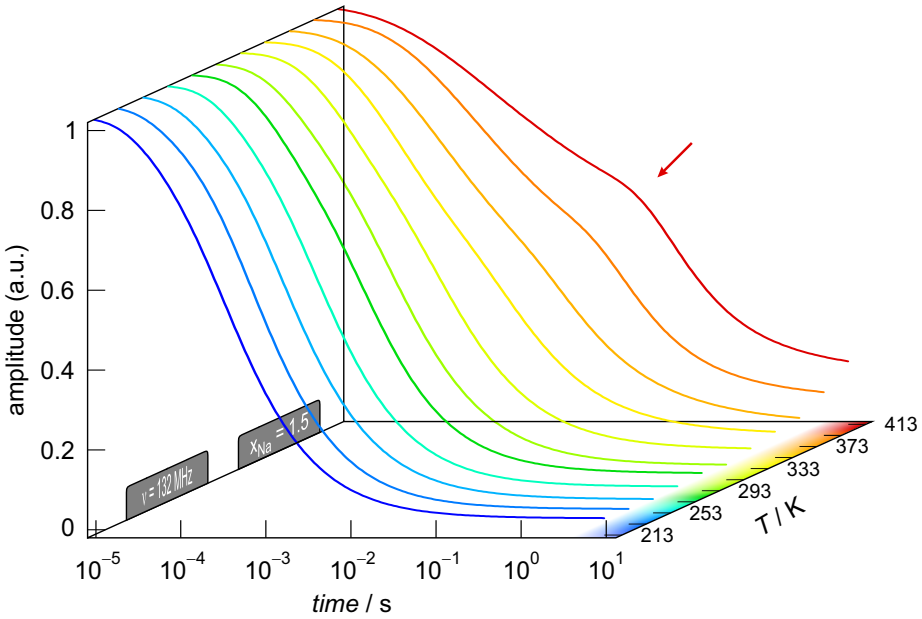

Figure 5: ^{23}Na relaxometry transients of sodiated LTO acquired in the laboratory frame of reference at a Larmor frequency of 132 MHz. This behavior occurs most prominently in $x = 1.5$, but is also silhouetted in $x = 0.5$. At temperatures above room temperature, enhanced Li mobility is detected in a second phase revealing a slower diffusion pathway.

ples $x = 0.1$ and $x = 0.5$. Values of 0.38 eV, as in $x = 0.5$, have already been assigned to lower energy barriers originating from formation of $Li_{4+x}Ti_5O_{12}$ solid solution [32]. In addition to the decrease in activation energy, a shift of the rate maximum can be observed. The rate maximum is defined as equilibrium of mean correlation rate ($1/\tau_c$), which is connected to the Li jump rate ($1/\tau$) by a factor of 2, and angular locking frequency (ω_1) and is best described by $\omega_1\tau_c \approx 0.5$. For measurements performed at $\nu = 33.3$ kHz, and hence $\omega_1 = 209.2$ kHz, a correlation rate of $4.2 \times 10^5 s^{-1}$ can be calculated. This correlation rate corresponds to a mean residence time of 2.4 μs for Li ions at the temperature of the rate maximum. Analogous to previously shown data, the rate maxima shift to lower temperatures until $x = 0.5$ and experience a shift in backward direction when exceeding this limit. Hence, a rate maximum at 393 K reveals fast Li dynamics in $x = 0.5$, rate maxima of the other samples are shifted towards much higher T.

^{23}Na measurements of the same samples are solely carried out in the laboratory frame of reference at a Larmor frequency of 132 MHz. Transient data gathered from saturation recovery experiments point towards existence of two simultaneously occuring jump processes at elevated temperatures. Figure 5 depicts transients of $x = 1.5$ that are, after exceeding 293 K, well described by stretched double exponential functions. This behavior can be assigned to increased accessibility of crystallographic sites for Na motion at such temperatures. As shown in Figure 6a, the availability of these sites is correlated to the quantity of inserted sodium. R_1 rates obtained for insertion of low sodium amounts, as in $x = 0.1$, generates a solid solution in which Na exhibits limited mobility and transients can be sufficiently described by stretched single exponential curves. Even though Na mobility increases at elevated temperatures, this sample exhibits no diffusion-induced rate peak until 413 K. Contrary to the previously regarded sample, additional lattice sites become available for ion diffusion at an insertion state of $x = 0.5$. Temporary occupa-

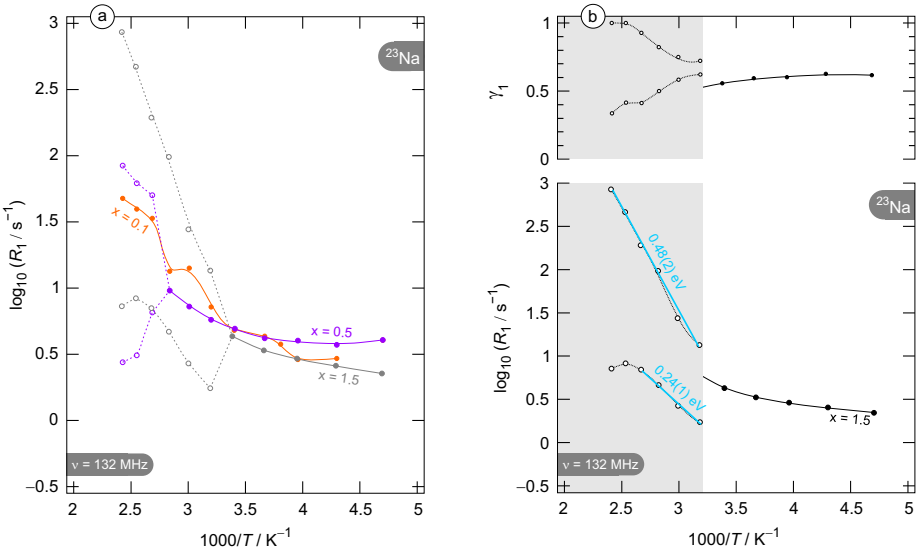

Figure 6: ^{23}Na ion dynamics as seen by NMR at a Larmor frequency of 132 MHz in the laboratory frame of reference. a) compares the rates acquired from sodiated LTO at x = 0.1, 0.5 and 1.5 and particularly emphasizing on simultaneous processes at high T. b) resolves these processes for x = 1.5 and depicts activation barriers for the fast and slow diffusion process, respectively.

tion of such sites is clearly visible at temperatures exceeding 353 K, hence, splitting of the single exponentially fitted data is depicted in the graph. Rates at x = 1.5, shown in Fig. 6b, bisect at 313 K and reveal the maximum and low-T flank of a diffusion-induced rate peak. The mean sodium residence time, which is obtained the peak maximum, equals 1.2 ns at 393 K. Its low-T flank reveals an activation barrier of 0.24 eV for this diffusion process. We assign this process to ionic motion between $8a - 16c - 8a'$ sites. In addition, the low-T flank of a slower hopping process discloses an activation energy of 0.48 eV and is sensed at much higher rates. This process can either be ascribed to exploiting of vacant 48f sites, which results in diffusion along an $8a - 48f - 8a'$ pathway, or hindered Na mobility in Li-rich $Na_xLi_{4-x}Ti_5O_{12}$ solid solution.

IV. Conclusion

LTO is widely known as zero-strain anode material for LiBs and a promising candidate for future application in sodium batteries. To elucidate its phase formation process is crucial to unleash its full potential in Na bearing systems. Here, we employed a variety of NMR spectroscopical methods to probe, both Li and Na, ion dynamics in chemically sodiated LTO. ^{7}Li line spectra reveal the influence of Na on Li mobility in a solid solution, *i.e.*, $Na_xLi_{4-x}Ti_5O_{12}$, at low sodium insertion states, viz., x = 0.1 and 0.5. Furthermore, motional narrowing confirms the formation of a solid solution $Li_{4+x}Ti_5O_{12}$ phase at x = 1.5. This behavior is supported by ^{7}Li spin-lattice relaxation in the laboratory and rotating frame of reference, both verifying the existence of two different diffusion processes. An $R_{1\rho}$ maximum can only be obtained for x = 0.5 at 393 K, confirming that Li ion motion decelerates at higher and lower sodium content. ^{6}Li MAS was used to resolve different contributions to the central transition obtained by ^{7}Li line measurements. Acquired data points towards slow and steady conversion to solid solution $Li_{4+x}Ti_5O_{12}$ and additionally reveals mobility of Li ions in $Na_xLi_{4-x}Ti_5O_{12}$ solid solution. A prerequisite for investigation of Na motion is the insertion of a reasonable amount of sodium into the LTO structure. At x =

1.5, ^{23}Na spin-lattice relaxation resolves two sodium diffusion processes at temperatures above 313 K that expose activation energies of 0.24 eV and 0.48 eV. These energy barriers can be assigned to Na motion in the aforementioned $Na_xLi_{4-x}Ti_5O_{12}$ solid solution. Variations in sodium and lithium content of said phase enable two possible diffusion pathways, viz., $8a - 16c - 8a'$ and $8a - 48f - 8a'$. To provide better understanding of sodium dynamics in this material, future investigations should aim at structural changes in desodiated LTO and the rearrangement of phases during cycling. Both characteristics are vital for application as anode material in future sodium ion batteries.

References

[1] P. G. Bruce, B. Scrosati, J.-M. Tarascon, *Angewandte Chemie International Edition* **2008**, *47*, 2930–2946.

[2] B. Dunn, H. Kamath, J.-M. Tarascon, *Science* **2011**, *334*, 928 LP –935.

[3] D Larcher, J.-M. Tarascon, *Nature Chemistry* **2014**, *7*, 19.

[4] H. Nishide, K. Oyaizu, *Science* **2008**, *319*, 737 LP –738.

[5] M Armand, J.-M. Tarascon, *Nature* **2008**, *451*, 652.

[6] M. Rawlence, I. Garbayo, S. Buecheler, J. L. Rupp, *Nanoscale* **2016**, *8*, 14746–14753.

[7] A. Fotouhi, D. J. Auger, K. Propp, S. Longo, M. Wild, *Renewable and Sustainable Energy Reviews* **2016**, *56*, 1008–1021.

[8] M. D. Slater, D. Kim, E. Lee, C. S. Johnson, *Advanced Functional Materials* **2012**, *23*, 947–958.

[9] T. Nagaura, K. Tozawa, *Progress in Batteries & Solar Cells* **1990**, *9*, 209–217.

[10] P. K. Nayak, L. Yang, W. Brehm, P. Adelhelm, *Angewandte Chemie International Edition* **2018**, *57*, 102–120.

[11] J. Peters, D. Buchholz, S. Passerini, M. Weil, *Energy & Environmental Science* **2016**, *9*, 1744–1751.

[12] Z. Jian, L. Zhao, H. Pan, Y.-S. Hu, H. Li, W. Chen, L. Chen, *Electrochemistry Communications* **2012**, *14*, 86–89.

[13] Y. Lei, X. Li, L. Liu, G. Ceder, *Chemistry of Materials* **2014**, *26*, 5288–5296.

[14] J. Yang, D. W. Han, M. R. Jo, K. Song, Y. I. Kim, S. L. Chou, H. K. Liu, Y. M. Kang, *Journal of Materials Chemistry A* **2015**, *3*, 1005–1009.

[15] D. A. Stevens, J. R. Dahn, *Journal of The Electrochemical Society* **2002**, *147*, 1271.

[16] H. Pan, X. Lu, X. Yu, Y.-S. Hu, H. Li, X.-Q. Yang, L. Chen, *Advanced Energy Materials* **2013**, *3*, 1186–1194.

[17] Z. Li, Z. Jian, X. Wang, I. A. Rodríguez-Pérez, C. Bommier, X. Ji, *Chemical Communications* **2017**, *53*, 2610–2613.

[18] T. Ohzuku, A. Ueda, N. Yamamoto, *Journal of The Electrochemical Society* **1995**, *142*, 1431.

[19] S. Scharner, W. Weppner, P. Schmid-Beurmann, *Journal of The Electrochemical Society* **1999**, *146*, 857.

[20] K Kanamura, T. Umegaki, H. Naito, Z. Takehara, T. Yao, *Journal of Applied Electrochemistry* **1998**, *31*, 73–78.

[21] K. Ariyoshi, R. Yamato, T. Ohzuku, *Electrochimica Acta* **2005**, *51*, 1125–1129.

[22] K. Ariyoshi, S. Yamamoto, T. Ohzuku, *Journal of Power Sources* **2003**, *119-121*, 959–963.

[23] Y. Sun, L. Zhao, H. Pan, X. Lu, L. Gu, Y. S. Hu, H. Li, M. Armand, Y. Ikuhara, L. Chen, X. Huang, *Nature Communications* **2013**, *4*, 1810–1870.

[24] L. Zhao, H. L. Pan, Y. S. Hu, H. Li, L. Q. Chen, *Chinese Physics B* **2012**, *21*, 4–8.

[25] X. Yu, H. Pan, W. Wan, C. Ma, J. Bai, Q. Meng, S. N. Ehrlich, Y. S. Hu, X. Q. Yang, *Nano Letters* **2013**, *13*, 4721–4727.

[26] M. Kitta, R. Kataoka, M. Kohyama, *Physical Chemistry Chemical Physics* **2016**, *18*, 19888–19893.

[27] M. Kitta, M. Kohyama, *Electrochemistry* **2018**, *86*, 194–197.

[28] E Fukushima, S. B. W. Roeder, *Experimental pulse NMR: a nuts and bolts approach*, Addison-Wesley Pub. Co., Advanced Book Program, **1981**.

[29] D. Ailion, C. P. Slichter, *Physical Review Letters* **1964**, *12*, 168–171.

[30] D. C. Ailion, C. P. Slichter, *Physical Review* **1965**, *137*, A235–A245.

[31] C. P. Slichter, D. Ailion, *Physical Review* **1964**, *135*, A1099–A1110.

[32] W. Schmidt, P. Bottke, M. Sternad, P. Gollob, V. Hennige, M. Wilkening, Small change-great effect: Steep increase of Li ion dynamics in Li4Ti5O12at the early stages of chemical Li insertion, **2015**.

[33] J. Kartha, D. Tunstall, J. T. Irvine, *Journal of Solid State Chemistry* **2000**, *152*, 397–402.

[34] W. Schmidt, M. Wilkening, *The Journal of Physical Chemistry C* **2016**, *120*, 11372–11381.

[35] N. Fujiwara, H. Yasuoka, Y. Ueda, *Physical Review B* **1998**, *57*, 3539–3542.

[36] M Wagemaker, D. R. Simon, E. M. Kelder, J Schoonman, C Ringpfeil, U Haake, D Lützenkirchen-Hecht, R Frahm, F. M. Mulder, *Advanced Materials* **2006**, *18*, 3169–3173.

4.3 Is Aluminum a Proper Anode Current Collector in Na-ion Batteries?

High availability and attractive prices render aluminum a desirable, cost-efficient, current collector material for Li-ion batteries. However, alloy formation in contact with lithium at voltages below 0.3 V, as well as severe corrosion effects initiated by fluorinated electrolytes, largely reduce its field of application in state of the art Li-ion batteries. In combination with high voltage anode materials or less corrosive electrolytes a reduction of these unwanted effects can be achieved, but also entails a decrease in energy density of the battery system. To circumvent aluminum related issues, copper is employed as anode current collector in commercially available Li-ion batteries. Sodium based battery systems, however, do not exhibit alloying reactions with aluminum and were, therefore, considered inherently compatible until several groups reported on corrosion of aluminum current collectors at voltages above 3.5 V.

This manuscript sheds light on the interaction of current collector material and cell performance. Sodium-ion half cells were assembled to perform electrochemical analysis, viz., cyclic voltrammetry and galvanostatic cycling, of various electrode materials on copper and aluminum substrates, respectively.

Significant reduction in performance of aluminum substrates equipped with TiO_2 active material were determined at high cycling rates. Initial assumptions implicated delamination of the active layer from the current collector and, therefore, contact loss. To substantiate these assumptions scanning electron microscopy (SEM) investigations were carried out and revealed the formation of an interlayer underneath the surface of the electrode material.

Is aluminum a proper anode current collector in Na-ion batteries?
Insights from several case studies

P. Posch[a*], M. Nachtnebel[b], H. Schroettner[b,c], H.M.R. Wilkening[a], I. Hanzu[a‡]

[a]Institute for Chemistry and Technology of Materials, Christian Doppler Laboratory for Lithium Batteries, Graz University of Technology (NAWI Graz), Graz, Austria

[b] Graz Centre for Electron Microscopy (ZFE), Steyrergasse 17, 8010 Graz, Austria

[c] Institute of Electron Microscopy and Nanoanalysis (FELMI), Graz University of Technology, Steyrergasse 17, 8010 Graz, Austria

*p.posch@tugraz.at

‡see also for correspondence: hanzu@tugraz.at

Abstract

The influence of current collectors on the overall cell performance is often considered negligible. Due to the inability of sodium to form alloys with aluminum, Na-ion batteries (SIBs) are, opposed to lithium based systems, regarded fully compatible with Al current collectors. Nonetheless, corrosion of aluminum substrates is known to occur at voltages exceeding 3.5 V, requiring either passivation agents or an effective potential limitation. Here, a comparison of several active materials, on copper and aluminum substrates, sheds light on systematic degradation of current collectors in SIBs. Electrochemical cycling experiments reveal severe capacity differences between TiO_2 composite electrodes that are operated with aluminum and copper current collectors, respectively. These differences are recorded primarily at high cycling rates, pointing towards delamination of active material from the aluminum substrate. Scanning electron microscopy is employed to acquire cross-section pictures of these very electrodes. Even though substrate containing layers are found in both TiO_2 electrodes, only aluminum derivatives damage the composite layer. These observations are in perfect agreement with data gathered from electrochemical characterization, and suggest Na blocking properties of the Al-rich layers at high currents.

Keywords: sodium ion battery, current collector, aluminum, stability

I. Introduction

Sustainable energy production from renewable resources are today in the focus of society needs and government policies. However, due to the intermittent character of renewable energy sources, efficient and cost effective energy storage is required. Lithium-ion technology has seen a tremendous evolution and development during the past two decades. Various devices, such as mobile phones, notebooks, tablets and electric vehicles carry batteries. Exhibiting high energy densities and outstanding cycle life, Li-ion batteries cover the most important requirements and are successfully used in these devices. Nonetheless, uncertainties in lithium supply and increasing lithium costs constitute one of major draw-

backs when large-scale grid-relevant storage is considered [1]. Thus, beyond lithium ion storage systems, for instance sodium-based, promise to be remarkable alternatives to cover large-scale grid applications. Since its invention, in 1966, the Na-S battery is recognized as a high capacity storage device [2]. Its drawbacks, inherent to a molten sodium anode and operating temperatures of $300 - 350\,^{\circ}\mathrm{C}$, can only be overcome by alternative systems that can be operated at room temperature (RT). Recently, Xiaofu *et al.* reported on such a system that uses a setup similar to lithium ion batteries and can be operated at RT providing capacities around $1\,\mathrm{Ah\,g^{-1}}$ after 150 cycles at 0.1 C [3]. Then, there are many instances of Na-ion batteries reported. In such a system, instead of shifting lithium ions between the positive and negative electrodes, sodium ions are used. While this results in lower energy densities for the Na-ion cells, the costs are estimated to be significantly lower than for Li-ion technology for reasons related to the better materials availability and lower materials costs.

A problem that is very often overlooked and not thoroughly investigated is the influence that the current collectors have on battery performance. In Li-ion systems, copper is used at the negative electrode (anode) and aluminum at the positive electrode (cathode). Aluminum current collectors at the anode cannot be used in Li-ion batteries. Severe corrosion effects in contact with fluorinated lithium salt electrolytes and alloying reactions with Li^+ at potentials below 0.3 V render aluminum unusable as anode current collector [4–7]. More advanced approaches make use of this behavior to generate lithium alloy electrodes [8–10] or reduce the problem by using less corrosive electrolytes and always in conjunction with high voltage anode materials such as $Li_4Ti_5O_{12}$ (LTO) [11–16], a strategy that reduces the energy density of the battery.

In the case of Na-ion systems, there is a significant departure from the Li-ion case. Since no alloying reaction takes place between sodium and aluminum current collectors, this system is considered inherently compatible and its application is expected to cut costs in sodium ion batteries [17, 18]. Several reports point to corrosion of aluminum current collectors at potentials above 3.5 V. Analogous to corrosion found in lithium cells, fluorinated sodium compounds can weaken this effect [19, 20].

Unfortunately, the stability of aluminum as negative current collector in Na-ion cells is, more often than not, only postulated instead of clearly proven. In most reports, Cu is still used as a current collector. Even if no Na-Al alloys are formed, there are other unwanted possible reactions that may affect the electrode performance. Is Al usable as a negative electrode current collector in Na-ion based cells without significant reduction of performance when compared to Cu? What are the drawbacks of the Al current collectors? This work provides a comparison between copper and aluminum current collectors and their interaction with active materials. Electrochemical performance is tested in sodium metal half-cells containing organic 1 M NaFSI electrolyte and data obtained from cyclic voltammetry and galvanostatic cycling is used to reveal differences in operation and performance.

II. Methods

Active Material Synthesis

$Na_3V_2(PO_4)_3/C$, furthermore referred to as NVP, was synthesized via sol-gel preparation route as reported by C. Huang *et alii* [21]. Citric acid (Sigma-Aldrich) and ammonium metavanadate (Sigma-Aldrich) in equimolar amounts were dissolved in distilled water forming an orange solution at 60 °C. An aqueous solution of sodium phosphate monobasic monohydrate (Sigma-Aldrich) was added continuously over the fixed period of 1 hour. The solution turned green and was heated to 80 °C under vigorous stirring for 2 hours to form a gel. The brightly blue colored gel was transferred to a heating oven and kept at 80 °C for one night. Before sintering the material at 700 °C in a tube furnace in argon atmosphere, the dry

gel is ground using mortar and pestle to obtain fine powder. The sintered material appears as a black powder.

Hard carbon, synthesized as reported by R. Alcántara *et al.*, also employs sol-gel method [22]. Resorcinol (Riedel-de-Haën) was dissolved in methanol stabilized formaldehyde (9-15 % methanol, Sigma-Aldrich) and aqueous sodium carbonate (Merck) was added to catalyze further reactions. Ortho-phosphoric acid (Roth, 85 %) was added dropwise to neutralize the solution, before stirring for 3 h and obtaining an aquagel. This gel was cured at 85 °C for 24 h and afterwards washed with large amounts of acetone for several times. A centrifuge (Heraeus, Megafuge 1.0) was used to separate gel from acetone after each washing step. The rinsed gel was heated to 300 °C for 2 h, ground using mortar and pestle, and sintered at 950 °C for 1 h in a quartz tube furnace in Ar atmosphere.

Composite electrodes were fabricated using active material, Super C65 carbon black and N-methylpyrrolidone (Sigma-Aldrich), in the case NVP, or sodium carboxymethylcellulose (Walocel CRT 2000 by Wolff Cellulosics GmbH & Co KG) binder dissolved in water (1.25 wt%) for hard carbon and TiO_2 active materials. The weight of all components was carefully determined to achieve a ratio of 12 : 2 : 1. Slurries were obtained by ball milling for 45 min at 400 RPM and a films with thicknesses of 100 μm were applied on aluminum and copper substrates using an ERICHSEN casting device. While roughened Cu foil (Coppertex) with a thickness of 30 μm was used without treatment, 50 μm Al (Goodfellow) foil was etched with an aqueous solution of 5 wt% KOH. Afterwards etched foils were rinsed with distilled water and dried using a heat gun. Cast electrodes were pre-dried at 1 atm and 60 °C for 8 hours and cut to 10 mm discs before the primary drying process at 60 °C under vacuum was carried out.

Electrochemical Characterization

Half-cell arrangements were assembled using Swagelok cells equipped with a composite working electrode, sodium metal (ACS reagent, Sigma-Aldrich) counter and reference electrode. Discs of Whatman GF/B glass microfiber filters act as separators that are wetted with 1 M NaFSI (Solvionic) in ethylene carbonate : diethylcarbonate (1:1 v/v) electrolyte. Cell assembly was performed under inert atmosphere, containing less than 1 ppm O_2 and 1 ppm H_2O, in an Mbraun Glovebox.

Cyclic voltammetry and galvanostatic cycling with potential limitation were carried out at an MPG-2 device from Biologic Science Instruments and a Maccor 40 primary cell testing device, respectively. Cyclic voltammograms were recorded from 0.1 to 3 V vs. Na/Na^+ executing sweep rates of 0.05, 0.1, 0.2, 0.5, 1, 2, 5, 10, 20 and 50 mV s^{-1}. Galvanostatic cycling experiments were set to the same potential limits and charging / discharging was performed at theoretically calculated C-rates. All electrochemical data were acquired at room temperature. The measurement devices ran EC-Lab and MacTest32 software, respectively, and both programs were used to process obtained datasets.

III. Results & Discussion

Corrosion of aluminum in various electrolyte media has been thoroughly investigated by several research groups [15, 23, 24]. Such effects are commonly determined by cyclic voltammetry over wide potential ranges. In the case of organic NaFSI-based electrolytes, potentials exceeding 3.5 V lead to corrosion of aluminum substrates. As shown by Otaegui *et al.*, corrosion kinetics accelerates at elevated temperatures; this can be overcome by substituting the organic solvent with an ionic liquid [25]. Here, we focus on possible interactions of substrates and composite active materials. Electrochemical analysis is carried out at potential ranges that are considered inherently safe, viz., between 0.1 and 3 V versus Na^+/Na. Figure 1 shows a comparison between the second CV cycles of six sodium metal half cells equipped with different working electrodes, namely TiO_2 nanoparticles (a), hard carbon (b) and NVP

(c), at a scan rate of 50 μV s^{-1}. Current collector materials are indicated by color, namely, orange and grey for copper and aluminum, respectively. These measurements provide initial insight into substrate based differences between the three electrode materials. TiO_2 samples exhibit negligible differences of the current response, there are no practican differences between copper and aluminum substrates. Slightly different electrochemical behaviour can be observed for hard carbon on copper substrate, compared to its analogue cast on aluminum. On aluminum substrate, NVP exhibits broad humps in oxidation and reduction regime at potentials ranging from 1 to 2.5 V when the Al current collector is used. The same redox processes show a pair of peaks, spaced in a range from 1.5 to 1.8 V, simply by changing the substrate material. This already points towards an initially poor electron transport/ poor contact between Al and the active NVP-containing mass leading to much higher ohmic drops in the electrode supported on Al. This limitation does not occur on Cu. At lower potentials, 0.1 to 0.5 V, another redox process that is only silhouetted on aluminum can be better resolved on copper substrate. These significant differences can be seen in Fig. 1c.

In the case of TiO_2 electrodes, measurements at slightly increased sweep rate confirm the cycling behavior seen at very low sweep rates. However, starting at 10 mV s^{-1}, there are significant differences between Al and Cu current collectors. Figure 2 shows performance differences at advancing sweep rates, viz. 1, 10 and 50 mV s^{-1}. The voltage profile at a sweep rate of 1 mV s^{-1} remains largely similar to lower scan rates (see Fig. 1a). At a sweep rate of 10 mV s^{-1}, multiple cathodic peak shoulders occur at 0.4, 0.75 and 1 V with their corresponding anodic peaks overlapping to form a very broad signal. These peak shoulders are less pronounced on aluminum substrate. The current response deviation at higher sweep rates, clearly visible at 10 and 50 mV s^{-1}, may arise from contact issues at the current collector electrode material interface. The absence of hysteresis loops, *i.e.*, a characteristic crossing of anodic and cathodic measurement data during corrosion at high potentials, verifies that corrosion of the aluminum current collectors, usually occurring above 3.5 V for aprotic NaFSI-containing electrolyte mixtures, is successfully prevented by the narrow potential range. Hence, all differences seen in the measurement data solely originate from interactions between electrolyte, active material and current collector. To evaluate the contribution of the active material to this phenomenon, galvanostatic cycling experiments were carried out. An overview of the obtained data is

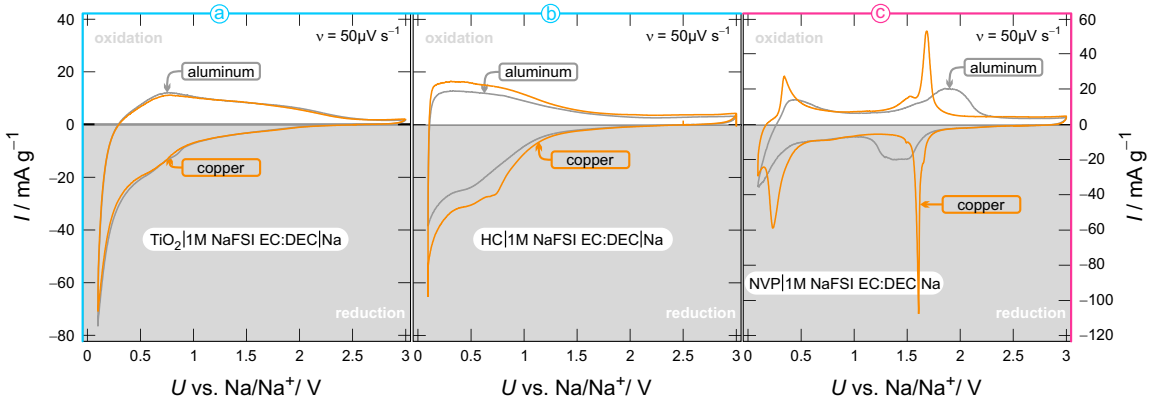

Figure 1: Cyclic voltammograms of TiO_2 nanoparticles (a), hard carbon (b) and $Na_3V_2(PO_4)_3$/C (c) electrodes in half-cell assembly, with sodium metal as both counter and reference electrodes. The electrolyte consists of 1 M NaFSI conductive salt dissolved in volumetrically mixed EC:DEC (1:1). All graphs contain data obtained during the second cycle.

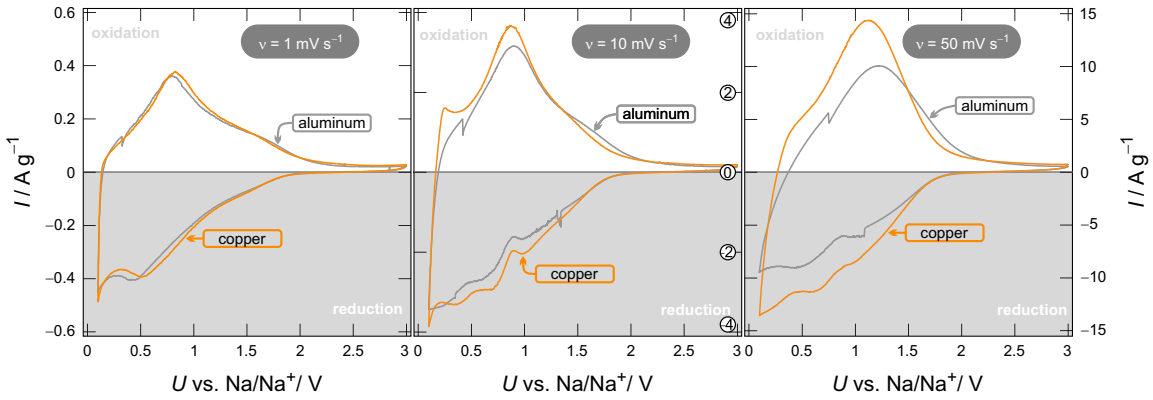

Figure 2: Cyclic voltammograms of TiO_2 nanoparticles on copper and aluminum substrates at advancing scan rates. Tick labels for graph acquired at ν= 10 mV s^{-1} are set in circles at the right-hand axis.

given in Figure 3, plotting the specific capacity against cycle number (a), as well as the coulombic efficiency of TiO_2 nanoparticles during cycling (b). To evaluate both mild and more demanding cycling conditions, the cycling rate is ramped from 0.1 C to 5 C in 5 steps, the cycling rate being increased every 20 cycles. Reversibility is determined by capacity recovery at the lowest cycling rate, namely 0.1 C, in end of the measurement series. Electrodes made with hard carbon active material, indicated by orange and dark grey dots for copper and aluminum, respectively, exhibit discharge specific capacities of 82 mAh g^{-1} at 0.1 C, independent of current collector material. This behavior maintains throughout the measurement series, even at high cycling rates. NVP adopts the same characteristics at slightly lower capacities of 53 mAh g^{-1}. However, at a cycling rate of 5 C, capacities depend on substrate material reaching 36 and 32 mAh g^{-1} on copper and aluminum, respectively. In contrast to cyclic voltammetry data, the cycling performance of NVP electrodes at moderate cycling rates is not affected by current collector material. Contrary to the aforementioned electrode materials, cyclability of TiO_2 nanoparticles is severely affected by its substrate. Specific discharge capacities of 139 and 136 mAh g^{-1} on aluminum and copper substrates, respectively, are obtained at slow cycling rates of 0.1 C. Raising the current to 1 C or more, a drastic decay of capacity can be registered on aluminum substrate. At a cycling rate of 5 C, electrodes on aluminum current collectors only reach 42 % of the capacity obtained with equivalent material on copper substrate. This difference is significant and cannot be ascribed to the somehow lower conductivity of Al with respect to the current collector. The interface contact between Al and active mass is the likely culprit.

A closer look at the coulombic efficiency of these data sets, see Fig. 3b, exposes advancing inconsistency from currents equivalent to 1 C. These findings suggest that delamination of the active material from its aluminum current collector is probably taking place. Therefore, less active material contributes to the cell reaction leading to loss of specific capacity. As a result of a slow delamination procedure, coulombic efficiencies remain reasonably high.

Wu *et al.* prove that these electrode materials, in particular anatase TiO_2 nanoparticles, are very stable anodes exhibiting no significant capacity decay [26]. To provide deeper understanding of the good cycle life, two additional titania morphologies, viz., rutile/anatase spherical microparticles and rod-shaped rutile nanoparticles, were investigated on both substrate materials. Figure 4 compares these two materials with the TiO_2 nanoparticles shown in Figure 3. Differences between copper and aluminum substrates arise for each material. Moderate capacity reduction with increasing

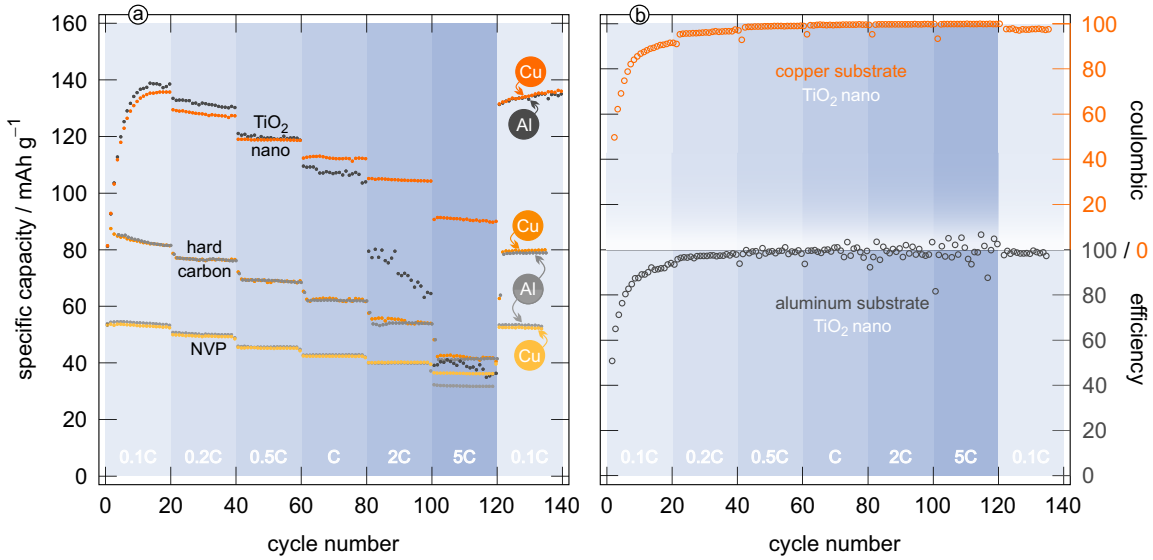

Figure 3: (a)Specific capacities of TiO_2, hard carbon and NVP in comparison. Half-cells assembled with sodium metal counter and reference electrodes and 1 M NaFSI EC:DEC electrolyte. Current steps advance 0.1 C, 0.2 C, 0.5 C, C, 2 C to 5 C and the last step is set back to 0.1 C. All materials exhibit outstanding recovery of initial capacities at lower cycling rates. Different substrate materials are distinguishable by colors, the corresponding substrate material is indicated by labeled circles in matching color. (b) Comparison of coulombic efficiencies for TiO_2 electrodes. Orange rings, as well as the corresponding scale, indicate the copper current collector, whereas the dark grey opponents illustrate their aluminum analogs.

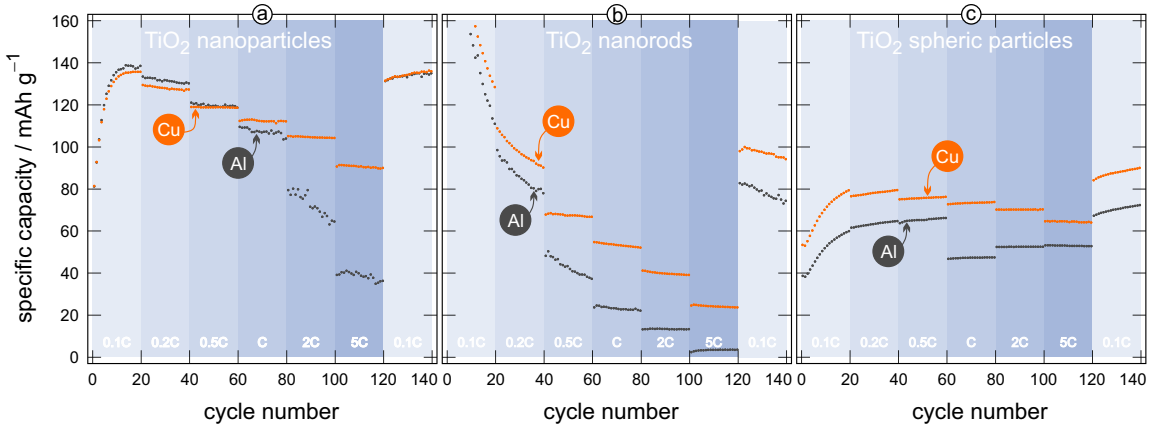

Figure 4: Performance of TiO_2 morphologies in sodium metal half-cells using 1 M NaFSI EC:DEC electrolyte. These three graphs plot the specific capacity against the cycle number. Aluminum and copper substrates are shown in different colors and are, furthermore, labeled with small circles that are either lettered Al or Cu. Cycling rates are highlighted by colored backgrounds and white inscriptions at the bottom of each graph.

cycling rate can be observed for spherical particles on copper substrate, as seen in Fig. 4a and c. As discussed above, this decay is intensified on aluminum substrate for nanoparticles seen in Fig. 4a. Electrodes composed of spherical TiO_2 microparticles experience an unknown process leading to a sudden decrease in capacity at currents equivalent to 1 C. This effect is only observed for electrodes on aluminum current collectors. The rod-shaped active material is prone to massive capacity decay starting at the first cycle, however, independently of substrate material. A characteristic effect observed for all three materials at low cycling rates is the recovery of the initial capacity ratio between copper and aluminum substrate electrodes. This supports the theory that electrodes on Al possibly experience higher interfacial resistance, manifesting at higher cycling rates, while the full capacity is recovered when lowering the current. This could also be due to the partial delamination of the active layer from the Al current collector.

Cross-section scanning electron microscopy (SEM) images acquired from a cycled, TiO_2 nanoparticle electrode on aluminum current collector seems to confirm this hypothesis (see Figure 5). An overall impression is given in Fig. 5a, showing $\approx 700\,\mu$m of the electrode construction. It reveals delamination from the aluminum current collector, and, as seen in the center of the picture, to some extent completely missing parts of active layer. Another noteworthy detail is the layer on the bottom that is entirely peeled off the electrode surface. We expect this peeling to happen during the slope-cutting process. Fig. 5b focusses at the interface between Al foil and active layer on a length of $130\,\mu$m. Delamination of the active material from the aluminum surface can be verified beyond doubt. Additionally, severe vertical fissure of the composite material, which is most likely caused by volumetric expansion and contraction during Na insertion and de-insertion, is observed. A close-up, see Fig. 5c, shows the formation of a layer between the current collector and the active material, as well as pole like structures. As verified by energy dispersive X-ray spectroscopy (EDX) analysis, these poles consist of aluminum oxide that pierces through the composite material and builds an interlayer. The built interlayer, illustrated in Fig. 5d, does not grow on the surface of the active layer, but is instead located beneath it. A careful look at EDX mapping reveals different compositions for the formed layer and the poles, which leads to the assumption that reactions with the electrolyte take place. Detection of fluorine and

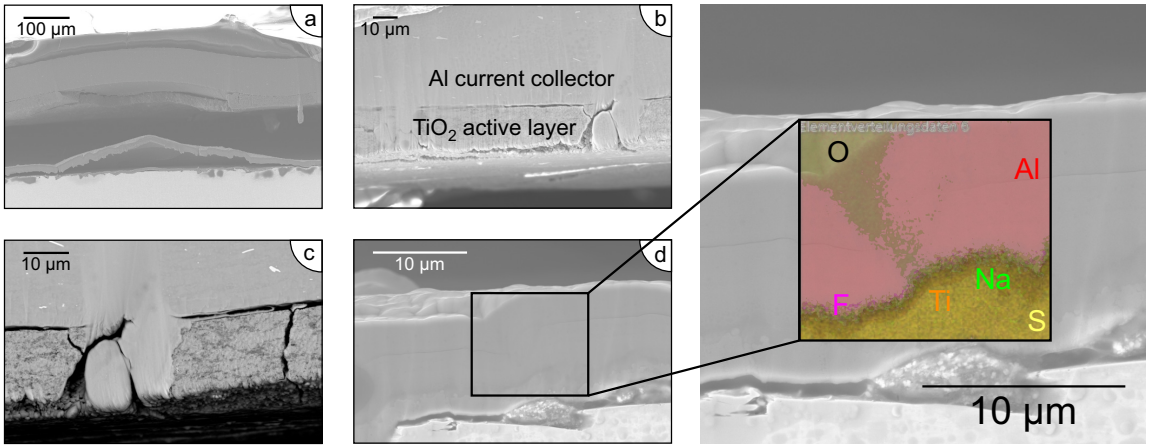

Figure 5: SEM pictures of cycled electrodes consisting of TiO_2 nanoparticle composite coated on aluminum substrate. Pictures (a), (b) and (d) were acquired from secondary electrons (SE). A back-scattered electron (BSE) picture enhances contrast between different material compositions in (c). The zoomed-in part on the right side represents EDX mapping of the indicated region.

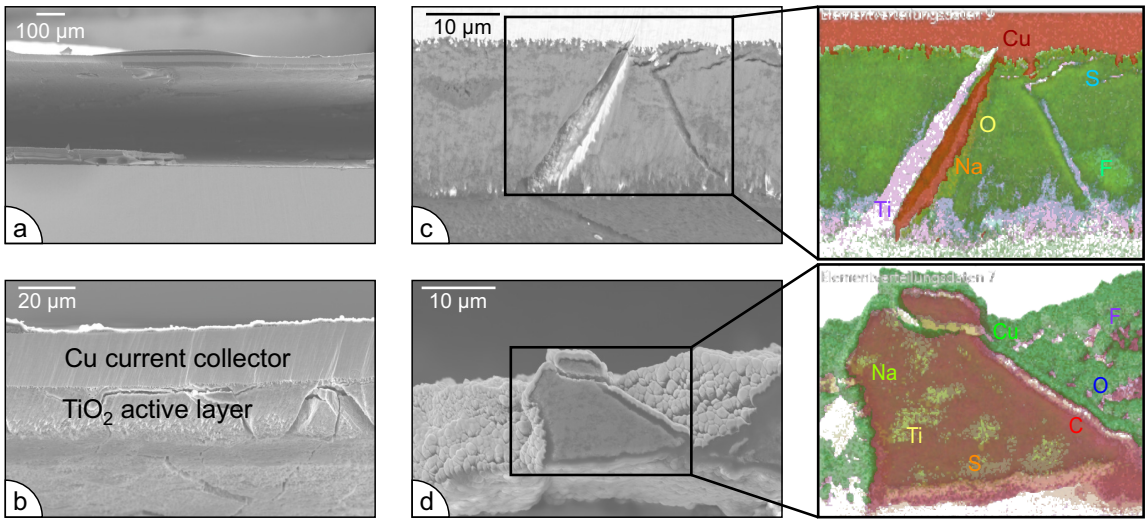

Figure 6: SEM pictures of the same active components as in Fig. 5, but cast on copper current collector. Detection methods are similar to those applied in Figure 5; SE mode for (a), (b), (d) and BSE mode for (c). EDC mapping of limited region, framed in (c) and (d), are depicted on the right-hand side.

sulfur signals inside the layer support this theory. We suggest that the aluminum containing interlayer prevents Na intercalation in active material closer to the current collector surface. As a result of this blocking effect, severe loss of capacity is observed at high cycling rates. Low rates, in contrary, enable slow transport through the layer and lead to recovery of initial capacity. Electrochemical data collected from copper based electrodes do not exhibit this behavior. Figure 6 shows several pictures acquired from a slope-cut electrode. Except for some parts that are peeled off the current collector during preparation, contact between current collector and active layer is maintained throughout the sample. As expected, the composite material exhibits fissure in both vertical and horizontal axes. Figure 6a depicts an overview of 1.3 mm of the sample, it reveals peeling of a large part of active layer with some Cu on it. Sufficient contact throughout larger areas of the electrode is depicted in section 6b. To draw attention to those parts of the active layer that are attached to the current collector, Fig. 6c presents a close-up view of the cracks in the material. EDX imaging detects copper-rich material growing inside the large crack of the active layer and simultaneously confirms absence of such phase in the smaller rifts on the right side. Furthermore, a closer look at the part of the composite separated from the substrate confirms existence of the same phase along its edges. Next to this structure, best seen in the overview picture 6a, a layer that covers the whole composite material surface can be identified. Figure 6d zooms in at smaller chunks and verifies the encapsulation of active material with said copper compound.

EDX assigns the layers to active material, an intermediate carbon layer and a copper and fluorine rich phase. Regarding electrochemical performance of the electrode, this construction compensates volume expansion and contraction and yields high reversibility and cycling stability. Finally, we suggest two origins for the Al and Cu coating of the electrolyte materials. (I) Analogous to previous stability studies for Cu and $LiPF_6$, we assume this copper compound to be a reaction product with the electrolyte [27, 28]. (II) Evaporation of the current collector material during the slope-cutting process and redeposition of the particular metal on the active layer.

IV. Conclusion

In this manuscript we investigated on the impact of current collector material to the performance of sodium-ion half cells. Various electrode materials were employed to highlight differences between copper and aluminum substrates. Electrochemical characterization of the materials revealed significant differences between substrate materials for TiO_2 nanoparticle composite electrodes. High cycling rates, viz., 1, 2 and 5 C, lead to a decrease of capacity on aluminum substrates, whereas copper electrodes exhibit no such behavior. After many cycles at heavy load, reduction of the cycling rate results in full recovery of the initial capacity. SEM points out that the aluminum substrate forms an interlayer underneath the surface of the composite material. This layer is considered a barrier that shields unexposed active material from taking part in the cell reaction. Such shielding effect does not occur at low cycling rates, which indicates that Na ions are able to migrate through this layer at a larger time frame. EDX specifies the layer as a composition of residues from the electrolyte and Al from the current collector. Formation of an enclosing interlayer can also be observed for Cu substrate. These layers either originate from reaction with other cells components, viz., electrolyte and active material, or is introduced during sample preparation for SEM investigations. Sodium transport to the active material is, apparently, not affected by formation of this layer.

References

[1] D Larcher, J.-M. Tarascon, *Nature Chemistry* **2014**, *7*, 19.

[2] J. T. Kummer, A. Arbor, N. Weber, Battery Having a Molten Alkali Metal Anode and a Molten Sulfur Cathode (US3,413,150A), **1968**.

[3] X. Xu, D. Zhou, X. Qin, K. Lin, F. Kang, B. Li, D. Shanmukaraj, T. Rojo, M. Armand, G. Wang, *Nature Communications* **2018**, *9*, 3870.

[4] E. Shembel, R. Apostolova, A. Strizhko, A. Belosokhov, A. Naumenko, V. Rozhkov, *Journal of Power Sources* **1995**, *54*, 421–424.

[5] S. Zhang, M. S. Ding, T. Jow, *Journal of Power Sources* **2001**, *102*, 16–20.

[6] S.-T. Myung, Y. Hitoshi, Y.-K. Sun, *Journal of Materials Chemistry* **2011**, *21*, 9891–9911.

[7] H Okamoto, *Journal of Phase Equilibria and Diffusion* **2012**, *33*, 500–501.

[8] F. Zhang, B. Ji, X. Tong, M. Sheng, X. Zhang, C.-S. Lee, Y. Tang, *Advanced Materials Interfaces* **2016**, *3*, 1600605.

[9] X. Tong, F. Zhang, B. Ji, M. Sheng, Y. Tang, *Advanced Materials* **2016**, *28*, 9979–9985.

[10] X. Zhang, Y. Tang, F. Zhang, C.-S. Lee, *Advanced Energy Materials* **2016**, *6*, 1502588.

[11] H. Yang, K. Kwon, T. M. Devine, J. W. Evans, *Journal of The Electrochemical Society* **2000**, *147*, 4399.

[12] A. Andersson, M. Herstedt, A. Bishop, K. Edström, *Electrochimica Acta* **2002**, *47*, 1885–1898.

[13] T. Nakajima, M. Mori, V. Gupta, Y. Ohzawa, H. Iwata, *Solid State Sciences* **2002**, *4*, 1385–1394.

[14] H.-B. Han, S.-S. Zhou, D.-J. Zhang, S.-W. Feng, L.-F. Li, K. Liu, W.-F. Feng, J. Nie, H. Li, X.-J. Huang, M. Armand, Z.-B. Zhou, *Journal of Power Sources* **2011**, *196*, 3623–3632.

[15] E. Kramer, S. Passerini, M. Winter, *ECS Electrochemistry Letters* **2012**, *1*, C9–C11.

[16] T Vogl, S Menne, A Balducci, *Physical Chemistry Chemical Physics* **2014**, *16*, 25014–25023.

[17] J. L. Murray, *Bulletin of Alloy Phase Diagrams* **1983**, *4*, 407–410.

[18] M. D. Slater, D. Kim, E. Lee, C. S. Johnson, *Advanced Functional Materials* **2012**, *23*, 947–958.

[19] X. Xia, W. M. Lamanna, J. R. Dahn, *Journal of the Electrochemical Society* **2013**, *160*, A607–A609.

[20] A. Ponrouch, E. Marchante, M. Courty, J. M. Tarascon, M. R. Palacín, *Energy and Environmental Science* **2012**, *5*, 8572–8583.

[21] C. Huang, D. Chen, Y. Huang, Y. Guo, *Electrochimica Acta* **2013**, *100*, 1–9.

[22] R. Alcantara, P. Lavela, G. F. Ortiz, J. L. Tirado, *Electrochemical and Solid-State Letters* **2005**, *8*, A222.

[23] L. J. Krause, W. Lamanna, J. Summerfield, M. Engle, G. Korba, R. Loch, R. Atanasoski, *Journal of Power Sources* **1997**, *68*, 320–325.

[24] T. D. Hatchard, M. N. Obrovac, *Journal of the Electrochemical Society* **2014**, *161*, A1748–A1752.

[25] L. Otaegui, E. Goikolea, F. Aguesse, M. Armand, T. Rojo, G. Singh, *Journal of Power Sources* **2015**, *297*, 168–173.

[26] L. Wu, D. Buchholz, D. Bresser, L. Gomes Chagas, S. Passerini, *Journal of Power Sources* **2014**, *251*, 379–385.

[27] L. Chen, Y. Li, S. P. Li, L. Z. Fan, C. W. Nan, J. B. Goodenough, *Nano Energy* **2018**, *46*, 176–184.

[28] J. Shu, M. Shui, F. Huang, D. Xu, Y. Ren, L. Hou, J. Cui, J. Xu, *Electrochimica Acta* **2011**, *56*, 3006–3014.

CHAPTER 5

CONCLUSIONS AND OUTLOOK

The aim of this thesis has been to provide deeper understanding of the functioning principles of battery components. This task was mainly accomplished by combination of 2 techniques that enable determination of macroscopic and microscopic ion transport properties. Information on long-ranged diffusion was provided by impedance spectroscopy, and ion hopping processes were precisely resolved by NMR spectroscopy. Due to its experimental versatility, the latter technique was also employed to sense phase formation processes. Even though the coupling of these two systems serves as a powerful tool to sense ion dynamics in a broad variety of samples, it cannot replace electrochemical characterization on a cell basis. Therefore, galvanostatic cycling and cyclic

voltammetry were used to characterize the effect of aluminum anode current collectors on the performance of sodium-ion battery electrodes. This thesis is, therefore, best described as inside out approach for characterization of battery components.

The Chapter (4.1) focused on precise determination of ion dynamics in single-crystalline LLZO systems. The application of LLZO in ASSBs is considered a hot topic and, therefore, proper ion dynamics studies are of utmost importance to reach this goal. From a fundamental point of view, a monocrystalline sample is an excellent model system to study ion dynamics that solely originate from bulk diffusion. The investigated cubic Al and Ga substituted LLZO single crystals were prepared by Czochralski method, that is a widely recognized method to produce monocrystalline silicon wafers for the semiconductor industry, at the Institute for Crystal Growth (IKZ) in Berlin. In both cases, as unmistakably illustrated by ^{7}Li spin-lattice relaxation data in the rotating frame of reference, the utter absence of grain boundary contributions led to better resolution of the ionic motion in the bulk. Measurements in the laboratory frame of reference revealed that local jump processes, viz., those between 24d and 96h lattice sites, in Al-LLZO are easily activated by energies ≤ 0.2 eV. The comparison with simulation data, provided by García Daza et al.,

revealed the adverse effect of dopants on 24*d* lattice sites that is, supposedly, enhanced by introduction of grain boundaries in polycrystalline materials. This idea is supported by the increase in activation energy to values ≥ 0.3 eV for medium-ranged to long-ranged diffusion processes.

In Ga-substituted LLZO single crystals a significant acceleration of diffusion processes was obtained. This statement is based on acquired data from conductivity spectroscopy that yielded conductivities of $1.1 \times 10^{-3}\,\mathrm{S\,cm^{-1}}$ at RT and is verified by a large shift of the obtained relaxation rate peaks towards low temperatures. This boost in ion dynamics can be assigned to the reduction in symmetry that originates from the acentric cubic structure ($I\bar{4}3d$) of Ga-substituted LLZO. However, to fully elucidate the ion hopping processes and assign the measured data to motion between particular lattice sites, accurate simulations are of utmost importance. These simulations are already in progress in will be added to the manuscript in the near future.

An alternative utilization of ^{7}Li NMR was reported in Chapter (4.2). Here, motional narrowing and spin-lattice relaxation were used to resolve the phase formation process of LTO that has been chemically sodiated. The chemical sodiation was performed by exposition of the pristine LTO to a solution of 1 M Na biphenyl-1,2-dimethoxyethane. Compositions were adjusted to different

sodiation ratios to resolve the phase formation process. In contrast to literature that reported on a multi-phase mechanism with separated Li and Na phases, we suggest the fluent passage from Na-poor solid-solution to Na-rich solid-solution that affects the motion of the observed Li nuclei. Close inspection of the NMR results pointed towards the formation of a dynamic solid-solution that enables temperature dependent Li diffusivity and varies in Na content.

The last subsection (4.3) in the experimental chapter approached the stability of aluminum current collectors in Na-ion batteries. Due to the inexistence of Na-Al alloys, aluminum was considered an inherently stable and, therefore, suitable substrate for anodes in Na-ion batteries. The performed galvanostatic cycling experiments proved that this rule does not apply for all anode materials. A comparison of several anode materials on aluminum and copper substrates revealed that the stability of aluminum current collectors largely depends on the applied electrode material. In particular, titania based electrodes exhibited severe capacity losses at elevated cycling rates. Excellent capacity retention, however, was achieved with all electrodes under investigation, even titania based ones at low cycling rates. To shed light on the electrode textures of the titania samples, cross-section SEM pictures were acquired in combination with EDX mapping. The results suggested the penetration of

aluminum decomposition products through the electrode material and formation of a layer composed of said compounds inside the active material. We suggest that this layer partially blocks ionic motion at high currents and, therefore, lower capacities were obtained at high cycling rates, whereas complete retention of the capacity is achieved at low rates.

Future research activities will mainly concentrate on the implementation of solid electrolytes in battery systems. Even though ionic conductivities are already close to those of liquid electrolytes, interfacial issues between solid electrolytes and electrode materials will represent the major challenge. Utilization of simplified model materials, like single crystals, will undoubtedly help find solutions to these upcoming problems. In less than a decade, it is expected that all-solid-state batteries will rule the market and revolutionize its fields of application.

BIBLIOGRAPHY

[1] International Energy Agency (IEA), *World Energy Outlook 2018: The Future is Electrifying*, **2018**.

[2] R. Mead, W. Greatbatch, F. Rudolph, **1976**, 3,944,433.

[3] B. B. Owens, *Solid State Ionics* **1981**, *3-4*, 273–275.

[4] M. Aoki, R. Okazaki, T. Sanukitani, K. Shinagawa, T. Fuji, *pat.*, JP19750152585, **1977**.

[5] D. Bennion, J. Dunning, W. Tiedemann, L. Hsueh, *pat.*, US3,844,837, **1974**.

[6] M. Binder, E. Petersen, C. Walker, W. Wade, S. Gilman, *pat.*, US4,514,478, **1985**.

[7] J. Shambaugh, R. Yetman, H. Zeltzer, *pat.*, US4,418,127, **1983**.

[8] M. S. Whittingham, *Chemistry of intercalation compounds: Metal guests in chalcogenide hosts, Vol. 12*, **1978**, pp. 41–99.

[9] J. Bichon, M. Danot, J. Rouxel, *Comptes rendus hebdomadaires des séances de l'Académie des sciences. Série C Sciences chimiques* **1973**, *276*, 4.

[10] L. Gaines, *pat.*, US4,091,191, **1978**.

[11] Y. Nishi, H. Azuma, A. Omaru, *pat.*, US4,959,281, **1990**.

[12] Y. Yamamoto, S. Fujita, H. Kato, *pat.*, WO1992JP00541, **1991**.

[13] Y. Nishi, *The Chemical Record* **2001**, *1*, 406–413.

[14] H. Wu, Y. Cui, *Nano Today* **2012**, *7*, 414–429.

[15] L. David, R. Bhandavat, U. Barrera, G. Singh, *Nature Communications* **2016**, *7*, 10998.

[16] Y. Miyaki, *pat.*, US7,132,197, **2003**.

[17] P. Balbuena, Y. Wang, *Lithium-ion Batteries: Solid-Electrolyte Interphase*, Imperial College Press, London, **2004**.

[18] W.-J. Zhang, *Journal of Power Sources* **2011**, *196*, 13–24.

[19] J. B. Goodenough, A. Padhi, K. S. Nanjundaswamy, C. Masquelier, *pat.*, CA2755356, **1997**.

[20] W. Li, J. R. Dahn, *pat.*, US5,733,681, **1998**.

[21] P. Rozier, J. M. Tarascon, *Journal of The Electrochemical Society* **2015**, *162*, A2490–A2499.

[22] N. Nitta, F. Wu, J. T. Lee, G. Yushin, *Materials Today* **2015**, *18*, 252–264.

[23] B. Zachau-Christiansen, K. West, T. Jacobsen, S. Atlung, *Solid State Ionics* **1990**, *40-41*, 580–584.

[24] T. Ohzuku, A. Ueda, N. Yamamoto, *Journal of The Electrochemical Society* **1995**, *142*, 1431.

[25] S. Scharner, W. Weppner, P. Schmid-Beurmann, *Journal of The Electrochemical Society* **1999**, *146*, 857.

[26] K Kanamura, T. Umegaki, H. Naito, Z. Takehara, T. Yao, *Journal of Applied Electrochemistry* **1998**, *31*, 73–78.

[27] T. F. Yi, L. J. Jiang, J. Shu, C. B. Yue, R. S. Zhu, H. B. Qiao, *Journal of Physics and Chemistry of Solids* **2010**, *71*, 1236–1242.

[28] S.-I. Tobishima, J.-I. Yamaki, T. Okada, *Electrochimica Acta* **1984**, *29*, 1471–1476.

[29] G.E.Blomgren, *Journal of Power Sources* **1999**, *81*, 112.

[30] K. Xu, *Chemical Reviews* **2004**, *104*, 4303–4418.

[31] W. Harris, PhD thesis, University of California, Berkeley, CA, **1958**.

[32] R. Selim, P. Bro, *Journal of The Electrochemical Society* **1974**, *121*, 1457.

[33] E. Peled, *Journal of The Electrochemical Society* **1979**, *126*, 2047.

[34] D. Aurbach, Y. Gofer, *Journal of The Electrochemical Society* **1989**, *136*, 3198.

[35] V. R. Koch, *Journal of The Electrochemical Society* **1982**, *129*, 1.

[36] S. A. Campbell, C. Bowes, R. S. McMillan, *Journal of Electroanalytical Chemistry* **1990**, *284*, 195–204.

[37] K. Xu, *Journal of The Electrochemical Society* **1999**, *146*, 4172.

[38] W. Elliott, Report No. 1, tech. rep., **1964**.

[39] G. Pistoia, M. D. Rossi, B. Scrosati, *Journal of The Electrochemical Society* **1970**, *117*, 500.

[40] O. D. Bonner, S.-J. Kim, A. L. Torres, *The Journal of Physical Chemistry* **1968**, *73*, 1968–1974.

[41] R. Fong, U. Von Sacken, J. R. Dahn, *Journal of The Electrochemical Society* **1990**, *137*, 2009–2013.

[42] S. Subbarao, D. H. Shen, F. Deligiannis, C. K. Huang, G. Halpert, *Journal of Power Sources* **1990**, *29*, 579–587.

[43] D. Guyomard, J.-M. Tarascon, *Journal of The Electrochemical Society* **1992**, *139*, 937–948.

[44] T. Ohzuku, Y. Iwakoshi, K. Sawai, *Journal of The Electrochemical Society* **1993**, *140*, 2490.

[45] M. Ue, S. Mori, *Journal of The Electrochemical Society* **1995**, *142*, 2577.

[46] D. Guyomard, J.-M. Tarascon, *Journal of The Electrochemical Society* **1993**, *140*, 248.

[47] J. M. Tarascon, D. Guyomard, *Solid State Ionics* **1994**, *69*, 293–305.

[48] W. K. Behl, E. J. Plichta, *Journal of Power Sources* **1998**, *72*, 132–135.

[49] E. J. Plichta, W. K. Behl, *Journal of Power Sources* **2000**, *88*, 192–196.

[50] S. E. Sloop, J. B. Kerr, K. Kinoshita, *Journal of Power Sources* **2003**, *119-121*, 330–337.

[51] B. Ravdel, K. M. Abraham, R. Gitzendanner, J. DiCarlo, B. Lucht, C. Campion, *Journal of Power Sources* **2003**, *119-121*, 805–810.

[52] K. Hayashi, Y. Nemoto, S. I. Tobishima, J. I. Yamaki, *Electrochimica Acta* **1999**, *44*, 2337–2344.

[53] S. S. Zhang, K. Xu, T. R. Jow, *Journal of The Electrochemical Society* **2002**, *149*, A586.

[54] S. S. Zhang, K. Xu, T. R. Jow, *Journal of Solid State Electrochemistry* **2003**, *7*, 147–151.

[55] W. Liu, N. Liu, J. Sun, P. C. Hsu, Y. Li, H. W. Lee, Y. Cui, *Nano Letters* **2015**, *15*, 2740–2745.

[56] K. Xu, S. Zhang, B. A. Poese, T. R. Jow, *Electrochemical and Solid-State Letters* **2002**, *5*, A259.

[57] K. Xu, S. Zhang, T. R. Jow, W. Xu, C. A. Angell, *Electrochemical and Solid-State Letters* **2002**, *5*, A26.

[58] F. Mestre-Aizpurua, S. Hamelet, C. Masquelier, M. R. Palacín, *Journal of Power Sources* **2010**, *195*, 6897–6901.

[59] S. Wang, W. Qiu, T. Li, B. Yu, H. Zhao, *International Journal of Electrochemical Science* **2006**, *1*, 250–257.

[60] X. Cui, H. Zhang, S. Li, Y. Zhao, L. Mao, W. Zhao, Y. Li, X. Ye, *Journal of Power Sources* **2013**, *240*, 476–485.

[61] D. P. Abraham, M. M. Furczon, S. H. Kang, D. W. Dees, A. N. Jansen, *Journal of Power Sources* **2008**, *180*, 612–620.

[62] O. V. Bushkova, T. V. Yaroslavtseva, Y. A. Dobrovolsky, *Russian Journal of Electrochemistry* **2017**, *53*, 677–699.

[63] D. T. Shieh, P. H. Hsieh, M. H. Yang, *Journal of Power Sources* **2007**, *174*, 663–667.

[64] S. Shui Zhang, *Electrochemistry Communications* **2006**, *8*, 1423–1428.

[65] S. S. Zhang, *Journal of Power Sources* **2007**, *163*, 713–718.

[66] S. Zugmann, D. Moosbauer, M. Amereller, C. Schreiner, F. Wudy, R. Schmitz, R. Schmitz, P. Isken, C. Dippel, R. Müller, M. Kunze, A. Lex-Balducci, M. Winter, H. J. Gores, *Journal of Power Sources* **2011**, *196*, 1417–1424.

[67] M. Nie, B. L. Lucht, *Journal of The Electrochemical Society* **2014**, *161*, A1001–A1006.

[68] S. Sylla, J. Y. Sanchez, M. Armand, *Electrochimica Acta* **1992**, *37*, 1699–1701.

[69] M. Morita, T. Shibata, N. Yoshimoto, M. Ishikawa, *Electrochimica Acta* **2002**, *47*, 2787–2793.

[70] L. Li, S. Zhou, H. Han, H. Li, J. Nie, M. Armand, Z. Zhou, X. Huang, *Journal of The Electrochemical Society* **2011**, *158*, A74.

[71] L. J. Krause, W. Lamanna, J. Summerfield, M. Engle, G. Korba, R. Loch, R. Atanasoski, *Journal of Power Sources* **1997**, *68*, 320–325.

[72] K. Naoi, *Journal of The Electrochemical Society* **1999**, *146*, 462.

[73] F. Michael, *Philosophical Transactions of the Royal Society of London* **1833**, *123*, 23–54.

[74] S. Kato, T. Yamauchi, *Journal of Japanese Ceramic Association* **1943**, *51*, 71–77.

[75] J. T. Kummer, A. Arbor, N. Weber, *pat.*, US3,413,150A, **1968**.

[76] J. Coetzer, *Journal of Power Sources* **1986**, *18*, 377–380.

[77] R. J. Bones, J. Coetzer, R. C. Galloway, D. A. Teagle, *Journal of The Electrochemical Society* **1987**, *134*, 2379–2382.

[78] J. J. Werth, *pat.*, US3,877,984, **1975**.

[79] W. Gorecki, R. Andreani, C. Berthier, M. Armand, M. Mali, J. Roos, D. Brinkmann, *Solid State Ionics* **1986**, *18-19*, 295–299.

[80] M. Minier, C. Berthier, W. Gorecki, *Journal de Physique* **1984**, *45*, 739–744.

[81] I. E. Kelly, J. R. Owen, B. C. Steele, *Journal of Power Sources* **1985**, *14*, 13–21.

[82] K. M. Abraham, M Alamgir, *Journal of The Electrochemical Society* **1990**, *137*, 1657–1658.

[83] G. B. Appetecchi, F Croce, B. Scrosati, *Electrochimica Acta* **1995**, *40*, 991–997.

[84] H. Choe, J. Giaccai, M. Alamgir, K. M. Abraham, *Electrochimica Acta* **1995**, *40*, 2289–2293.

[85] A. M. Stephan, *European Polymer Journal* **2006**, *42*, 21–42.

[86] A. Manuel Stephan, K. S. Nahm, *Polymer* **2006**, *47*, 5952–5964.

[87] G. B. Appetecchi, F Croce, M. Mastragostino, B. Scrosati, F. Soavi, A. Zanelli, *Journal of The Electrochemical Society* **1998**, *145*, 4133–4135.

[88] Q Li, Y Takeda, N Imanish, J Yang, H. Y. Sun, O Yamamoto, *Journal of Power Sources* **2001**, *98*, 795–797.

[89] C. W. Nan, L. Fan, Y. Lin, Q. Cai, *Physical Review Letters* **2003**, *91*, 1–4.

[90] J. Zhang, N. Zhao, M. Zhang, Y. Li, P. K. Chu, X. Guo, Z. Di, X. Wang, H. Li, *Nano Energy* **2016**, *28*, 447–454.

[91] K. K. Fu, Y. Gong, J. Dai, A. Gong, X. Han, Y. Yao, C. Wang, Y. Wang, Y. Chen, C. Yan, Y. Li, E. D. Wachsman, L. Hu, *Proceedings of the National Academy of Sciences* **2016**, *113*, 7094–7099.

[92] L. Chen, Y. Li, S. P. Li, L. Z. Fan, C. W. Nan, J. B. Goodenough, *Nano Energy* **2018**, *46*, 176–184.

[93] A. S. Pandian, X. C. Chen, J. Chen, B. S. Lokitz, R. E. Ruther, G. Yang, K. Lou, J. Nanda, F. M. Delnick, N. J. Dudney, *Journal of Power Sources* **2018**, *390*, 153–164.

[94] N. J. Dudney, J. B. Bates, R. A. Zuhr, C. F. Luck, J. D. Robertson, *Solid State Ionics* **1992**, *53-56*, 655–661.

[95] J. B. Bates, N. J. Dudney, G. R. Gruzalski, R. A. Zuhr, A. Choudhury, C. F. Luck, *Solid State Ionics* **1992**, *53-56*, 647–654.

[96] N. J. Dudney, B. J. Neudecker, *Current Opinion in Solid State and Materials Science* **1999**, *4*, 479–482.

[97] N. J. Dudney, *The Electrochemical Society Interface* **2008**, 44–48.

[98] A. Magistris, G. Chiodelli, M. Villa, *Journal of Power Sources* **1985**, *14*, 87–91.

[99] B. K. Money, K. Hariharan, *Solid State Ionics* **2008**, *179*, 1273–1277.

[100] B. Fleutot, B. Pecquenard, H. Martinez, A. Levasseur, *Solid State Ionics* **2013**, *249-250*, 49–55.

[101] R. L. Puurunen, *Chemical Vapor Deposition* **2004**, *10*, 159–170.

[102] T. Aaltonen, M. Alnes, O. Nilsen, L. Costelle, H. Fjellvåg, *Journal of Materials Chemistry* **2010**, *20*, 2877–2881.

[103] T. Aaltonen, O. Nilsen, A. Magrasó, H. Fjellvåg, *Chemistry of Materials* **2011**, *23*, 4669–4675.

[104] J. Hämäläinen, J. Holopainen, F. Munnik, T. Hatanpää, M. Heikkilä, M. Ritala, M. Leskelä, *Journal of The Electrochemical Society* **2012**, *159*, A259–A263.

[105] M. Nisula, Y. Shindo, H. Koga, M. Karppinen, *Chemistry of Materials* **2015**, *27*, 6987–6993.

[106] Y.-C. Perng, J. Cho, S. Y. Sun, D. Membreno, N. Cirigliano, B. Dunn, J. P. Chang, *J. Mater. Chem. A* **2014**, *2*, 9566–9573.

[107] J. Li, C. Ma, M. Chi, C. Liang, N. J. Dudney, *Advanced Energy Materials* **2015**, *5*, 1–6.

[108] L. O Hagman, P. Kierkegaard, *Acta Chemica Scandinavica* **1968**, *22*, 1822–1832.

[109] A. Clearfield, W. L. Duax, A. S. Medina, G. D. Smith, J. R. Thomas, *The Journal of Physical Chemistry* **1969**, *73*, 3424–3430.

[110] R. Masse, A. Durif, J. C. Guitel, I. Tordjman, *Bulletin de la Société Française de Minéralographie et de Cristallographie* **1972**, *95*, 47–55.

[111] J. B. Goodenough, H. Y.-p. Hong, J. A. Kafalas, *Materials Research Bulletin* **1976**, *11*, 203–220.

[112] W. M. Reiff, J. H. Zhang, C. C. Torardi, *Journal of Solid State Chemistry* **1986**, *62*, 231–240.

[113] C. C. Torardi, E. Prince, *Materials Research Bulletin* **1986**, *21*, 719–726.

[114] A. Manthiram, J. B. Goodenough, *Journal of Power Sources* **1989**, *26*, 403–408.

[115] J. Gopalakrishnan, K. K. Rangan, *Chemistry of Materials* **1992**, *4*, 745–747.

[116] A. K. Padhi, V. Manivannan, J. B. Goodenough, *Journal of The Electrochemical Society* **1998**, *145*, 1518–1520.

[117] A. Manthiram, J. B. Goodenough, *Journal of Solid State Chemistry* **1987**, *71*, 349–360.

[118] P. G. Bruce, G. Miln, *Journal of Solid State Chemistry* **1990**, *89*, 162–166.

[119] Z. Jian, Y. S. Hu, X. Ji, W. Chen, *Advanced Materials* **2017**, *29*, 1–16.

[120] X. Rui, Q. Yan, M. Skyllas-Kazacos, T. M. Lim, *Journal of Power Sources* **2014**, *258*, 19–38.

[121] Y. Q. Qiao, X. L. Wang, Y. J. Mai, J. Y. Xiang, D. Zhang, C. D. Gu, J. P. Tu, *Journal of Power Sources* **2011**, *196*, 8706–8709.

[122] X. H. Rui, C. Li, C. H. Chen, *Electrochimica Acta* **2009**, *54*, 3374–3380.

[123] Q. Chen, T. Zhang, X. Qiao, D. Li, J. Yang, *Journal of Power Sources* **2013**, *234*, 197–200.

[124] M. A. Subramanian, R. Subramanian, A. Clearfield, *Solid State Ionics* **1986**, *18-19*, 562–569.

[125] C. Delmas, F. Cherkaoui, A. Nadiri, P. Hagenmuller, *Materials research bulletin* **1987**, *22*, 631–639.

[126] K. Takada, M. Tansho, I. Yanase, T. Inada, A. Kajiyama, M. Kouguchi, S. Kondo, M. Watanabe, *Solid State Ionics* **2001**, *139*, 241–247.

[127] C. Delmas, A. Nadiri, J. L. Soubeyroux, *Solid State Ionics* **1988**, *28-30*, 419–423.

[128] H. Aono, E. Sugimoto, Y. Sadaoka, N. Imanaka, G. ya Adachi, *Solid State Ionics* **1990**, *40-41*, 38–42.

[129] K. Arbi, J. M. Rojo, J. Sanz, *Journal of the European Ceramic Society* **2007**, *27*, 4215–4218.

[130] M. Kotobuki, M. Koishi, Y. Kato, *Ionics* **2013**, *19*, 1945–1948.

[131] K. Arbi, W. Bucheli, R. Jiménez, J. Sanz, *Journal of the European Ceramic Society* **2015**, *35*, 1477–1484.

[132] Q. Ma, M. Guin, S. Naqash, C. L. Tsai, F. Tietz, O. Guillon, *Chemistry of Materials* **2016**, *28*, 4821–4828.

[133] Y. Deng, C. Eames, L. H. Nguyen, O. Pecher, K. J. Griffith, M. Courty, B. Fleutot, J. N. Chotard, C. P. Grey, M. S. Islam, C. Masquelier, *Chemistry of Materials* **2018**, *30*, 2618–2630.

[134] S. Lunghammer, Q. Ma, D. Rettenwander, I. Hanzu, F. Tietz, H. M. Wilkening, *Chemical Physics Letters* **2018**, *701*, 147–150.

[135] J. Brous, I. Fankuchen, E. Banks, *Acta Crystallographica* **1953**, *6*, 67–70.

[136] Y. Inaguma, C. Liquan, M. Itoh, T. Nakamura, T. Uchida, H. Ikuta, M. Wakihara, *Solid State Communications* **1993**, *86*, 689–693.

[137] H. Kawai, J. Kuwano, *Journal of The Electrochemical Society* **1994**, *141*, L78–L79.

[138] O. Bohnke, C. Bohnke, J. L. Fourquet, *Solid State Ionics* **1996**, *91*, 21–31.

[139] M. Krumpelt, I. D. Bloom, J. D. Pullockaran, K. M. Myles, *pat.*, US5,232,794, **1993**.

[140] N. Bonanos, K. S. Knight, B. Ellis, *Solid State Ionics* **1995**, *79*, 161–170.

[141] S. Tao, J. T. Irvine, *Materials for Sustainable Energy* **2003**, *2*, 320–323.

[142] Y. H. Huang, R. I. Dass, Z. L. King, J. B. Goodenough, *Science* **2006**, *312*, 254–257.

[143] Y. Zhao, L. L. Daemen, *Journal of the American Chemical Society* **2012**, *134*, 15042–15047.

[144] W. J. Kwon, H. Kim, K. N. Jung, W. Cho, S. H. Kim, J. W. Lee, M. S. Park, *Journal of Materials Chemistry A* **2017**, *5*, 6257–6262.

[145] Y. Li, H. Xu, P. H. Chien, N. Wu, S. Xin, L. Xue, K. Park, Y. Y. Hu, J. B. Goodenough, *Angewandte Chemie - International Edition* **2018**, *57*, 8587–8591.

[146] I. Hanghofer, G. J. Redhammer, S. Rohde, I. Hanzu, A. Senyshyn, H. M. R. Wilkening, D. Rettenwander, *Chemistry of Materials* **2018**, *30*, 8134–8144.

[147] H. T. Le, D. T. Ngo, P. N. Didwal, J. G. Fisher, C. N. Park, I. D. Kim, C. J. Park, *Journal of Materials Chemistry A* **2019**, *7*, 3150–3160.

[148] V. Thangadurai, H. Kaack, W. J. F. Weppner, *Journal of the American Ceramic Society* **2003**, *86*, 437–440.

[149] M. P. O'Callaghan, D. R. Lynham, E. J. Cussen, G. Z. Chen, *Chemistry of Materials* **2006**, *18*, 4681–4689.

[150] M. P. O'Callaghan, A. S. Powell, J. J. Titman, G. Z. Chen, E. J. Cussen, *Chemistry of Materials* **2008**, *20*, 2360–2369.

[151] E. J. Cussen, *Chemical Communications* **2006**, 412–413.

[152] E. J. Cussen, T. W. Yip, *Journal of Solid State Chemistry* **2007**, *180*, 1832–1839.

[153] V. Thangadurai, S. Narayanan, D. Pinzaru, *Chemical Society Reviews* **2014**, *43*, 4714–4727.

[154] M. P. O'Callaghan, E. J. Cussen, *Chemical Communications* **2007**, *12*, 2048–2050.

[155] V. Thangadurai, W. Weppner, *Journal of Solid State Chemistry* **2006**, *179*, 974–984.

[156] R. Murugan, V. Thangadurai, W. Weppner, *Angewandte Chemie - International Edition* **2007**, *46*, 7778–7781.

[157] J. Awaka, N. Kijima, H. Hayakawa, J. Akimoto, *Journal of Solid State Chemistry* **2009**, *182*, 2046–2052.

[158] V. Thangadurai, S. Adams, W. Weppner, *Chemistry of Materials* **2004**, *16*, 2998–3006.

[159] K. Meier, T. Laino, A. Curioni, *Journal of Physical Chemistry C* **2014**, *118*, 6668–6679.

[160] C. A. Geiger, E. Alekseev, B. Lazic, M. Fisch, T. Armbruster, R. Langner, M. Fechtelkord, N. Kim, T. Pettke, W. Weppner, *Inorganic Chemistry* **2011**, *50*, 1089–1097.

[161] M. Kotobuki, K. Kanamura, Y. Sato, T. Yoshida, *Journal of Power Sources* **2011**, *196*, 7750–7754.

[162] H. Buschmann, J. Dölle, S. Berendts, A. Kuhn, P. Bottke, M. Wilkening, P. Heitjans, A. Senyshyn, H. Ehrenberg, A. Lotnyk, V. Duppel, L. Kienle, J. Janek, *Physical Chemistry Chemical Physics* **2011**, *13*, 19378–19392.

[163] D. Rettenwander, P. Blaha, R. Laskowski, K. Schwarz, P. Bottke, M. Wilkening, C. A. Geiger, G. Amthauer, *Chemistry of Materials* **2014**, *26*, 2617–2623.

[164] D. Rettenwander, J. Langer, W. Schmidt, C. Arrer, K. J. Harris, V. Terskikh, G. R. Goward, M. Wilkening, G. Amthauer, *Chemistry of Materials* **2015**, *27*, 3135–3142.

[165] J. Wolfenstine, J. Ratchford, E. Rangasamy, J. Sakamoto, J. L. Allen, *Materials Chemistry and Physics* **2012**, *134*, 571–575.

[166] J. L. Allen, J. Wolfenstine, E. Rangasamy, J. Sakamoto, *Journal of Power Sources* **2012**, *206*, 315–319.

[167] T. Thompson, J. Wolfenstine, J. L. Allen, M. Johannes, A. Huq, I. N. David, J. Sakamoto, *Journal of Materials Chemistry A* **2014**, *2*, 13431–13436.

[168] P. Bottke, D. Rettenwander, W. Schmidt, G. Amthauer, M. Wilkening, *Chemistry of Materials* **2015**, *27*, 6571–6582.

[169] B. Stanje, D. Rettenwander, S. Breuer, M. Uitz, S. Berendts, M. Lerch, R. Uecker, G. Redhammer, I. Hanzu, M. Wilkening, *Annalen der Physik* **2017**, *529*, 1–9.

[170] A. Wachter-Welzl, J. Kirowitz, R. Wagner, S. Smetaczek, G. C. Brunauer, M. Bonta, D. Rettenwander, S. Taibl, A. Limbeck, G. Amthauer, J. Fleig, *Solid State Ionics* **2018**, *319*, 203–208.

[171] Y. Zhang, F. Chen, R. Tu, Q. Shen, L. Zhang, *Journal of Power Sources* **2014**, *268*, 960–964.

[172] F. A. García Daza, M. R. Bonilla, A. Llordés, J. Carrasco, E. Akhmatskaya, *ACS Applied Materials & Interfaces* **2019**, *11*, 753–765.

[173] C. Bernuy-Lopez, W. Manalastas, J. M. Lopez del Amo, A. Aguadero, F. Aguesse, J. A. Kilner, *Chemistry of Materials* **2014**, *26*, 3610–3617.

[174] M. A. Howard, O. Clemens, E. Kendrick, K. S. Knight, D. C. Apperley, P. A. Anderson, P. R. Slater, *Dalton Transactions* **2012**, *41*, 12048–12053.

[175] R. Wagner, G. J. Redhammer, D. Rettenwander, A. Senyshyn, W. Schmidt, M. Wilkening, G. Amthauer, *Chemistry of Materials* **2016**, *28*, 1861–1871.

[176] L. Cheng, E. J. Crumlin, W. Chen, R. Qiao, H. Hou, S. Franz Lux, V. Zorba, R. Russo, R. Kostecki, Z. Liu, K. Persson, W. Yang, J. Cabana, T. Richardson, G. Chen, M. Doeff, *Physical Chemistry Chemical Physics* **2014**, *16*, 18294–18300.

[177] Y. Zhu, X. He, Y. Mo, *Journal of Materials Chemistry A* **2016**, *4*, 3253–3266.

[178] A. Sharafi, H. M. Meyer, J. Nanda, J. Wolfenstine, J. Sakamoto, *Journal of Power Sources* **2016**, *302*, 135–139.

[179] W. Luo, Y. Gong, Y. Zhu, Y. Li, Y. Yao, Y. Zhang, K. K. Fu, G. Pastel, C. F. Lin, Y. Mo, E. D. Wachsman, L. Hu, *Advanced Materials* **2017**, *29*, 1–7.

[180] Z. Lu, J. Yu, J. Wu, M. B. Effat, S. C. Kwok, Y. Lyu, M. M. Yuen, F. Ciucci, *Energy Storage Materials* **2019**, *18*, 311–319.

[181] M. Wang, J. Sakamoto, *Journal of Power Sources* **2018**, *377*, 7–11.

[182] Y. Ren, Y. Shen, Y. Lin, C. W. Nan, *Electrochemistry Communications* **2015**, *57*, 27–30.

[183] L. Porz, T. Swamy, B. W. Sheldon, D. Rettenwander, T. Frömling, H. L. Thaman, S. Berendts, R. Uecker, W. C. Carter, Y. M. Chiang, *Advanced Energy Materials* **2017**, *7*, 1–12.

[184] B. Wu, S. Wang, J. Lochala, D. Desrochers, B. Liu, W. Zhang, J. Yang, J. Xiao, *Energy and Environmental Science* **2018**, *11*, 1803–1810.

[185] J. Kennedy, Y. Yang, *Journal of The Electrochemical Society* **1986**, 2437–2438.

[186] A. Pradel, M. Ribes, *Solid State Ionics* **1986**, *18-19*, 351–355.

[187] R. Kanno, T. Hata, Y. Kawamoto, M. Irie, *Solid State Ionics* **2000**, *130*, 97–104.

[188] R. Kanno, M. Murayama, *Journal of The Electrochemical Society* **2001**, *148*, A742.

[189] F. Mizuno, A. Hayashi, K. Tadanaga, M. Tatsumisago, *Advanced Materials* **2005**, *17*, 918–921.

[190] A. Hayashi, K. Minami, F. Mizuno, M. Tatsumisago, *Journal of Materials Science* **2008**, *43*, 1885–1889.

[191] Z. Liu, W. Fu, E. A. Payzant, X. Yu, Z. Wu, N. J. Dudney, J. Kiggans, K. Hong, A. J. Rondinone, C. Liang, *Journal of the American Chemical Society* **2013**, *135*, 975–978.

[192] E. Rangasamy, G. Sahu, J. K. Keum, A. J. Rondinone, N. J. Dudney, C. Liang, *Journal of Materials Chemistry A* **2014**, *2*, 4111–4116.

[193] E. Rangasamy, Z. Liu, M. Gobet, K. Pilar, G. Sahu, W. Zhou, H. Wu, S. Greenbaum, C. Liang, *Journal of the American Chemical Society* **2015**, *137*, 1384–1387.

[194] N. Kamaya, K. Homma, Y. Yamakawa, M. Hirayama, R. Kanno, M. Yonemura, T. Kamiyama, Y. Kato, S. Hama, K. Kawamoto, A. Mitsui, *Nature Materials* **2011**, *10*, 682.

[195] K. Takada, *Acta Materialia* **2013**, *61*, 759–770.

[196] Y. Mo, S. P. Ong, G. Ceder, *Chemistry of Materials* **2012**, *24*, 15–17.

[197] H Mehrer, *Diffusion in Solids: Fundamentals, Methods, Materials, Diffusion-Controlled Processes*, Springer Berlin Heidelberg, **2007**.

[198] J. Habasaki, C. Leon, K. Ngai, *Dynamics of Glassy, Crystalline and Liquid Ionic Conductors*, Springer International Publishing, **2016**.

[199] J. F. Nye, *Physical Properties of Crystals: Their Representation by Tensors and Matrices*, Clarendon Press, **1985**.

[200] J. Bardeen, C. Herring, *Atom movements: a seminar on atom movements held during the Thirty-second National Metal Congress and Exposition, Chicago, October 21 to 27, 1950*, American Society for Metals, Michigan, **1951**, p. 87.

[201] J. Bardeen, C. Herring, *Imperfections in nearly perfect crystals*, Wiley, **1952**, p. 262.

[202] R. J. D. Tilley, *Defects in Solids*, Wiley, **2008**.

[203] V. F. Lvovich, *Impedance Spectroscopy*, **2012**, pp. 1–21.

[204] A. K. Jonscher, *Nature* **1977**, *267*, 673–679.

[205] B. Roling, M. Meyer, A. Bunde, K. Funke, *Journal of Non-Crystalline Solids* **1998**, *226*, 138–144.

[206] D. L. Sidebottom, B. Roling, K. Funke, *Physical Review B - Condensed Matter and Materials Physics* **2000**, *63*, 1–7.

[207] D. L. Sidebottom, *Reviews of Modern Physics* **2009**, *81*, 999–1014.

[208] G. E. Murch, *Solid State Ionics* **1982**, *7*, 177–198.

[209] D. L. Sidebottom, *Physical Review Letters* **1999**, *83*, 983–986.

[210] J. T. S. Irvine, D. C. Sinclair, A. R. West, *Advanced Materials* **1990**, *2*, 132–138.

[211] H Friebolin, *Basic One- and Two-Dimensional NMR Spectroscopy*, Wiley, **2010**.

[212] N. Bloembergen, E. M. Purcell, R. V. Pound, *Physical Review* **1948**, *73*, 679–712.

[213] A. Kuhn, M. Kunze, P. Sreeraj, H. D. Wiemhöfer, V. Thangadurai, M. Wilkening, P. Heitjans, *Solid State Nuclear Magnetic Resonance* **2012**, *42*, 2–8.

APPENDIX

Publications and Manuscripts

I **Ion Dynamics in Al-Stabilized $Li_7La_3Zr_2O_{12}$ Single Crystals – Macroscopic Transport and the Elementary Steps of Ion Hopping**
P. Posch, S. Lunghammer, S. Berendts, S. Ganschow, G.J. Redhammer, A. Wilkening, M. Lerch, B. Gadermaier, D. Rettenwander and H.M.R. Wilkening – under review

II **^{7}Li NMR Resolves Diffusion Pathways in Single Crystalline Ga-Stabilized Li7La3Zr2O12 $Li_7La_3Zr_2O_{12}$**
P. Posch, L.J. Miara, S. Berendts, S. Ganschow, D. Rettenwander and H.M.R. Wilkening – Manuscript

III **Phase Formation in Chemically Sodiated Spinel-Type $Li_4Ti_5O_{12}$ Sensed by Solid-State NMR**
P. Posch, S. Lunghammer and H.M.R. Wilkening – Manuscript

IV **Is aluminum a proper anode current collector in Na-ion batteries? Insights from several case studies**
P. Posch, M. Nachtnebel, H. Schroettner, H.M.R. Wilkening and I. Hanzu – Manuscript

V **Self-Diffusion and Ion Exchange in mechanosynthesized, nanocrystalline solid solution of PbF_2 and CaF_2 – A ^{19}F 2D NMR EXSY Study to Visualize F site Preferences**
S. Lunghammer, A. Düvel, P. Posch, B. Kunert, R. Resel and H.M.R. Wilkening – Manuscript

VI **Ion transport in commercially available Na –β''– Alumina – state-of-the-art and future applications**
S. Lunghammer, P. Posch, D. Knez, D. Rettenwander, I. Hanzu and H.M.R. Wilkening –Manuscript

Oral Presentations

I **Ceramics for Safe Batteries**
P. Posch, C. Hiebl, M. Wilkening – Student Speech Contest AuCERS(Graz, Austria – 2017)

II **Inorganic Oxide Materials and their Suitability for Na- and Li-ion Batteries**
P. Posch, and M. Wilkening – DocDays(Graz, Austria – 2018)

Poster Presentations

I European Materials Research Society (EMRS) – Fall Meeting (Warsaw, Poland – 2016)
Hydrothermally synthesized sodium titanates as anode materials for sodium-ion batteries
P. Posch, I. Hanzu and M. Wilkening

II Solid State Ionics – SSI (Padua, Italy – 2017)
Hydrothermally synthesized sodium titanates as anode materials for sodium-ion batteries
P. Posch, I. Hanzu and M. Wilkening

III 2nd Dresden Battery Days (Dresden, Germany – 2017)
All-Solid-State Li and Na Batteries with Nanocrystalline Ceramics
P. Posch, M. Uitz, S. Lunghammer, S. Breuer, C. Täubert, V. Hennige and M. Wilkening

IV Americas International Meeting on Electrochemistry and Solid State Science – AiMES (Cancun, Mexico – 2018)
Ion Dynamics in Al-doped Cubic $Li_7La_3Zr_2O_{12}$ Garnet-Type Single Crystals
P. Posch, S. Lunghammer, S. Berendts, R. Uecker, D. Rettenwander and M. Wilkening

V $F^2C\pi^2$ Joint Conference – International Conference on ElectroCeramics (Lausanne, Switzerland – 2019)
Ion Dynamics in Al-stabilized $Li_7La_3Zr_2O_{12}$ Single Crystals – Two Elementary Steps of Ion Hopping Seen by NMR
P. Posch, S. Lunghammer, S. Berendts, S. Ganschow, D. Rettenwander and M. Wilkening

5.1 Supporting Information Single Crystalline Al-stabilized LLZO

Ion Dynamics in Al-Stabilized $Li_7La_3Zr_2O_{12}$ Single Crystals – Macroscopic Transport and the Elementary Steps of Ion Hopping

Patrick Posch[a]*, Sarah Lunghammer[a], Stefan Berendts[b], Steffen Ganschow[c], Günther J. Redhammer[d], Alexandra Wilkening[a], Martin Lerch[b], Daniel Rettenwander[a] and H. Martin R. Wilkening[a‡]

[a] Institute for Chemistry and Technology of Materials, Christian Doppler Laboratory for Lithium Batteries, Graz University of Technology (NAWI Graz), Graz, Austria;

[b] Department of Chemistry, Berlin University of Technology, Berlin, Germany;

[c] Leibniz-Institut für Kristallzüchtung (IKZ), Berlin, Germany;

[d] Department of Chemistry and Physics of Materials, University of Salzburg, Salzburg, Austria.

* p.posch@tugraz.at

‡ see also for correspondence: wilkening@tugraz.at

Analysis of the Al-stabilized LLZO single crystals by X-ray diffraction

Several crystals, suitable in size for X-ray diffraction experiments, were cleaved from different oddments, left over by the cutting process of slices from a large single crystal, and were cut to cuboid pieces of about 150 μm in diameter. Data collection was performed on a Bruker SMART APEX CCD-diffractometer. The single crystals were glued on top of a glass capillary (0.1 mm in diameter). Intensity data were collected with graphite-monochromatized Mo K_α X-ray radiation (50 kV, 20 mA). The crystal-to-detector distance was 30 mm and the detector positioned at −28° 2Θ and −40° 2Θ using an ω-scan mode strategy at four different θ positions (0°, 90°, 180° and 270°). 660 frames with $\Delta\omega$ = 0.3° were acquired for each run. Three-dimensional data were integrated and corrected for Lorentz-, polarization and background effects using the APEX3 software [1]. Structure refinement with weighted full-matrix least-squares refinements on F2 were carried out with SHELX-2012 [2] as implemented in the program suite WinGX 2014.1 [3].

All the tested crystals turned out to be single crystalline in nature and of good quality with sharp Bragg peaks; no evidence was found for any kinds of intergrowth or for diffuse streaks. The latter would be indicative for chemical inhomogeneity. The quality of the single crystals can also be judged from the calculated precession images shown in **Figure S1**.

For 3 out of 15 tested crystals, full data sets were measured, the details of data collection, refinement and structural details can be found in **Tables S1** to **S3**; indexing of all observed Bragg peaks proved the cubic, body centered, cell with space group symmetry $Ia\bar{3}d$. The crystal structure, obtained from the refinements is in very good agreement with the already reported ones [4–7]. An additional set of data, obtained from a crystal (FM_2), prepared and sintered following the procedures outlined in ref. [7], is included for comparison.

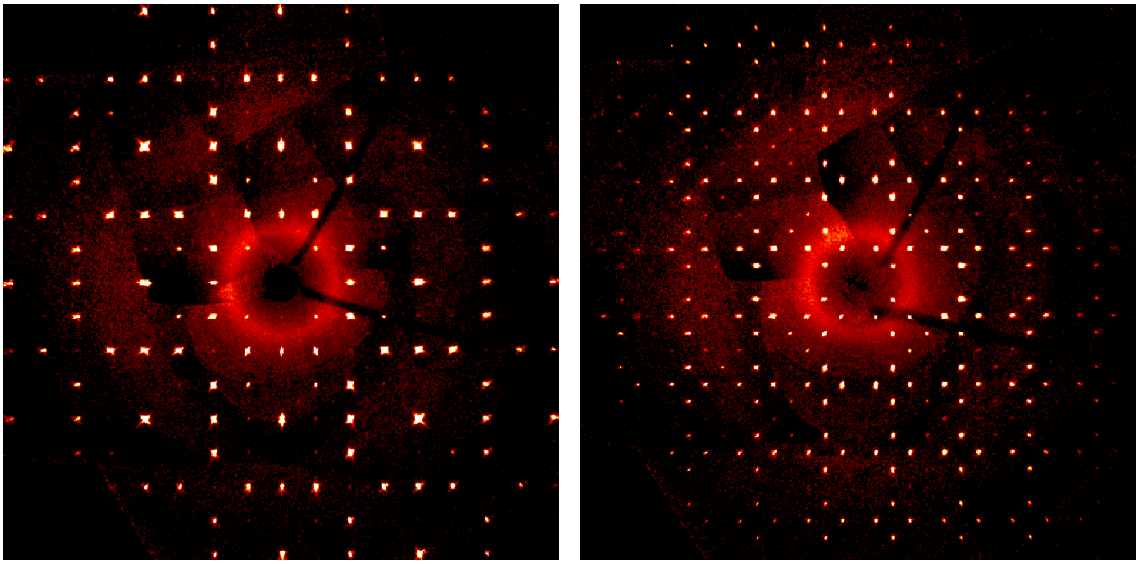

Figure S1: Calculated precession image of the (hk0) and the (hk1) plane for the cubic Al-LLZO crystal, cleaved from the large single crystal named EK_Al1.

As can be seen in **Table S1**, while the lattice parameters of the three single crystals EK_Al*i* (*i* = 1, 2, 3) are very similar, FM_2 reveals smaller lattice parameters. The latter single crystal was prepared by a solid-state route [7] and has directly been measured after finishing the synthesis. Following recent findings, this observations can be interpreted as a sign for a slight beginning Li^+/H^+ replacement caused by long-term storage of the oddments in humid air for approximately 4 months [5].

As is commonly observed for Al-doped LLZO, Li^+ distributes over two sites, the regular tetrahedral 24*d* sites and the interstitial 96*h* sites. Analyzing residual electron density maps, no indications for Li on other positions were found. The tetrahedral Li1 site is filled to about 60% and is remarkably similar in all the four data sets collected, while the split-site Li2 (96h) is occupied to approximately 38 % in the fresh FM_2 sample. The chips from the large single crystal show a somewhat smaller occupation of ca. 34%, which is seen as a further indication of some beginning alteration. From the structure refinements, the smallest distance between Li atoms (Li1-Li2 position) is approximately 1.67 Å, the second smallest is ca. 2.33 Å. The data are similar within the set of data from the Al-LLZO crystal, but show slight differences when compared with the results obtained for the freshly prepared crystal prepared by sintering. These very small differences do not encourage us to speculate on a small shift of Li2 position. All the other structural parameters are remarkably constant.

Table S1: Crystal data and structure refinement for the Al-doped LLZO single crystals

ID code	EK_Al1	EK_Al2	EK_Al3	FM_2
lattice parameter (Å)	12.9709(17)	12.9725(3)	12.9717(4)	12.9629(2)
crystal size (mm^3)	0.16 × 0.14 × 0.14	0.14 × 0.12 × 0.11	0.15 × 0.12 × 0.12	0.12 × 0.11 × 0.07
collected reflections	32924	33012	26524	33025
independ. reflections	459	458	453	456
R_{int} (%)	4.10	3.77	4.03	2.98
refined parameters	23	23	23	25
goodness of fit on F^2	1.338	1.324	1.394	1.534
R_1 (all data) (%)	2.36	2.49	3.335	1.86
wR_2 (all data) (%)	4.28	4.69	6.72	3.44
largest diff peak/ hole (e $Å^{-3}$)	0.581 / −1.263	0.759 / −1.017	1.030 / −1.531	0.648 / −0.394

EK_Al*i* with *i* = 1, 2, 3 denote smaller crystals taken from a large single crystal; FM_2 is a small single crystal obtained from a solid-state sintering experiment at 1230 °C. For all data sets: data collection at 295(1) K, Mo K_α radiation, λ = 0.71073 Å, refinement on F^2, cubic, space group $Ia\bar{3}d$, Z = 8.

Table S2: Atomic coordinates, occupation factors and equivalent isotropic displacement parameters for Al-doped LLZO of this study. U_{eq} is defined as one third of the trace of the orthogonalized U_{ij} tensor.

Site		EK_Al1	EK_Al2	EK_Al3	FM_2*
La (24*d*)	*x*	0.125	0.125	0.125	0.125
	y	0	0	0	0
	z	0.25	0.25	0.25	0.25
	Occ.	0.995(9)	0.993(9)	0.986(7)	0.984(8)
	$U_{eq.}$	0.01411(10)	0.01287(10)	0.00750(15)	0.00872(8)
Zr (16*a*)	*x*	0	0	0	0
	y	0	0	0	0
	z	0	0	0	0
	Occ.	1.0	1.0	1.0	1.0
	$U_{eq.}$	0.0172(4)	0.01139(17)	0.0057(2)	0.00675(13)
Li1 (24*d*)	*x*	0.375	0.375	0.375	0.375
	y	0	0	0	0
	z	0.25	0.25	0.25	0.25
	Li Occ.	0.561(23)	0.575(24)	0.580(28)	0.584(17)
	Al Occ.	0.05*	0.05*	0.05*	0.05*
	$U_{eq.}$	0.025(7)	0.022(6)	0.013(3)	0.018(6)
Li2 (96*h*)	*x*	0.1000(14)	0.1004(16)	0.0987(19)	0.0957(11)
	y	0.1887(16)	0.1877(18)	0.1899(21)	0.1887(12)
	z	0.4258(16)	0.4267(18)	0.4263(20)	0.4240(2)
	Occ.	0.349(16)	0.342(18)	0.343(21)	0.375(13)
	$U_{eq.}$	0.022(6)	0.021(6)	0.016(7)	0.019(7)
O (96*h*)	*x*	0.10045(16)	0.10048(17)	0.1003(3)	0.09995(14)
	y	0.19531(17)	0.19530(18)	0.1960(3)	0.19600(14)
	z	0.28128(17)	0.28148(18)	0.2814(3)	0.28183(14
	Occ.	1.0	1.0	1.0	1.0
	$U_{eq.}$	0.0172(4)	0.0157(4)	0.0102(5)	0.0119(3)

* = fixed during refinement to values obtained from chemical analysis.

Table S3: Selected bond length for Al-substituted LLZO single crystals

Distance	EK_Al1	EK_Al2	EK_Al3	FM_2*
La-O1	2.512(2)	2.514(2)	2.510(3)	2.5103(19)
La-O1	2.585(2)	2.586(2)	2.595(3)	2.5944(18)
Zr-O1	2.105(2)	2.105(2)	2.103(3)	2.1079(17)
Zr-Li2	2.93(2)	2.92(2)	2.93(2)	2.914(15)
Li1-O1	1.918(2)	1.917(2)	1.912(3)	1.9045(18)
Li1-Li2	1.67(2)	1.67(2)	1.64(3)	1.605(14)
Li2-Li2	2.32(2)	2.31(2)	2.34(3)	2.377(14)
Li2-O1	1.88(2)	1.89(2)	1.88(3)	1.847(15)
Li2-O1	2.14(2)	2.14(2)	2.12(3)	2.084(14)
Li2-O1	2.16(2)	2.14(2)	2.18(3)	2.170(15)
Li2-O1	2.25(2)	2.26(2)	2.23(3)	2.234(15)
Li2-Li2	0.69(3)	0.67(2)	0.73(5)	0.81(3)

References

[1] Bruker, (2015), APEX3 (Version 2015. 10-0), Bruker AXS Inc, Madison, Wisconsin, USA.

[2] G.M. Sheldrick, *Acta Crystallogr. Sect.* C **71** (2015) 3–8.

[3] L.J. Farrugia, *J. Appl. Crystallogr.* **45** (2012) 849–854.

[4] H. Buschmann, J. Dölle, S. Berendts, A. Kuhn, P. Bottke, M. Wilkening, P. Heitjans, A. Senyshyn, H. Ehrenberg, A. Lotnyk, V. Duppel, L. Kienle, J. Janek, *Phys. Chem. Chem. Phys.* **13** (2011) 19378–19392.

[5] C. Hiebl, D. Young, R. Wagner, H.M.R. Wilkening, G.J. Redhammer, D. Rettenwander, *J. Phys. Chem. C* **123** (2019) 1094–1098.

[6] D. Rettenwander, R. Wagner, J. Langer, M.E. Maier, M. Wilkening, G. Amthauer, *Eur. J. Mineral.* **28** (2016) 619–629.

[7] R. Wagner, G.J. Redhammer, D. Rettenwander, A. Senyshyn, W. Schmidt, M. Wilkening, G. Amthauer, *Chem. Mater.* **28** (2016) 1861–1871.